

Contents

1	Introduction	3
1.1	A brief history of superfluidity	3
1.2	Some key concepts	6
1.2.1	Bose-Einstein condensation and long-range order . .	7
1.2.2	Bogolyubov's approximation and the order parameter	8
1.2.3	Landau's criterion for superfluidity	10
1.2.4	Rotation and vorticity in superfluids	13
1.3	Helium droplets	15
1.4	Structure of the thesis	18
1.4.1	Part I: Excited state dynamics	18
1.4.2	Part II: Collisions and capture by quantised vortices .	18
2	The DFT method for heavy impurities	21
2.1	The Orsay-Trento Density Functional	23
2.1.1	The Solid-OT Density Functional	26
2.2	Static calculations	27
2.2.1	Producing vortical states	27
2.3	Dynamic calculations	28
2.3.1	The DIM model	29
2.3.2	Including spin-orbit coupling	32
I	Photo-excitation dynamics of alkalis	35
3	Introduction	37
3.1	Imaging Excited-State Dynamics	37
3.2	Desorption dynamics of RbHe-exciplexes	38
4	Results	41
4.1	Imaging Excited-State Dynamics	41
4.2	Desorption dynamics of RbHe exciplexes	48

4.3 Supervised work: Dynamics of superfluid helium nanodroplets doped with potassium	61
II Head-on collisions and capture by quantised vortices 63	
5 Introduction	65
5.1 Head-on collisions	65
5.2 Capture by quantised vortices	66
6 Results	69
6.1 Head-on collisions	69
6.2 Capture by quantised vortices	77
7 Conclusions & Outlook	93
Bibliography	93

Chapter 1

Introduction

SUPERFLUIDS are liquids and gases with remarkable properties. In particular, superfluid helium can flow through a capillary without friction due to its extremely small viscosity (at least 1500 times smaller than normal liquid helium^[1]), or creep up the wall of a container, seemingly defying the force of gravity^[2] (“Rollin creeping”). Its thermal conductivity is about 3×10^6 times higher than that of liquid helium I or about 200 times higher than that of copper at room temperature^[3]. It therefore earned the title of “best heat conducting substance we know” by Willem and his daughter Anna Keesom and dubbed “*supra-heat-conducting*”^[3]. Later it was understood why^[4–7] and it turns out that heat doesn’t diffuse through the medium as in normal liquids, but rather it travels through the medium in waves (second sound). This makes it an ideal coolant e.g. to stabilise the superconducting magnets in CERN’s Large Hadron Collider^[8]. Helium is also the only known substance that stays liquid at zero temperature and low pressures and both its angular momentum and vorticity are quantised, making it the first observed macroscopic quantum substance. Helium-4 becomes superfluid below the λ -point, named so by William H. Keesom in 1936 who measured a singularity in the specific heat at $T_\lambda = 2.2\text{ K}$ ^[3].

1.1 A brief history of superfluidity

HELIUM was the last gas to be liquefied and was done so by Heike Kamerlingh Onnes in 1908^[11,12]. In 1932 John McLennan saw that liquid helium stopped boiling below $\approx 2.2\text{ K}$ ^[13] and later that year Willem Keesom and his daughter Anna observed, while measuring the temperature dependence of the specific heat, a singularity around the same temperature^[9]. They called it the “ λ -temperature”, T_λ , because of the

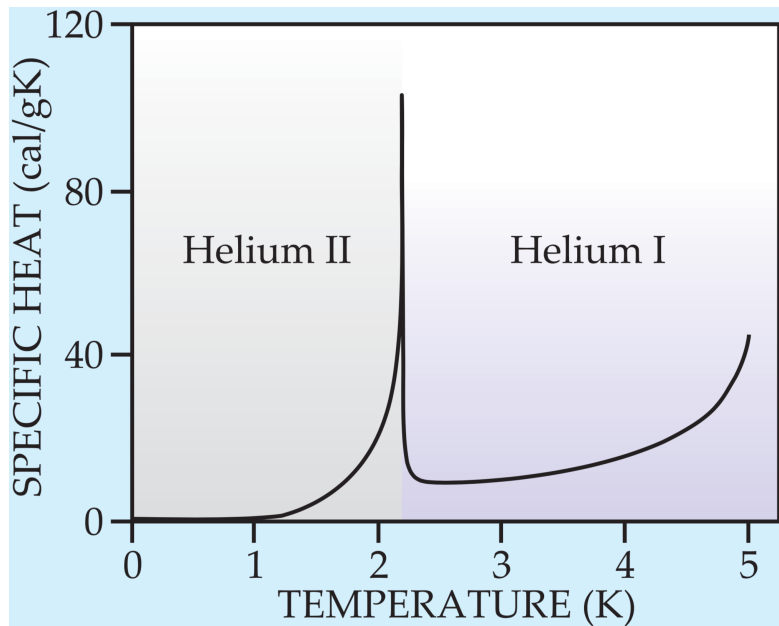


Figure 1.1: The specific heat of ${}^4\text{He}$ as a function of the temperature. There is a clearly visible singularity around 2.2 K and the graph itself has the distinct λ -like shape that inspired^[9] Willem and Anna Keesom to call the temperature at which the singularity occurs the “ λ -point”. (Illustration courtesy of R.J. Donnelly^[10])

shape of the temperature dependence of the specific heat resembling the Greek letter λ (see Figure 1.1). A few years later in 1935 Burton measured a sharp decrease in the viscosity of liquid helium below T_λ ^[14]. Around the same time Fritz London was already thinking about macroscopic wave functions and why helium does not freeze at $T = 0\text{ K}$ under atmospheric pressure^[15]. London and Simon concluded that it was caused by the zero point motion of the helium atoms and their associated kinetic energy that is comparable to their Van der Waals energy, effectively preventing liquid helium to solidify^[16,17]. The year after, in 1936, Willem and Anna Keesom measured an abnormally high heat conductance below T_λ ^[3]. This was confirmed roughly one year later by J.F. Allen *et al.*^[18] and it was understood that the high thermal conductance was the reason for the helium to stop boiling whenever the temperature drops below T_λ . It was in 1937, when Kapitza tried to determine the viscosity of the laminar flow, that he measured a viscosity that was about 10^4 times smaller than that of hydrogen gas^[1]. It was then that Kaptiza who, by analogy with superconductors, first

coined the word “superfluid”^[1] to describe the special state that helium enters below the λ -point where it can flow, seemingly without friction. Allen and Misener realised that superfluid helium is not just a liquid with a very low viscosity, but that its hydrodynamics was completely different from that of ordinary liquids^[19] and therefore required a completely new interpretation.

The start of this new interpretation was made by London^[20] in 1938 when he made a connection between the behaviour of superfluid helium and that of an ideal “Bose–Einstein” (BE) gas. Both his calculated value for $T_c = 3.09\text{ K}$ and the behaviour of the temperature dependence of the heat capacity for the ideal BE-gas were very similar to the measured ones for liquid helium below T_λ . He wrote to Nature that “it was difficult not to imagine a connection with “Bose–Einstein condensation” (BEC). Tisza expanded upon London’s ideas^[21] and considered a Helium II system of total N atoms to consist of two parts; a macroscopic “condensed” part n_0 , the superfluid component, in the ground state, and the remaining part $n = N - n_0$, the normal component, where the helium atoms are distributed over the excited states. Assuming this was correct the fraction n_0/N should decrease with increasing temperature according to the equation

$$\frac{n_0}{N} = 1 - \left(\frac{T}{T_0} \right)^s \quad \text{for } T < T_0 \quad (1.1)$$

where $s = 3/2$ for an ideal gas and should be taken larger, e.g. $s = 5$, for a real liquid with stronger interactions between the atoms.

This was the birth of the “two-fluid” model. With this model he derived two hydrodynamic equations for liquid helium below T_λ and discovered that within it, heat propagates in waves instead of diffusing through the medium, and calculated the velocity of these waves. He also explained why the viscosity is disappearing at low temperatures contrary to classical liquids where the viscosity increases^[4–7]. In 1941 Lev Landau reformulated Tisza’s theory on a more rigorous footing^[22,23]. He assumed, contrary to Tisza, that the normal component of the liquid was made-up of collective excitations instead of excited single atoms. He postulated that the liquid could exhibit two states of motion which he called “potential motion” that is irrotational ($\nabla \times \mathbf{v} = 0$), and “vortex motion” that is rotational ($\nabla \times \mathbf{v} \neq 0$). The corresponding energies of these two motions are discontinuously separated by an energy gap Δ . In case of potential internal motion the excitations are quanta of longitudinal (sound) waves, i.e., phonons.

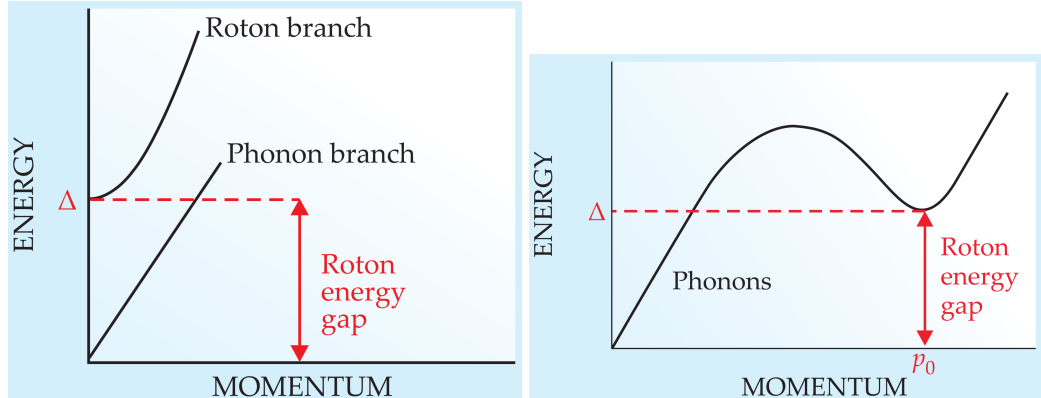


Figure 1.2: Left: Lev Landau’s 1941 energy dispersion curve^[22] for the excitations in liquid helium below T_λ . It exhibits a phonon- and a roton branch. The slope of the linear phonon branch corresponds to the velocity of sound. Right: Lev Landau’s 1947 modified dispersion curve. The roton-branch is no longer a separate excitation branch but rather an extension of the phonon-branch. (Illustration courtesy of R.J. Donnelly^[10])

The excitations of the vortex-spectrum could be called “rotons”(see Figure 1.2).

A theoretical demonstration, explicitly showing that phonons and rotons are collective excitations of the liquid, came in the form of a 1947 paper by Nikolay Bogolyubov^[24]. The intimate relationship between superfluidity and BEC was not universally accepted until 1995 when Cornell and Wieman in Colorado and Ketterle at MIT discovered BEC in rubidium quantum gases^[25,26].

1.2 Some key concepts

In this section I will briefly introduce some key ideas that are used throughout the thesis and that are needed to fully appreciate the discussed material. Also references to more complete and more in-depth treatments will be provided for the interested reader.

1.2.1 Bose-Einstein condensation and long-range order

The essential concept of Bose-Einstein condensation is the fact that at low temperatures, multiple bosons, unlike fermions, will occupy the same quantum state. In theory there is no upper bound of how many bosons can occupy such a single state. It is then said that, with ever decreasing temperature, a macroscopic part of the total number of bosons will “condense” into the quantum state with the lowest energy.

Another important concept in BEC is the idea of long-range order. Let us start by introducing the one-body density matrix of a system of N bosons in a pure state $\Psi_k(\mathbf{r}_1, \mathbf{r}_2, \dots, \mathbf{r}_N)$

$$n_k^{(1)}(\mathbf{r}, \mathbf{r}') := N \int \Psi_k^*(\mathbf{r}, \mathbf{r}_2, \dots, \mathbf{r}_N) \Psi_k(\mathbf{r}', \mathbf{r}_2, \dots, \mathbf{r}_N) d\mathbf{r}_2 d\mathbf{r}_3 \dots d\mathbf{r}_N \quad (1.2)$$

where the integral is taken over the $N - 1$ coordinates $\mathbf{r}_2, \mathbf{r}_3, \dots, \mathbf{r}_N$. For a statistical mixture of quantum states one needs to take the weighted average over all the different Ψ_k -states. In thermodynamic equilibrium the states are Boltzmann weighted by their eigenvalues $\{E_k\}$

$$n^{(1)}(\mathbf{r}, \mathbf{r}') = \frac{1}{Q} \sum_k n_k^{(1)}(\mathbf{r}, \mathbf{r}') e^{-E_k/k_B T} \quad (1.3)$$

where Q is the partition function. For more general cases the one-body density matrix is defined

$$n^{(1)}(\mathbf{r}, \mathbf{r}') := \langle \hat{\Psi}^\dagger(\mathbf{r}) \hat{\Psi}(\mathbf{r}') \rangle \quad (1.4)$$

where $\hat{\Psi}^\dagger(\mathbf{r})/\hat{\Psi}(\mathbf{r})$ are field-operators creating/annihilating a boson at \mathbf{r} and the averaging $\langle \dots \rangle$ is taken over all states in the mixture. Once it is accepted that a macroscopic part of the total number of bosons can occupy a single quantum state it can be demonstrated that, while considering a uniform isotropic system of N bosons, the one-body density matrix (Eq. 1.2) tends to a constant value when the distance between \mathbf{r} and \mathbf{r}' goes to infinity. In the thermodynamic limit where $N, V \rightarrow \infty$ such that $n = N/V$ is kept fixed, the one-body density only depends on the modulus of the relative variable $\mathbf{s} := \mathbf{r} - \mathbf{r}'$ so that we can write it as the Fourier transform of the momentum distribution as

$$n^{(1)}(s) = \frac{1}{V} \int n^{(1)}(\mathbf{p}) \exp(i\mathbf{p} \cdot \mathbf{s}/\hbar) d\mathbf{p} \quad (1.5)$$

For a Bose-Einstein condensed system, the momentum distribution at small momenta is not smooth but has a sharp peak around $p = 0$ for the bosons that are in the ground state, while the remaining bosons are smoothly distributed over the excited states.

$$n(\mathbf{p}) = N_0 \delta(\mathbf{p}) + \tilde{n}(\mathbf{p}) \quad (1.6)$$

where \tilde{n} is a smoothly varying function of \mathbf{p} . When this expression is plugged into Eq. (1.5) and taking the limit where s goes to infinity

$$\lim_{s \rightarrow \infty} n^{(1)}(s) = \frac{N_0}{V}, \quad (1.7)$$

where $N_0/V := n_0 \leq 1$ is called the condensate fraction. It is called long-range order since it involves the off-diagonal elements of the one-body density matrix; the elements that are usually associated with the coherences.

A set of eigenvalues $\{n_i\}$ of the one-body density matrix can be defined through the following eigenvalue equation

$$\int n^{(1)}(\mathbf{r}, \mathbf{r}') \varphi_i(\mathbf{r}') d\mathbf{r}' = n_i \varphi_i(\mathbf{r}) \quad (1.8)$$

and its solutions $\{\varphi_i\}$ form a natural orthonormal basis set of single boson wave functions $\int \varphi_i^* \varphi_j d\mathbf{r} = \delta_{ij}$, with normalisation condition $\sum_i n_i = N$. This permits writing the one-body density matrix in a useful diagonalised form and recalling that Bose-Einstein condensation occurs when a single particle state φ_i is occupied in a macroscopic way, say when $n_{i=0} = N_0$, a number of order N , we separate the condensate part from the rest

$$n^{(1)}(\mathbf{r}, \mathbf{r}') = N_0 \varphi_0^*(\mathbf{r}) \varphi_0(\mathbf{r}') + \sum_{i \neq 0} n_i \varphi_i^*(\mathbf{r}) \varphi_i(\mathbf{r}') \quad (1.9)$$

1.2.2 Bogolyubov's approximation and the order parameter

It is customary, given the importance of the condensate fraction N_0 in a BEC, to write the field operator of a N -body boson system as the sum of the condensate part and the rest, just as the one-body density matrix

$$\hat{\Psi}(\mathbf{r}) = \varphi_0(\mathbf{r}) \hat{a}_0 + \sum_{i \neq 0} \varphi_i(\mathbf{r}) \hat{a}_i \quad (1.10)$$

where the \hat{a}_i and \hat{a}_i^\dagger are annihilation and creation operator of a particle in state φ_i and obey the usual bosonic commutation relations

$$[\hat{a}_i, \hat{a}_j^\dagger] = \delta_{ij}, \quad [\hat{a}_i, \hat{a}_j] = 0 = [\hat{a}_i^\dagger, \hat{a}_j^\dagger] \quad (1.11)$$

Using Eq. (1.10) in Eq. (1.2) and comparing it to Eq. (1.9) one finds the expectation value of $\langle \hat{a}_j^\dagger \hat{a}_i \rangle = \delta_{ij} n_i$. Now, the Bogolyubov approximation essentially replaces the operators \hat{a}_0 and \hat{a}_0^\dagger with the *c*-number¹ $\sqrt{N_0}$. This is equivalent to ignoring the non-commutative nature of the operators due to the macroscopic occupation of the state φ_0 , when $N_0 = \langle \hat{a}_0^\dagger \hat{a}_0 \rangle \gg 1$. We then rewrite the field operator as the sum of a classical field for the condensed component and quantum field for the non-condensed component

$$\hat{\Psi}(\mathbf{r}) = \Psi_0(\mathbf{r}) + \delta\hat{\Psi}(\mathbf{r}), \quad (1.12)$$

where $\delta\hat{\Psi}(\mathbf{r}) = \sum_{i \neq 0} \varphi_i(\mathbf{r}) \hat{a}_i$ and $\Psi_0(\mathbf{r}) = \sqrt{N_0} \varphi_0(\mathbf{r})$. At $T = 0$ the whole system is condensed and one can ignore $\delta\hat{\Psi}$ altogether; the field operator becomes a normal function of space Ψ_0 .

The classical field Ψ_0 is called the *effective-* or *macroscopic* wave function of the condensate and it behaves like an order parameter in the sense that it varies continuously between a maximum value \sqrt{N} , that is proportional to the total number particles in the system, at $T = 0$, and vanishes at the superfluid-normal fluid phase transition temperature T_λ . It is a complex quantity characterised by a real-valued modulus and phase S :

$$\Psi_0(\mathbf{r}) = |\sqrt{N_0} \varphi_0(\mathbf{r})| e^{iS(\mathbf{r})} \quad (1.13)$$

The modulus determines the number-density of the condensate, while the phase S plays an important role in the coherence and properties of the superfluid. As we will see in Section 1.2.4, S plays the role of a velocity potential.

Using an order parameter as defined here is equivalent to using the many-body wave function

$$\Phi(\mathbf{r}_1, \mathbf{r}_2, \dots, \mathbf{r}_N) = \prod_{i=1}^N \varphi_0(\mathbf{r}_i), \quad (1.14)$$

¹The term *c*-number is old nomenclature for a classical number, which can be real or complex, to distinguish them from quantum numbers, or *q*-numbers, that are represented by operators.

with a density operator $\hat{\rho}(\mathbf{r}) := \sum_{i=1}^N \delta(\mathbf{r} - \mathbf{r}_i)$ (see Section 2). One way to see why this wave function plays the role of an order parameter is to look at its time dependence. For normal wave functions the time dependence is determined by the eigenvalues E_i of the Hamiltonian of the system

$$\Psi(\mathbf{r}, t) = \psi(\mathbf{r}) e^{-iE_i t/\hbar} \quad (1.15)$$

But in this case, the time dependence is determined by the chemical potential $\mu = E(N) - E(N-1) \approx \partial E / \partial N$

$$\Psi_0(\mathbf{r}, t) = \Psi_0(\mathbf{r}) e^{-i\mu t/\hbar} \quad (1.16)$$

Another aspect of Ψ_0 being an order parameter and not a true many-body wave function is that two solutions Ψ_a and Ψ_b of the non-linear droplet Hamiltonian corresponding to two different values of the chemical potential μ_a and μ_b are not necessarily orthogonal, i.e. $0 \leq N^{-1} \int \Psi_a^* \Psi_b d\mathbf{r} < 1$. However, in dilute gases it is possible to construct a many-body wave function from the order parameter that regains its orthonormality in the thermodynamic limit

$$\Phi_0(\mathbf{r}_1, \mathbf{r}_2, \dots, \mathbf{r}_N) = \left(\frac{1}{\sqrt{N}} \Psi_0(\mathbf{r}_1) \right) \left(\frac{1}{\sqrt{N}} \Psi_0(\mathbf{r}_2) \right) \cdots \left(\frac{1}{\sqrt{N}} \Psi_0(\mathbf{r}_N) \right) \quad (1.17)$$

1.2.3 Landau's criterion for superfluidity

For a gas or liquid to be able to become superfluid Landau postulated that the energy dispersion relation needs to fulfil certain requirements. Specifically for a fluid to flow without dissipation, i.e. a super-flow, the velocity field needs to fulfil the following inequality:

$$v < v_c = \min_{\mathbf{p}} \frac{\epsilon(\mathbf{p})}{p} \quad (1.18)$$

For an ideal Bose gas $\epsilon(\mathbf{p}) = \frac{p^2}{2m}$. In this case

$$v_c = \min_{\mathbf{p}} \frac{\epsilon(\mathbf{p})}{p} \quad (1.19)$$

$$= \min_{\mathbf{p}} \frac{p}{2m} \quad (1.20)$$

$$= 0 \quad (1.21)$$

Apparently ideal Bose-gases cannot become superfluid.

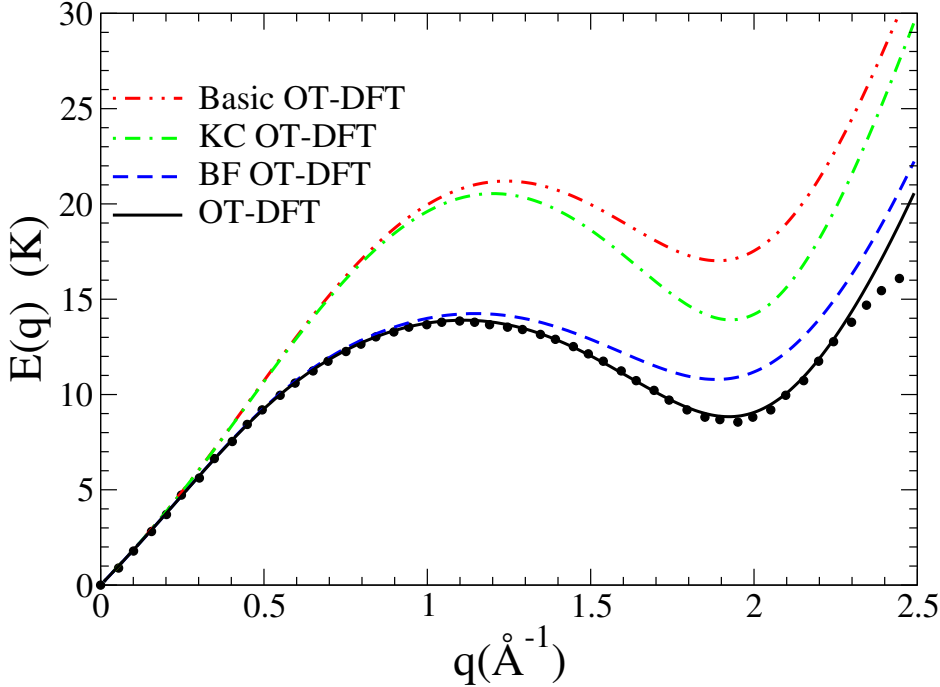


Figure 1.3: Dispersion relation for elementary excitations in liquid ^4He calculated as in^[27]. ‘Basic’ indicates the OT-DFT without the non-local kinetic energy correlation (KC) nor the back-flow (BF) terms; KC OT-DFT adds to the basic OT-DFT the KC term; BF OT-DFT adds to the basic OT-DFT the BF term. The dots are the experimental data from^[28]. The Landau velocity $v_L = E(q)/(\hbar q)|_{min}$ obtained for each functional is 60.3 m/s (OT-DFT); 75.1 m/s (BF OT-DFT); 94.4 m/s (KC OT-DFT); 118 m/s (basic OT-DFT); and 57.5 (experiment).

But if we allow for some weak interactions between the bosons the energy dispersion relation is given by

$$\epsilon(\mathbf{p}) = \sqrt{\frac{gn}{m}p^2 + \left(\frac{p^2}{2m}\right)^2}, \quad (1.22)$$

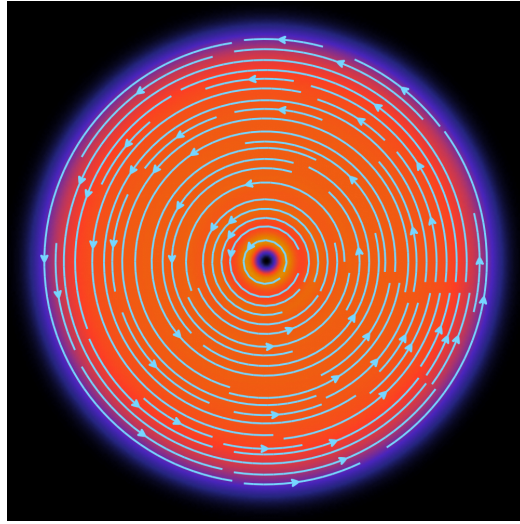


Figure 1.4: Cross section of a ${}^4\text{He}$ droplet through a symmetry plane. The droplet is made of 1000 atoms. Superimposed in cyan are the streamlines of the velocity field \mathbf{v}_s for $s = 1$. They are concentric circles, centred around the vortex core along the z -axis. The colour scale encodes for the density $\rho(r)$. The radius of the droplet is about 22 Å.

Bogolyubov's dispersion law for elementary excitations (1947). And thus

$$v_c = \min_p \sqrt{\frac{gn}{m} + \frac{p^2}{4m^2}} \quad (1.23)$$

$$= \sqrt{\frac{gn}{m}} \quad (1.24)$$

$$= c, \quad (1.25)$$

the speed of sound. Here $g = \frac{4\pi\hbar^2 a}{m}$, and a the s -wave scattering length. The weakly interacting Bose gases can become superfluid.

Liquid helium below the λ -point has a similar energy dispersion relation (see Figure 1.3) hence reinforcing the notion that superfluidity and Bose–Einstein condensation are two intimately related concepts. The experimental value of the speed of sound is ~ 57.5 m/s.

1.2.4 Rotation and vorticity in superfluids

Starting from time-dependent Euler–Lagrange (EL) equation (Eq. 2.6, see Chapter 2) for the time-evolution of the order parameter Ψ (Eq. 1.13, dropping the ground-state subscript and allowing φ and S to vary in time)

$$i\hbar \frac{\partial}{\partial t} \Psi(\mathbf{r}, t) = \left[-\frac{\hbar^2}{2m} \nabla^2 + \frac{\delta \mathcal{E}_c}{\delta \rho} \right] \Psi(\mathbf{r}, t) \quad (1.26)$$

one left-multiplies it with the complex conjugate of the order parameter Ψ^* and then subtract the complex conjugate of the whole expression on both sides. After some algebra and defining $\rho(\mathbf{r}, t) := N|\varphi(\mathbf{r}, t)|^2$, one arrives at the continuity equation

$$\frac{\partial \rho}{\partial t} + \nabla \cdot \mathbf{j} = 0, \quad (1.27)$$

with

$$\mathbf{j}(\mathbf{r}, t) := -\frac{i\hbar}{2m} \left[\Psi^*(\mathbf{r}, t) \nabla \Psi(\mathbf{r}, t) - \Psi(\mathbf{r}, t) \nabla \Psi^*(\mathbf{r}, t) \right] \quad (1.28)$$

$$= \rho(\mathbf{r}, t) \frac{\hbar}{m} \nabla S(\mathbf{r}, t) \quad (1.29)$$

From Eq. (1.27) it follows that the atomic number density is a conserved quantity (**HOW DOES THIS CORRELATE WITH EVAPORATION ?**).

We can identify the collective velocity \mathbf{v}_s of the superfluid through the relation

$$\mathbf{v}_s(\mathbf{r}, t) = \mathbf{j}/\rho = \frac{\hbar}{m} \nabla S(\mathbf{r}, t) \quad (1.30)$$

and we see that the rotation of the velocity field of the superfluid $\nabla \times \mathbf{v}_s = 0$, i.e. the fluid is said to be *irrotational*; a typical property of superfluids. Conversely, taking the curl $\nabla \times \mathbf{j} = \frac{\hbar}{m} \nabla \rho \times \nabla S$ we see that this is merely a restatement of the fact that one needs a gas or liquid with a non-uniform density and a non-zero phase for it to be able to support vortices.

Let us consider the illustrative example of a line vortex through the origin along the z -axis. As will be demonstrated in Section 2.2.1, this is a stationary state of the droplet Hamiltonian and therefore its time dependence is just a multiplicative factor. In cylindrical coordinates (r, φ, z) such a vortex solution has the form

$$\Psi_s(\mathbf{r}) = \sqrt{\rho(r)} e^{is\varphi}, \quad (1.31)$$

with s an integer. This is an eigenfunction of the angular momentum operator \hat{L}_z with eigenvalue

$$\hat{L}_z \Psi_s(\mathbf{r}) = \frac{\hbar}{i} \frac{\partial}{\partial \varphi} \Psi_s(\mathbf{r}) = \hbar s \Psi_s(\mathbf{r}) \quad (1.32)$$

and with expectation value

$$\langle \hat{L}_z \rangle = \langle \Psi_s | \hat{L}_z | \Psi_s \rangle \quad (1.33)$$

$$= \hbar s \left\langle \sqrt{N_0} \varphi_0 \middle| \sqrt{N_0} \varphi_0 \right\rangle \quad (1.34)$$

$$= N_0 \hbar s \quad (1.35)$$

The angular momentum is quantised and proportional to the number of bosons in the BEC fraction/superfluid. We can calculate the velocity field

$$\mathbf{v}_s = \frac{\hbar}{m} \nabla S = \frac{\hbar s}{m r} \hat{\boldsymbol{\varphi}} \quad (1.36)$$

The streamlines of \mathbf{v}_s are concentric circles, centred around the z -axis, lying in the xy -plane (see Figure 1.4). Contrary to rigid rotation fields which increase proportional to the distance from the z -axis r , the superfluid rotation field decreases proportional to distance from the z -axis $1/r$ and is singular in the origin. Calculating the circulation of the velocity field \mathbf{v}_s along a closed contour including the z -axis gives

$$\oint_{\partial\Sigma} \mathbf{v}_s \cdot d\mathbf{l} = \int_0^{2\pi} \frac{\hbar s}{m r} \hat{\boldsymbol{\varphi}} \cdot r d\varphi \hat{\boldsymbol{\varphi}} \quad (1.37)$$

$$= 2\pi s \frac{\hbar}{m} \quad (1.38)$$

There are two things to note here. Firstly, the circulation around a closed loop that encompasses the z -axis is quantised in units of \hbar/m for $s \in \mathbb{N}_{>0}$. Secondly, the value of the circulation of the velocity field does not depend on the chosen contour as long as it includes the location of the vortex. This means that all the vorticity is contained at the location where the velocity field is singular (the “core” of the vortex), at $r = 0$ along the z -axis.

Because of the pole in the velocity field, Stokes theorem will lead to the following contradiction

$$2\pi s \frac{\hbar}{m} = \oint_{\partial\Sigma} \mathbf{v}_s \cdot d\mathbf{l} = \iint_{\Sigma} \nabla \times \mathbf{v}_s \cdot d\mathbf{\Sigma} = 0 \quad (1.39)$$

and can therefore not be applied. To emphasise that all the vorticity is concentrated around the vortex core one can write formally

$$\nabla \times \mathbf{v}_s = 2\pi s \frac{\hbar}{m} \delta^{(2)}(\mathbf{r}_\perp) \hat{\mathbf{z}}, \quad (1.40)$$

where $\delta^{(2)}$ is 2-dimensional Dirac-delta function and \mathbf{r}_\perp a vector in a plane perpendicular to the vortex line.

1.3 Helium droplets

 UNTIL the 1980, most experimental and theoretical work was done on bulk systems, i.e. systems of the order of N_A number of atoms. It was only in the last couple of decades that advancements in technology enabled experimentalists to create nanoscale sized superfluid helium droplets. From the early 1990's onwards, superfluid helium nano-droplets became an active field of study, both experimentally and theoretically. Surely, the finite size of these droplets would impose some interesting properties as compared to bulk liquid helium.

The helium-helium interaction is already weak in bulk liquid helium and in finite self-bound systems such as droplets it is even weaker, e.g. the binding energy per atom is $< 7.17\text{ K}$. Because of this, helium droplets cool down very rapidly due to evaporation, reaching their limiting temperature of about 0.38 K in microseconds. Pure helium droplets are neutral systems and their properties like their size, binding energy and excitation spectra, are not easy to determine experimentally and are usually obtained by indirect methods. This didn't stop the theoreticians describe doped ${}^4\text{He}_N$ droplets using a wide variety of approaches depending on the size and character of the droplets ranging from Quantum Monte Carlo, Hypernetted-Chain/Euler-Lagrange, Variational Monte Carlo and many others.

A key property of helium droplets, in contrast to bulk helium, is their ability to pickup any kind of dopants with which they collide. Depending on the relative strength of the He-dopant interaction compared to the He-He interaction, impurities either get bound to the surface of the droplet (e.g. the alkalies) or get absorbed into their interior. They can therefore be doped with almost any kind of atomic or molecular species where they can

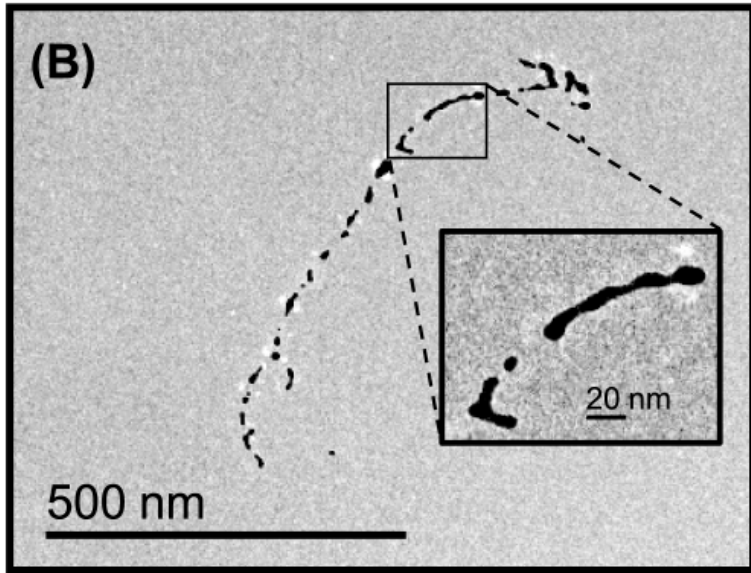


Figure 1.5: Electron-microscope image of an elongated track-shaped Ag-cluster after it is surface-deposited.

form new complexes. This enables a broad spectrum of possible experimental study. Due to the fact that helium droplets are ultra cold superfluid liquids, and therefore provide high mobility of any picked-up dopants, one can do high resolution spectroscopy studies. Having a fine control over the number of picked-up dopants[29] one can use droplets as a matrix for creating self-organising structures of polar molecules, or very cold metal clusters and study their Coulomb explosion. From the perspective of the droplet it's possible to use the dopants as gentle probes to determine the superfluid properties of helium droplets that would be inaccessible with other methods. For two examples of this see [37-39], where a dopant is used to probe the superfluid character of small ^4He droplets and [16,17] to see their limiting temperatures.

One of the most intriguing properties of superfluid helium droplets is the fact that they can host quantised vortices. Because of their ultra low temperature they are true quantum liquids and thus their vorticity and angular momentum are quantised. The existence of quantised vortices was anticipated because they have been created and observed in Bose-Einstein condensates made of dilute gases. However, the detection of quantised vortices is still experimentally challenging. Recently, Gomez, Loginov

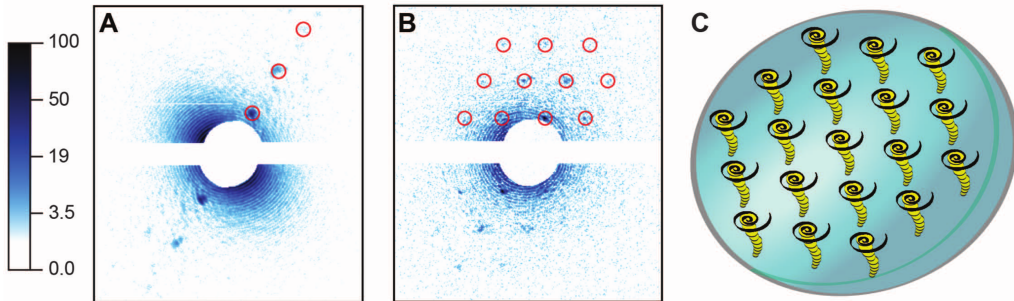


Figure 1.6: He droplets doped with Xe atoms. (A and B) X-ray diffraction images of doped droplets, displayed in a logarithmic intensity scale. (C) Droplet and embedded Xe clusters. Images in (A) and (B) correspond to tilted and parallel alignments of the vortex axes with respect to the incident x-ray beam, respectively.

and Vilesov performed experiments[PRL 108, 155302 (2012)] where vortices inside superfluid ^4He droplets, produced by the expansion of liquid helium, were traced by introducing Ag atoms which clustered along the vortex lines, into the droplets. The Ag clusters were subsequently surface-deposited and imaged via electron microscopy. The prevalence of elongated track-shaped deposits (see Figure 1.6) shows that vortices are present in droplets larger than about 300 nm and that their lifetime exceeds a few milliseconds. Two years later Gomez reported[Science 345, 906 (2014)] on the formation of quantum vortex lattices inside droplets. He used single-shot femtosecond x-ray coherent diffractive imaging to investigate the rotation of single, isolated superfluid helium-4 droplets containing $\sim 10^8$ to 10^{11} atoms. The formation of quantum vortex lattices inside the droplets was confirmed by observing the characteristic Bragg patterns from xenon clusters trapped in the vortex cores (see Figure 1.6).

A lot of work has been done on helium droplets the last few decades, both experimentally and theoretically. From the absorption spectra of alkali metal doped helium droplets, the study of doped mixed ^3He - ^4He droplets, electrons in liquid helium, to the investigation of the critical Landau velocity inside small ^4He droplet. For a comprehensive overview of work done in the last two decades, the interested reader is referred to the review papers[JLTP.Vol142.Nos.1/2(2006), IRPC.Vol36No4.621-707(2017), IRPC.Vol33No3.301-339(2014)].

1.4 Structure of the thesis

THIS thesis will consist of two parts, since the presented work focuses on two distinct areas of interest with no mutual overlap. Each part will have its own short introduction to motivate the performed research and put in a broader context. The final chapter contains a more general discussion about the presented material and will conclude with some work in progress and future prospects.

1.4.1 Part I: Excited state dynamics

In this part of the thesis the real-time dynamics of a single electronically excited rubidium (Rb) atom, residing in the surface dimple of a helium nano-droplet will be presented. The atom will be excited from its ground state $5s^2\Sigma_{1/2}$ to the $5p^2\{\Sigma, \Pi\}$ and $6p^2\{\Sigma, \Pi\}$ manifold. This will be a combined experimental and theoretical study. The results are presented in two published articles:

Imaging Excited-State Dynamics of Doped He Nanodroplets in Real-Time will focus on imaging and characterising the dynamics using femtosecond spectroscopy and time-dependent density functional theory.

Desorption dynamics of RbHe-exciples off He nanodroplets induced by spin relaxation is a combined experimental and theoretical investigation of the formation of free RbHe-exciplex molecules from laser-excited Rb-doped He nanodroplets through the mechanism of electronic spin relaxation. The role of relaxation of internal degrees of freedom of the RbHe exciplex in the desorption process has not been explicitly addressed.

1.4.2 Part II: Collisions and capture by quantised vortices

The second part investigates the real-time capture process of single xenon and argon atoms in their ground state by ${}^4\text{He}_{1000}$ droplets. Specifically it will address the interaction between a captured xenon or argon atom and a single quantised vortex line in the interior of the droplet. It will contain only theoretical investigations. The results will also be presented in two published works:

Head-on Collisions of Xe Atoms Against Superfluid ${}^4\text{He}$ Nanodroplets studies the kinematics of head-on collisions between a xenon atom and a helium droplet. This scenario is then compared to a previous study of the same

process with caesium to get a clear picture of the differences in dynamic behaviour between heliophilic and heliophobic species in said process. It also investigates different velocity regimes.

Capture of Xe and Ar atoms by quantized vortices in ^4He nanodroplets addresses the capture of xenon and argon atoms at different velocity regimes and impact factors to determine the effective cross section for capture. This investigation then repeated with a droplet hosting one quantised line vortex. Also some preliminary results are presented for a larger droplet hosting an array of 6 line vortices, lined with argon atoms.

Chapter 2

The DFT method for heavy impurities

One Functional to rule them all,
One Functional to find them,
One Functional to bring them
all and in a droplet bind them in
the Realm of Physics where
Reason lies.

some guy from LCAR

 ROM the theoretical point of view, superfluid helium must be considered as a high dimensional quantum system. Quantum Monte Carlo (QMC)^[29] and direct quantum mechanical^[30–32] calculations are the most accurate methods, but their computational demand quickly exceeds currently available computer resources when the number of helium atoms increases. Furthermore, QMC cannot describe dynamic evolution of superfluid helium in real time. To address these limitations, semi-empirical methods based on density functional theory (DFT) formalism have been introduced^[33–35]. DFT can be applied to much larger systems than QMC and allows for time-dependent formulation. As such, it offers a good compromise between accuracy and computational feasibility. The main drawback of DFT is that the exact energy functional is not known and must therefore be constructed in a semi-empirical manner. Moreover, doped helium droplets are limited to a mean-field description of the dopant-helium interaction. Nevertheless, DFT is the only method to date that can successfully reproduce results from a wide range of time-resolved experiments in superfluid helium on the atomic scale.

The starting point for the density functional method are the Hohenberg-Kohn (H-K) theorems^[36], which state that the total energy E of a many-body quantum system at $T = 0$ is a unique functional of the one-particle density

$$E[\rho] = \mathcal{T}[\rho] + \int \mathcal{E}[\rho] d\mathbf{r} \quad (2.1)$$

with

$$\rho(\mathbf{r}) = \langle \Phi | \hat{\rho}(\mathbf{r}) | \Phi \rangle := \left\langle \Phi \left| \sum_{i=1}^N \delta(\mathbf{r} - \mathbf{r}_i) \right| \Phi \right\rangle \quad (2.2)$$

the atomic density and Φ the many-body wave function. Here the total energy is split in a kinetic part $\mathcal{T}[\rho]$ and a potential part encoding the interactions. Furthermore, this unique functional gives the ground state energy if and only if the input density is the true ground state density of the system. Kohn and Sham later reformulated the theory such that we can regard the N -body ensemble of particles as a fictitious system of non-interacting particles, rewriting the above functional

$$E[\rho] = T[\rho] + \int \mathcal{E}_c[\rho] d\mathbf{r} \quad (2.3)$$

where this time

$$T = -\frac{\hbar^2}{2m} \sum_i \int \varphi_i^*(\mathbf{r}) \nabla^2 \varphi_i(\mathbf{r}) d\mathbf{r} \quad (2.4)$$

is the kinetic energy of this fictitious system and $\{\varphi_i\}$ are the single particle Kohn-Sham (K-S) orbitals corresponding to the non-interacting many-body wave function $\Phi(\mathbf{r}_1, \mathbf{r}_2, \dots, \mathbf{r}_N) = \prod_i \varphi_i(\mathbf{r}_i)$. Plugging this into the definition (Eq. 2.2) of the density operator it is straightforward to show that the density of this system is $\rho(\mathbf{r}) = \sum_i |\varphi_i(\mathbf{r})|^2$. The difference of the true kinetic energy and the fictitious one $\mathcal{T}[\rho] - T[\rho]$ has been included in the “correlation energy density” term $\mathcal{E}_c[\rho]$.

In our calculations $T = 0$ K and we therefore assume complete Bose-Einstein condensation. In this case all the helium atoms occupy the single-particle orbital φ_0 and the density becomes $\rho(\mathbf{r}) = N|\varphi_0(\mathbf{r})|^2$. As explained before in Section 1.2.2, it is customary to define an order parameter $\Psi(\mathbf{r}) := \sqrt{\rho(\mathbf{r})} = \sqrt{N}\varphi_0(\mathbf{r})$ (see Eq. 1.12) for a BEC, which is sometimes called the

effective- or macroscopic wave function. The expression for the kinetic energy (Eq. 2.4) then simplifies to

$$T[\rho] = -\frac{\hbar^2}{2m} N \langle \varphi_0 | \nabla^2 | \varphi_0 \rangle = \frac{\hbar^2}{2m} \int |\nabla \Psi|^2 d\mathbf{r} \quad (2.5)$$

To describe the time evolution of the system, the Runge-Gross theorem extends DFT in its time-dependent version TDDFT [40]. The minimisation of the total energy (Eq. 2.3) leads to the following time-dependent Euler-Lagrange (EL) equation

$$i\hbar \frac{\partial}{\partial t} \Psi(\mathbf{r}, t) = \left\{ -\frac{\hbar^2}{2m} \nabla^2 + \frac{\delta \mathcal{E}_c}{\delta \rho} \right\} \Psi(\mathbf{r}, t) := \mathcal{H}[\rho] \Psi(\mathbf{r}, t) \quad (2.6)$$

As long as we are in the thermodynamic regime the solutions $\Psi(\mathbf{r}, t)$ can be decomposed into the liquid's density and associated velocity potential field (see Section 1.2.2, 1.2.4).

Considering only eigenstates $\Psi(\mathbf{r}, t) = \Psi_0(\mathbf{r}) e^{-i\mu t/\hbar}$ of the time-independent Hamiltonian $\mathcal{H}[\rho]$ the time-dependent EL-equation reduces to a time independent one

$$\left\{ -\frac{\hbar^2}{2m} \nabla^2 + \frac{\delta \mathcal{E}_c}{\delta \rho} \right\} \Psi_0(\mathbf{r}) = \mu \Psi_0(\mathbf{r}) \quad (2.7)$$

with μ the chemical potential. Solving this equation by iteration will result in the ground state density $|\Psi_0|^2$ of the system. Within the H–K framework and the variation principle that was used to obtain these EL-equations, the nature of the minimisation is such that it gives the lowest energy for a given symmetry. This means that as long as the input state doesn't break the symmetry of the time-independent EL-equation, it minimises the energy of this state even if it doesn't lead to the ground state. This can be used to obtain a stationary vortex-line solution. With the inclusion of appropriate constraints in the energy functional the same procedure can be used to obtain helium densities with an array of vortex-lines.

2.1 The Orsay–Trento Density Functional

THE functional that is used in the work presented in this thesis is based on the Orsay-Trento (OT) functional. It uses a finite-range, non-local approach and it is, to date the most accurate model in

Model	parameters	for	the	OT-DFT	and	solid	functionals.
ϵ_{LJ} (K)	σ (\AA)	h (\AA)		c_2 (K \AA ⁶)	c_3 (K \AA ⁹)	α_s (\AA ³)	
10.22	2.556	2.190323		-2.41186×10^4	1.85850×10^6	54.31	
ρ_{0s} (\AA ⁻³)	l (\AA)	C (Hartree)		β (\AA ³)	ρ_m (\AA ⁻³)	γ_{11}	
0.04	1.	0.1		40.	0.37	-19.7544	
γ_{12} (\AA ⁻²)	α_1 (\AA ⁻²)		γ_{21}	γ_{22} (\AA ⁻²)	α_2 (\AA ⁻²)		
12.5616	1.023		-0.2395	0.0312	0.14912		

the sense that it accurately reproduces bulk properties of liquid helium at $T = 0 = P$, written as

$$\begin{aligned} \mathcal{E}_c[\rho, \mathbf{v}] = & \frac{1}{2} \int \left\{ \rho(\mathbf{r}) V_{LJ}(|\mathbf{r} - \mathbf{r}'|) \rho(\mathbf{r}') \right. \\ & + \frac{1}{2} c_2 \rho(\mathbf{r}) [\bar{\rho}(\mathbf{r})]^2 + \frac{1}{3} c_3 \rho(\mathbf{r}) [\bar{\rho}(\mathbf{r})]^3 \Big\} d\mathbf{r}' \\ & - \frac{\hbar^2}{4m} \alpha_s \int F(|\mathbf{r} - \mathbf{r}'|) \left[1 - \frac{\bar{\rho}(\mathbf{r})}{\rho_{0s}} \right] \nabla \rho(\mathbf{r}) \cdot \nabla \rho(\mathbf{r}') \left[1 - \frac{\bar{\rho}(\mathbf{r}')}{\rho_{0s}} \right] d\mathbf{r}' \\ & - \frac{m}{4} \int V_J(|\mathbf{r} - \mathbf{r}'|) \rho(\mathbf{r}) \rho(\mathbf{r}') [\mathbf{v}(\mathbf{r}) - \mathbf{v}(\mathbf{r}')]^2 d\mathbf{r}' \end{aligned} \quad (2.8)$$

The first term corresponds to a classical Lennard-Jones type two-body interaction between the helium atoms. The interaction is screened at short distances where the interaction energy is of the same order as the correlation effects:

$$V_{LJ}(r) = \begin{cases} \epsilon_{LJ} \left[\left(\frac{\sigma}{r} \right)^{12} - \left(\frac{\sigma}{r} \right)^6 \right] & \text{if } r > h \\ 0 & \text{otherwise} \end{cases} \quad (2.9)$$

In the second line, the terms corresponding to c_2 and c_3 , correct for short range correlations when $r < h$. The weighted density $\bar{\rho}$ is the average density ρ over a sphere of radius h :

$$\bar{\rho}(\mathbf{r}) = \int \Pi_h(|\mathbf{r} - \mathbf{r}'|) \rho(\mathbf{r}') d\mathbf{r}', \quad (2.10)$$

with

$$\Pi_h(r) := \begin{cases} \frac{3}{4\pi h^3} & \text{if } r \leq h \\ 0 & \text{otherwise} \end{cases} \quad (2.11)$$

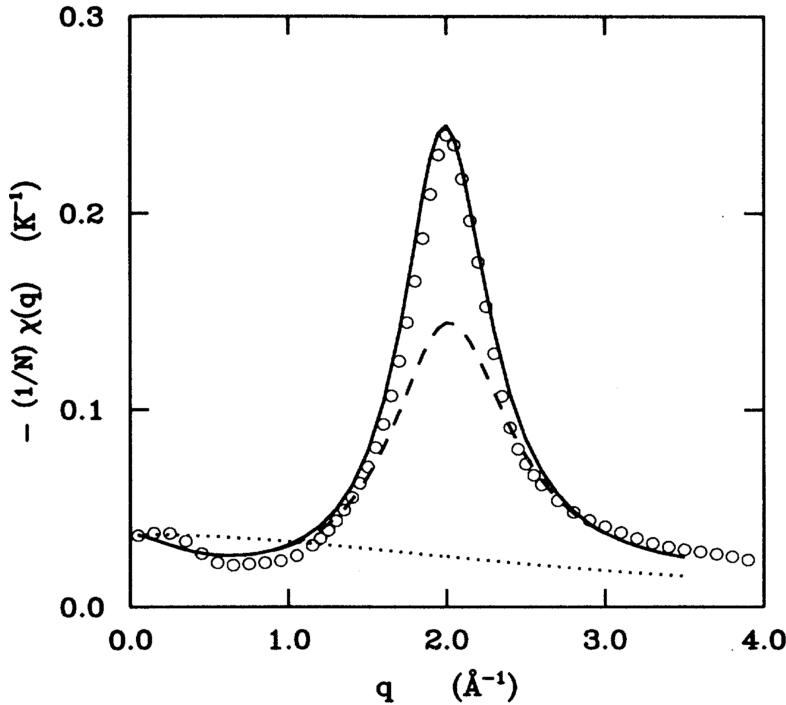


Figure 2.1: Static response function of liquid ^4He at zero pressure. Points: experimental data; dotted line: from functional of refs 15,16; dashed line: OP functional ref 1; solid line present functional.

The third line is a non-local correction to the kinetic energy (KC). It partially accounts for the difference $\mathcal{T}[\rho] - T[\rho]$ mentioned in the previous section. The gradient-gradient interaction function F is a Gaussian kernel defined as

$$F(r) = \frac{1}{l^3\sqrt{\pi^3}} e^{-r^2/l^2} \quad (2.12)$$

All the parameters are fixed to reproduce the peak of the static response function (see Fig.) in the bulk liquid. The factor $(1 - \tilde{\rho}/\rho_{0s})$ is included to match the pressure dependence of the static response function predicted by diffusion Monte Carlo calculations [ref 21 in OT paper]. The quantity $\tilde{\rho}(\mathbf{r})$ is another weighted density, calculated using F as a weight

$$\tilde{\rho}(\mathbf{r}) := \int F(|\mathbf{r} - \mathbf{r}'|)\rho(\mathbf{r}') d\mathbf{r}' \quad (2.13)$$

The density $\tilde{\rho}(\mathbf{r})$ is very close to the normal density $\rho(\mathbf{r})$ except in very inhomogeneous situations. For helium droplets one can safely use ρ instead

of $\tilde{\rho}$.

Finally, in the last line in Eq. 2.8 is called the *back-flow* term and influences the dynamic response of the system. It plays the role of a non-local kinetic energy. Since the back-flow contains the factor $\mathbf{v} - \mathbf{v}'$, as defined in Eq. 1.30 the contribution will only be non-zero whenever the order parameter Ψ is complex-valued. Which means that in the time-independent case this will only affect the vortex states. The phenomenological effective current-current interaction $V_J(r)$ is calibrated so that it reproduces the experimental phonon-roton spectrum (see Fig. 1.3):

$$\begin{aligned} V_J(r) = & (\gamma_{11} + \gamma_{12} r^2) e^{-\alpha_1 r^2} \\ & + (\gamma_{21} + \gamma_{22} r^2) e^{-\alpha_2 r^2} \end{aligned} \quad (2.14)$$

All the parameters of the functional are given in Table 2.1.

2.1.1 The Solid-OT Density Functional

In the presence of highly inhomogeneous liquid densities, e.g. atomic impurities with a very strong He-X interaction, the OT-functional Eq. (2.8) becomes numerically unstable. To deal with this problem an additional cut-off can be used

$$\mathcal{E}_{\text{sol}} := C\rho(\mathbf{r})\{1 + \tanh(\beta[\rho(\mathbf{r}) - \rho_m])\} \quad (2.15)$$

where the model parameters $\{C, \beta, \rho_m\}$ are specified in Table 2.1. Including this term in the OT-functional prevents excessive density build-up. \mathcal{E}_{sol} only starts to deviate from zero whenever the liquid density ρ is comparable to ρ_m or larger. Therefore, inclusion of this term in the functional does not alter the density distribution. This penalty term was originally developed to account for the liquid-solid phase transition of ${}^4\text{He}$ [61,62]. The functional that has been used to obtain the result presented in this work is what we call the “Solid-OT-DFT functional”. It consists of the first three terms of the original OT-functional Eq. (2.8), plus \mathcal{E}_{sol}

$$\begin{aligned} \mathcal{E}_c^{\text{sol}}[\rho] = & \frac{1}{2} \int \left\{ \rho(\mathbf{r})V_{LJ}(|\mathbf{r} - \mathbf{r}'|)\rho(\mathbf{r}') \right. \\ & + \frac{1}{2}c_2\rho(\mathbf{r})[\bar{\rho}(\mathbf{r})]^2 + \frac{1}{3}c_3\rho(\mathbf{r})[\bar{\rho}(\mathbf{r})]^3 \Big\} d\mathbf{r}' \\ & + C\rho(\mathbf{r})\{1 + \tanh(\beta[\rho(\mathbf{r}) - \rho_m])\} \end{aligned} \quad (2.16)$$

2.2 Static calculations

N the work presented here all the impurities are heavy compared to the mass of ^4He , e.g. the mass of Rubidium is about 21 times larger than that of Helium, Xenon roughly 33 times and Argon about 10 times. Therefore we will treat the centre of mass motion of the impurities as classical. In the DFT derived EL-equations this will be modelled as an external field V_X

$$E[\rho] \rightarrow E[\rho] + \int \rho(\mathbf{r}) V_X(|\mathbf{r} - \mathbf{r}_I|) d\mathbf{r} \quad (2.17)$$

where X is the label of the used ^4He -impurity pair interaction and \mathbf{r}_I is the position of the impurity. Varying the modified functional to minimise the energy one now finds a new EL-equation in which the helium-impurity interaction is included:

$$\left\{ -\frac{\hbar^2}{2m_4} \nabla^2 + \frac{\delta\mathcal{E}_c}{\delta\rho} + V_X(|\mathbf{r} - \mathbf{r}_I|) \right\} \Psi(\mathbf{r}) = \mu \Psi(\mathbf{r}) \quad (2.18)$$

This equation is then solved in a self-consistent way by the Imaginary Time Method[ref 69] (ITM) in cartesian coordinates upon convergence. The calculations are performed in three dimensions without imposing any symmetries that are present in the external potential. All the quantities are discretised on evenly spaced cartesian grid with a grid constant that is typically of the order of 0.4. The differential operators are evaluated using a k -point finite difference method where most of the time $k = 13$ is sufficiently accurate. The integrals in the density-functional can be expressed as convolutions and can therefore be evaluated in momentum-space by exploiting the convolution theorem, using proprietary highly optimised parallel Fast Fourier Transform algorithms.

2.2.1 Producing vortical states

The helium density that minimises the energy of the vortical states Ψ_s (Eq. 1.31), introduced in Section 1.2.4 can be obtained by solving the same EL-equation as for a vortex-free droplet. This becomes more clear when we write Eq. (2.7) in cylindrical coordinates and then substitute Ψ_0 by Ψ_s :

$$\left\{ -\frac{\hbar^2}{2m} \left[\frac{1}{r} \frac{\partial}{\partial r} \left(r \frac{\partial}{\partial r} \right) - \frac{s^2}{r^2} \right] + \frac{\delta\mathcal{E}_c}{\delta\rho} \right\} \Psi_s(\mathbf{r}) = \mu \Psi_s(\mathbf{r}) \quad (2.19)$$

Written like this it is evident that the ground state Ψ_0 is just the special case for $s = 0$. Obtaining the solution using the ITM works as long as the solution has overlap with initial guess for the order parameter. Starting with a trial order parameter similar to Ψ_s will guarantee this. To do this we use the “imprinting” technique where we use the ground state density of a previously obtained vortex-free droplet and multiply it with a normalised complex factor

$$\Psi(\mathbf{r}) = \sqrt{\rho_0(\mathbf{r})} \times \frac{x + iy}{\sqrt{x^2 + y^2}} \quad (2.20)$$

where ρ_0 is the ground state density of the vortex-droplet. In cylindrical coordinates this factor is equivalent to the one in Eq. (1.31) for $s = 1$.

This changes for droplets with two or more vortices, where the cylindrical symmetry is broken and the solutions are no longer solutions of Eq. (2.19) nor eigenfunctions of the angular momentum operator. In this case the time-independent EL-equation has to be modified to include a rotational constraint

$$\mathcal{H} \rightarrow \mathcal{H} - \Omega \hat{L}_z \quad (2.21)$$

such that for a suitable choice of Ω the vortex-array solution becomes favourable to the ground state. Since these states are no longer eigenstates of the original time-dependent Hamiltonian, these states are no longer stationary and will start to rotate with frequency Ω . The initial guess for a droplet with n_v vortices can be produced using the same imprinting method as mentioned before

$$\Psi(\mathbf{r}) = \sqrt{\rho_0(\mathbf{r})} \times \prod_{j=1}^{n_v} \left[\frac{(x - x_j) + i(y - y_j)}{\sqrt{(x - x_j)^2 + (y - y_j)^2}} \right] \quad (2.22)$$

where ρ_0 is again the ground state density of the vortex-free droplet and (x_j, y_j) is the initial position of the j -th vortex-line parallel to the z -axis.

2.3 Dynamic calculations

 or the dynamic evolution of atomic impurities excited from ns -states to $n's$ -states, we do not need to keep track of the evolution of the electronic state of the impurity since it keeps its spherically

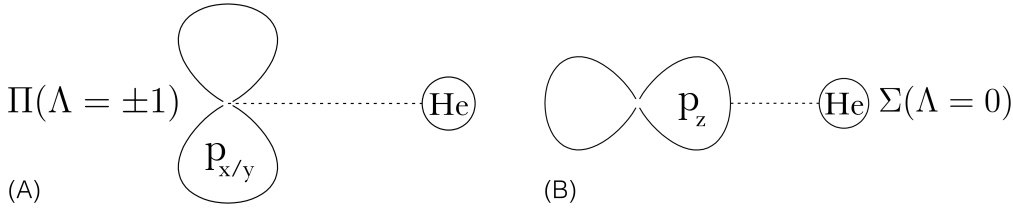


Figure 2.2: Level splitting of the p-orbitals in the presence of helium, that breaks the spherical symmetry. (A) A double degenerate $n'p_{x/y}$ -orbital and (B) a single $n'p_z$ -orbital. (Illustration courtesy of M. Martinez)

symmetric orbital. In this case we only need to describe the time evolution of the centre of mass coordinate of the impurity. As in the statics, because of the large atomic mass of the impurity compared to helium, the time evolution of the centre of mass coordinate of the impurity is treated classically. To obtain the correct energy for the whole droplet-impurity system the energy functional needs to be extended to include the impurities centre of mass motion and the impurity-helium interaction

$$E[\rho] \rightarrow E[\rho] + \frac{p_I^2}{2m_I} + \int \rho(\mathbf{r}) V_{X^*}(|\mathbf{r} - \mathbf{r}_I|) d\mathbf{r} \quad (2.23)$$

where p_I is the classical momentum of the impurity, m_I is the impurity mass and V_{X^*} is the $X-{}^4\text{He}$ pair potential for a ground-, excited- or ionised state. The equations of motion for the time evolution of the order parameter $\Psi(\mathbf{r}, t)$ and the centre of mass of the impurity $\ddot{\mathbf{r}}_I$ are

$$\begin{aligned} i\hbar \frac{\partial}{\partial t} \Psi &= \left[-\frac{\hbar^2}{2m_4} \nabla^2 + \frac{\delta \mathcal{E}_c}{\delta \rho} + V_{X^*}(|\mathbf{r} - \mathbf{r}_I|) \right] \Psi \\ m_I \ddot{\mathbf{r}}_I &= -\nabla_{\mathbf{r}_I} \left[\int \rho(\mathbf{r}) V_{X^*}(|\mathbf{r} - \mathbf{r}_I|) d\mathbf{r} \right] \\ &= - \int V_{X^*}(|\mathbf{r} - \mathbf{r}_I|) \nabla \rho(\mathbf{r}) d\mathbf{r} \end{aligned} \quad (2.24)$$

2.3.1 The DIM model

The situation becomes slightly more complicated for ns -states excited to $n'p$ -states (effective one-electron excited ${}^2\text{P}$ -states). Since the p-orbital is no longer spherically symmetric, we also need to include a description for the time evolution of the orientation of the p-orbital. To do this we use the diatomic model (DIM). The interaction between a helium atom (${}^1\text{S}_0$ -state)

and the triple degenerate $L = 1$ electronic state of the impurity partially lifts the degeneracy so that the interaction can be decomposed into a Σ -state and a double degenerate Π -state (see Fig. 2.2). In the cylindrical symmetry of the DIM it is customary to use the molecular term symbol $^{2S+1}\Lambda_\Omega$ to label the levels. Here S is the total spin angular momentum (and $2S + 1$ the spin multiplicity), Λ is the modulus of the total orbital angular momentum and Ω is the total angular momentum, all projected along the internuclear axis. Following the spectroscopic notation the orbitals corresponding to $\Lambda = 0, 1, 2, 3, \dots$ are labeled $\Sigma, \Pi, \Delta, \Phi, \dots$. The interaction between a helium atom and the impurity's electronic structure can be expressed in an uncoupled basis

$$|p_{im}\rangle \in \{|p_{xm}\rangle, |p_{ym}\rangle, |p_{zm}\rangle\} \quad (2.25)$$

of real one-electron p-orbitals oriented along the internuclear axis (see Fig. 2.3). The helium-impurity interaction matrix is given by

$$\begin{aligned} \mathcal{V}^{DIM}(r_m) &= V_\Pi(r_m)(|p_{xm}\rangle\langle p_{xm}| + |p_{ym}\rangle\langle p_{ym}|) + V_\Sigma(r_m)|p_{zm}\rangle\langle p_{zm}| \\ &= V_\Pi(r_m)(\mathbb{1}_3 - |p_{zm}\rangle\langle p_{zm}|) + V_\Sigma(r_m)|p_{zm}\rangle\langle p_{zm}| \\ &= V_\Pi(r_m)\mathbb{1}_3 + [V_\Sigma(r_m) - V_\Pi(r_m)]|p_{zm}\rangle\langle p_{zm}| \end{aligned} \quad (2.26)$$

where r_m is the modulus of the interatomic separation vector and V_Π and V_Σ are the Π and Σ impurity-He pair potentials in the absence of spin-orbit coupling. For a system consisting of N helium atoms the total interaction energy is calculated by summing over all the contributions of the N individual ${}^4\text{He}$ -X contributions (DIM^[?])

$$\mathcal{U}^{DIM}(\mathbf{r}_I) = \sum_{m=1}^N \mathcal{V}^{DIM}(r_m) \quad (2.27)$$

It is more convenient to express the interaction in a basis common to all impurity-helium pairs, instead of a basis that depends on the particular impurity-helium pair chosen. To do this we apply a rotation $\mathcal{R}_m : \hat{\mathbf{z}}_m \mapsto \hat{\mathbf{z}} \propto \mathbf{r}_I$, so that the matrix corresponding to the m^{th} ${}^4\text{He}$ atom expressed in the common basis is given by

$$|p_{zm}\rangle\langle p_{zm}| = \mathcal{R}_m |p_z\rangle\langle p_z| \mathcal{R}_m^{-1} \quad (2.28)$$

It can be shown that the elements of this matrix in cartesian coordinates are of the form

$$\langle p_i | \mathcal{R}_m | p_z \rangle\langle p_z | \mathcal{R}_m^{-1} | p_j \rangle = \frac{r_{im} r_{jm}}{\|\mathbf{r}_m\|^2} \quad (2.29)$$

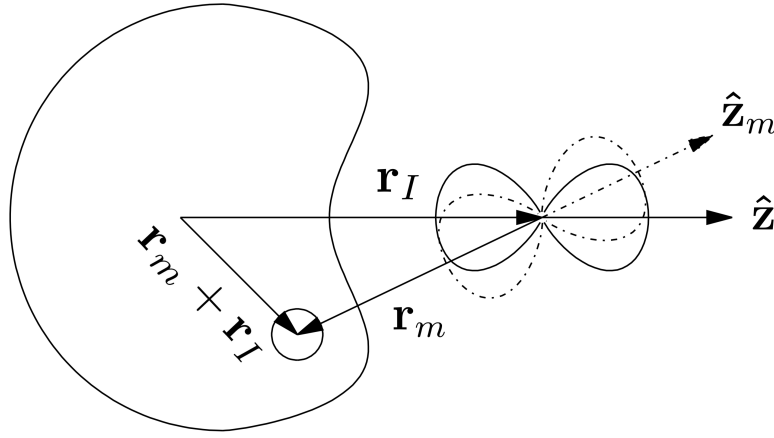


Figure 2.3: The set of axis defined in the DIM description (illustration courtesy of M. Martinez).

where $(i, j) \in \{x, y, z\}$. With these definitions we can write the matrix elements U_{ij}^{DIM} of the interaction energy \mathcal{U}^{DIM}

$$U_{ij}^{\text{DIM}}(\mathbf{r}_I) = \langle p_i | \mathcal{U}^{\text{DIM}} | p_j \rangle = \sum_{m=1}^N V_{ij}^{\text{DIM}}(r_m) \quad (2.30)$$

where

$$V_{ij}^{\text{DIM}}(r_m) := V_{\Pi}(r_m) \delta_{ij} + \left[V_{\Sigma}(r_m) - V_{\Pi}(r_m) \right] \frac{r_{im} r_{jm}}{\|\mathbf{r}_m\|^2} \quad (2.31)$$

are the matrix elements of \mathcal{V}^{DIM} expressed in the common basis. Since we are working with a continuous helium density $\rho(\mathbf{r})$ and not with discrete atoms the summation over N helium atoms in the previous expression is replaced by an integral over the density $\sum_m \rightarrow \int \rho(\mathbf{r}) d\mathbf{r}$ which finally gives for the matrix element U_{ij}^{DIM}

$$U_{ij}^{\text{DIM}}(\mathbf{r}_I) = \int \rho(\mathbf{r} + \mathbf{r}_I) V_{ij}^{\text{DIM}}(r) d\mathbf{r} \quad (2.32)$$

The eigenvalues $U_k^{\text{np}}(\mathbf{r}_I)$ of this real symmetric matrix define the potential energy curves (PECs) as a function of the distance between the surrounding helium and the impurity.

2.3.2 Including spin-orbit coupling

For the study of the alkali metal Rb in this work, the spin-orbit (SO) splitting of the energy levels is comparable to the splitting of the orbital angular momentum levels $L = 0$ and $L = \pm 1$ due to the interaction with the helium. Therefore the spin-orbit interaction needs to be included in the total interaction Hamiltonian.

The total Hamiltonian is given by the sum of the DIM-interaction and the SO-interaction $\mathcal{H} = \mathcal{U}^{DIM} + \mathcal{V}^{SO}$. The SO-matrix is defined

$$\mathcal{V}^{SO} = \frac{1}{2}A_{\ell s}(\mathbf{J}^2 - \mathbf{L}^2 - \mathbf{S}^2) \quad (2.33)$$

with $\mathbf{J} = \mathbf{L} + \mathbf{S}$. The coupling constant $A_{\ell s}$ is usually approximated by that of the free atom^[37]. We can extend the DIM basis Eq. (2.25) to include the projection of the electron spin $s = \{\uparrow, \downarrow\}$ corresponding to the quantum numbers $m_s = \{\frac{1}{2}, -\frac{1}{2}\}$:

$$|p_i, s\rangle \in \{|p_x, \uparrow\rangle, |p_x, \downarrow\rangle, |p_y, \uparrow\rangle, |p_y, \downarrow\rangle, |p_z, \uparrow\rangle, |p_z, \downarrow\rangle\}. \quad (2.34)$$

In this basis the \mathcal{V}^{SO} is given by

$$\mathcal{V}^{SO} = \frac{1}{2}A_{\ell s} \begin{pmatrix} 0 & 0 & -i & 0 & 0 & 1 \\ 0 & 0 & 0 & i & -1 & 0 \\ i & 0 & 0 & 0 & 0 & -i \\ 0 & -i & 0 & 0 & -i & 0 \\ 0 & -1 & 0 & i & 0 & 0 \\ 1 & 0 & i & 0 & 0 & 0 \end{pmatrix} \quad (2.35)$$

Kramers' theorem states that the two-fold degeneracy of the levels originating from total half-integer spin cannot be broken by electrostatic interactions^[38]. Therefore all the electronic eigenstates of \mathcal{H} are doubly degenerate. Diagonalisation of \mathcal{H} yields three doubly degenerate PECs between the impurity and surrounding helium.

The dynamic evolution of the electronic excited state of the impurity is described by introducing an additional degree of freedom, a 6-component vector $|\lambda\rangle$, which describes the coefficients of the electronic state in the $\{|p_i, s\rangle\}$ basis

$$|\lambda(t)\rangle = \sum_{\substack{i=\{x,y,z\} \\ s=\{\uparrow,\downarrow\}}} \lambda_{is}(t) |p_i, s\rangle \quad (2.36)$$

such that $\|\langle \lambda | \lambda \rangle\|^2 = 1$. The complete set of variables required to describe the system consists of the complex valued effective wave function for helium $\Psi(\mathbf{r}, t)$ with $\rho(\mathbf{r}, t) = |\Psi(\mathbf{r}, t)|^2$, the impurity position $\mathbf{r}_I(t)$, and the 6-dimensional complex vector to determine its electronic wave function $|\lambda(t)\rangle$. The total energy of the impurity- ${}^4\text{He}_N$ complex after excitation to the ${}^2\text{P}$ manifold is

$$\begin{aligned} E[\Psi, \mathbf{r}_I, \lambda] &= \frac{\hbar^2}{2m} \int |\nabla \Psi|^2 d\mathbf{r} + \int \mathcal{E}_c[\rho] d\mathbf{r} \\ &\quad + \frac{p_I^2}{2m_I} + \int \rho(\mathbf{r}) V_\lambda(\mathbf{r} - \mathbf{r}_I) d\mathbf{r} + \langle \lambda | \mathcal{V}^{SO} | \lambda \rangle \end{aligned} \quad (2.37)$$

where V_λ is defined as

$$V_\lambda(\mathbf{r}) := \langle \lambda | \mathcal{V}^{DIM} | \lambda \rangle = \sum_{ijss'} \lambda_{is}^* V_{ijss'}^{DIM}(\mathbf{r}) \lambda_{js'} \quad (2.38)$$

and the components of the 6×6 matrix \mathcal{V}^{DIM} given by

$$V_{ijss'}^{DIM}(\mathbf{r}) = V_{ij}^{DIM} \delta_{ss'} = \left\{ V_\Pi(r) \delta_{ij} + [V_\Sigma(r) - V_\Pi(r)] \frac{r_i r_j}{\|\mathbf{r}_m\|^2} \right\} \delta_{ss'} \quad (2.39)$$

Unlike for the static DFT case, the time evolution of the system is obtained by minimising the following action

$$\begin{aligned} A[\Psi, \mathbf{r}_I, \lambda] &= \int \left\{ E[\Psi, \mathbf{r}_I, \lambda] - i\hbar \int \Psi^*(\mathbf{r}) \frac{\partial}{\partial t} \Psi(\mathbf{r}) d\mathbf{r} \right. \\ &\quad \left. - i\hbar \left\langle \lambda \left| \frac{\partial}{\partial t} \right| \lambda \right\rangle - \frac{1}{2} m_I \ddot{\mathbf{r}}_I^2 \right\} dt \end{aligned} \quad (2.40)$$

Variation of the action A with respect to $\{\Psi^*, \langle \lambda |, \mathbf{r}_I\}$ yields the following three coupled EL-equations

$$\begin{aligned} i\hbar \frac{\partial}{\partial t} \Psi &= \left[-\frac{\hbar^2}{2m} \nabla^2 + \frac{\delta \mathcal{E}_c}{\delta \rho(\mathbf{r})} + V_\lambda(\mathbf{r} - \mathbf{r}_I) \right] \Psi \\ i\hbar \frac{\partial}{\partial t} |\lambda\rangle &= \mathcal{H} |\lambda\rangle \\ m_I \ddot{\mathbf{r}}_I &= -\nabla_{\mathbf{r}_I} \left[\int \rho(\mathbf{r}) V_\lambda(\mathbf{r} - \mathbf{r}_I) d\mathbf{r} \right] = - \int V_\lambda(\mathbf{r} - \mathbf{r}_I) \nabla \rho(\mathbf{r}) d\mathbf{r} \end{aligned} \quad (2.41)$$

where the explicit time dependence of the variables is omitted for clarity. The second line of Eq. (2.41) is a 6×6 matrix equation with the matrix elements of \mathcal{H} given by

$$H_{ijss'} = U_{ijss'}^{DIM} + V_{ijss'}^{SO} = \int \rho(\mathbf{r}) V_{ijss'}^{DIM}(\mathbf{r} - \mathbf{r}_I) d\mathbf{r} + V_{ijss'}^{SO} \quad (2.42)$$

In the cases that SO-coupling can be neglected the 6-dimensional electronic state vector $|\lambda\rangle$ reduces to the 3-dimensional vector

$$|\lambda(t)\rangle = \sum_{i=\{x,y,z\}} \lambda_i(t) |p_i\rangle \quad (2.43)$$

and the 6×6 matrix \mathcal{H} reduces to the 3×3 matrix of Eq. (2.32) with elements

$$H_{ij} = U_{ij}^{DIM} = \int \rho(\mathbf{r}) V_{ij}^{DIM}(\mathbf{r} - \mathbf{r}_I) d\mathbf{r} \quad (2.44)$$

For the technical details about how this method is implemented the interested reader is directed to [39]. For the collection of Fortran code that has been used to obtain the results presented here see [??]. For the manual to use the code see [39].

Part I

Photo-excitation dynamics of alkalis

Chapter 3

Introduction

3.1 Imaging Excited-State Dynamics

As mentioned in the introduction He nanodroplets capable of efficiently capturing and cooling atoms, molecules, and clusters for spectroscopy and dynamics studies[1,2]. So far, time-resolved experiments on He droplets doped with alkali (Ak) metal atoms were mostly focused on the formation of AkHe exciplexes induced by laser excitation[15-18,22,23]. The concurrent desorption of these excited species was estimated to proceed on a picosecond time scale[9,10,13,24-26]. This estimate, sufficient for studies employing nanosecond laser pulses, clearly lacks precision for experiments with sub-picosecond time resolution. Thus in the previous measurements as well as in experiments focusing on electronic and vibrational coherences of Ak atoms and molecules[17,19,22,23,27] the exact location of the dopants, attached to the droplets or in the vacuum, has remained somewhat uncertain.

Here we report a combined experimental and theoretical investigation of the excited-state dynamics of doped He nanodroplets in real time. The combination of fs pump-probe spectroscopy with velocity map imaging (VMI)[28] allows us to clearly disentangle complex formation, desorption, and ion solvation. As a model system, we investigate He droplets doped with single rubidium (Rb) atoms. Ground-state Rb atoms and small molecules are weakly bound to the He droplet surface in a dimple structure[29-31]. Therefore, the ejection dynamics of the excited Rb atom (Rb^*) is not affected by processes such as the interaction of Rb^* with density waves traveling in the bulk of the droplet, as for Ag^* [11].

3.2 Desorption dynamics of RbHe-exciples

Understanding the photochemistry of condensed phase systems and surfaces is essential in many research areas, such as atmospheric sciences[1] and photocatalysis[2]. However, complex diabatic couplings of electronic and motional degrees of freedom of various subunits of the system often present a major challenge. Moreover, the heterogeneity of multi-component solid or liquid systems and experimental difficulties in precisely preparing the sample and reproducing measurements tend to make it hard to unravel specific elementary reactions. In this respect, He nanodroplets doped with single atoms or well-defined complexes are ideal model systems for studying photodynamical processes in the condensed phase, both experimentally and theoretically. Due to their ultra-low temperature (0.37 K) and their quantum fluid nature, He nanodroplets have a homogeneous density distribution and dopant particles aggregate into cold clusters mostly inside the droplets[3,4]. Only alkali metal atoms and small clusters are attached to He droplets in loosely bound dimple-like states at the droplet surface[5-12].

While He nanodroplets are extremely inert and weakly-perturbing matrices for spectroscopy of embedded atoms and molecules in their electronic ground state, a rich photochemical dynamics is initiated upon electronic excitation or ionisation[13,14], involving electronic relaxation[15-18], the ejection of the dopant out of the droplet[19-26], chemical reactions within the dopant complex[27-29], and even among the dopant and the surrounding He[20,30-39].

As a general trend, electronically excited dopant atoms and small molecules tend to be ejected out of He droplets either as bare particles or with a few He atoms attached to them[15,40-42]. In particular, all atomic alkali species promptly desorb off the droplet surface, the only exceptions being Rb and Cs atoms in their lowest excited states[43,44]. The dynamics of the desorption process has recently been studied at an increasing level of detail[16,21,23,45], including time-resolved experiments and simulations[24,26]. The focus was on the competing processes of desorption of the dopant induced by laser excitation, and the dopant falling back into the He droplet upon photoionisation. The latter occurred at short pump-probe delay times when the distance between the photoion and the droplet was short enough for ion-He attraction to be effective.

The purpose of this work is to extend our joint experimental and theo-

retical study of the photodynamics of Rb-doped He nanodroplets to RbHe exciplexes[23,26]. The simultaneous effect of pairwise Rb-He attraction and repulsion of Rb from the He droplet as a whole results in an intricate dynamics, and interpretations have remained somewhat ambiguous with respect to the exciplex formation mechanism and time scale, as well as the origin of free exciplexes detached from the He droplets[16,26,30,33,34]. In particular the role of relaxation of internal degrees of freedom of the RbHe exciplex in the desorption process has not been explicitly addressed[46,47]. Here, we discuss in detail the interplay of the RbHe formation dynamics, the RbHe desorption off the He droplet surface, and the fall-back of $[RbHe]^+$ created by photoionization in femtosecond pump-probe experiments[24,26,31]. We find that electronic spin-relaxation is the main process driving the desorption of RbHe off the He droplet.

Chapter 4

Results

4.1 Imaging Excited-State Dynamics

Imaging Excited-State Dynamics of Doped He Nanodroplets in Real-Time

Johannes von Vangerow,[†] Fran ois Coppens,[‡] Antonio Leal,[§] Marti Pi,[§] Manuel Barranco,^{§,‡} Nadine Halberstadt,[‡] Frank Stienkemeier,[†] and Marcel Mudrich^{*,†,¶}

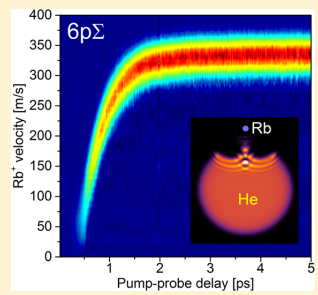
[†]Physikalisches Institut, Universit t Freiburg, Hermann-Herder-Str. 3, 79104 Freiburg, Germany

[‡]Laboratoire des Collisions, Agr gats, R activit , IRSAMC, UMR 5589, CNRS et Universit  Paul Sabatier-Toulouse 3, 118 route de Narbonne, F-31062 Toulouse Cedex 09, France

[§]Departament FQA, Facultat de F sica, and IN2UB, Universitat de Barcelona, Diagonal 645, 08028 Barcelona, Spain

Supporting Information

ABSTRACT: The real-time dynamics of excited alkali metal atoms (Rb) attached to quantum fluid He nanodroplets is investigated using femtosecond imaging spectroscopy and time-dependent density functional theory. We disentangle the competing dynamics of desorption of excited Rb atoms off the He droplet surface and solvation inside the droplet interior as the Rb atom is ionized. For Rb excited to the 5p and 6p states, desorption occurs on starkly differing time scales (~ 100 versus ~ 1 ps, respectively). The comparison between theory and experiment indicates that desorption proceeds either impulsively (6p) or in a transition regime between impulsive dissociation and complex desorption (5p).



He nanodroplets are intriguing quantum fluid objects of finite size capable of efficiently capturing and cooling atoms, molecules, and clusters for spectroscopy and dynamics studies.^{1,2} Upon electronic excitation, embedded atoms and small molecules tend to move toward the droplet surface and may be ejected due to short-range electron-He repulsion.³ In contrast, cations experience attractive forces toward the He droplets mediated by electrostatic polarization, which draw them to the droplet interior, where they may form snowball complexes.^{4–7} These two opposing trends lead to a rich dynamics initiated by photoexcitation of embedded species involving desorption, electronic relaxation, complex formation, as well as solvation and desolvation of the ionized impurity. Similar dynamics have been observed when exciting pure He droplets with extreme-ultraviolet radiation²⁰ as well as for other types of clusters.²¹

So far, time-resolved experiments on He droplets doped with alkali (Ak) metal atoms were mostly focused on the formation of AkHe exciplexes induced by laser excitation.^{15–18,22,23} The concurrent desorption of these excited species was estimated to proceed on a picosecond time scale.^{9,10,13,24–26} This estimate, sufficient for studies employing nanosecond laser pulses, clearly lacks precision for experiments with sub-picosecond time resolution. Thus in the previous measurements as well as in experiments focusing on electronic and vibrational coherences of Ak atoms and molecules^{17,19,22,23,27} the exact location of the dopants, attached to the droplets or in the vacuum, has remained somewhat uncertain.

Here we report a combined experimental and theoretical investigation of the excited-state dynamics of doped He nanodroplets in real time. The combination of fs pump-probe spectroscopy with velocity map imaging (VMI)²⁸ allows us to clearly disentangle complex formation, desorption, and ion solvation. As a model system, we investigate He droplets doped with single rubidium (Rb) atoms. Ground-state Rb atoms and small molecules are weakly bound to the He droplet surface in a dimple structure.^{29–31} Therefore, the ejection dynamics of the excited Rb atom (Rb*) is not affected by processes such as the interaction of Rb* with density waves traveling in the bulk of the droplet, as for Ag*.¹¹

We excite droplet-bound Rb atoms to states correlating either to the lowest excited state 5p or to the higher lying state 6p. The dynamics is probed by ionizing Rb* at variable delay times between photoexcitation ($t = 0$) and photoionization ($t = t_+$) while monitoring the velocity and signal yield of Rb⁺ ions. A simulation based on time-dependent density functional theory (TDDFT) gives us insight into the time evolution both of Rb* and of the Rb⁺ ion taking into account the quantum fluid properties of the He environment. Using these techniques, we follow the trajectory of the excited and subsequently ionized Rb atom in detail as it escapes from the droplet surface or submerges into it. Although separated by only ~ 1.4 eV in energy, the two states 5p and 6p are found to feature time

Received: November 6, 2016

Accepted: December 20, 2016

Published: December 20, 2016

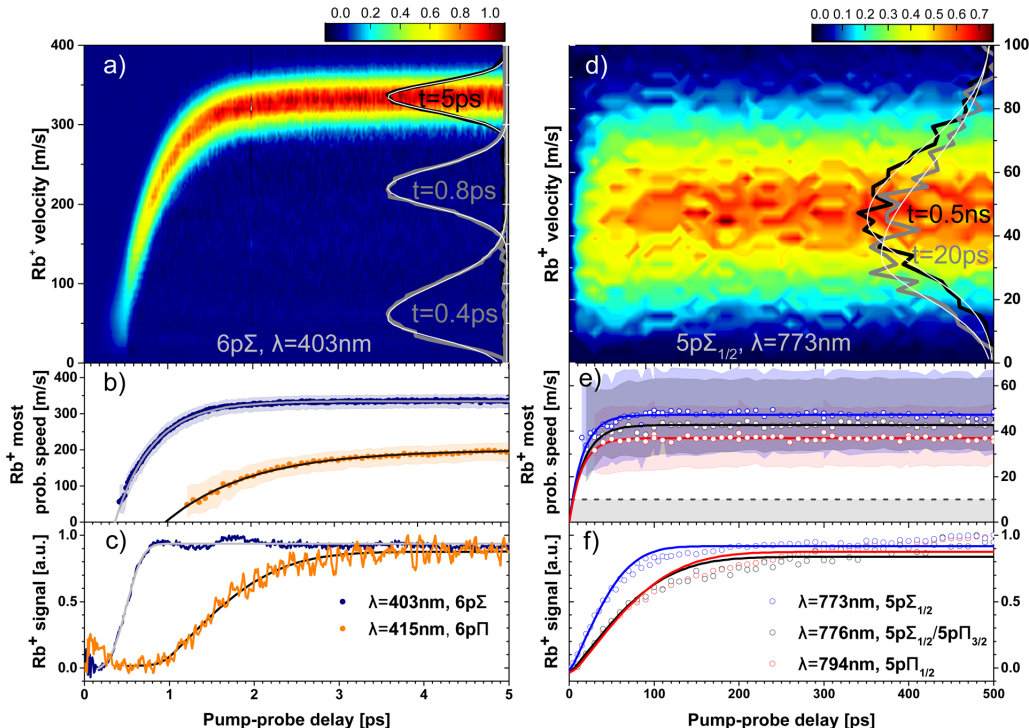


Figure 1. Rb⁺ transient speed distributions (a,d), most probable speeds (b,e), and ion yields (c,f) resulting from photoexcitation to He droplet perturbed states correlating to 6p (left column) and 5p states (right column) of Rb (pump) and subsequent ionization (probe). The shaded areas (b,e) indicate the left and right $\epsilon^{-1/2}$ widths of the speed distributions. The shaded area at the bottom of panel e depicts the experimental resolution. The smooth lines are fits to the data (see text).

constants of the desorption dynamics differing by about 2 orders of magnitude.

Figure 1a,d shows examples of measured Rb⁺ transient speed distributions derived from the VMIs by angular integration. From these distributions we infer the most probable speeds (b,e) by fitting a skewed Gaussian distribution as illustrated by selected speed distributions shown on the right-hand sides of Figure 1a,d.³⁴ For the droplet perturbed Rb 6p states the most probable speeds (b) as well as the total Rb⁺ ion yields (c) show a steep rise within a few picoseconds. In contrast, for the droplet perturbed 5p states we record speed distributions (e) close to our experimental resolution of ~10 m/s (shaded gray area) and ion yields (f) which increase within hundreds of picoseconds.

For the droplet perturbed Rb 6p excitations, the transient ion yield curves (c) have previously been interpreted in terms of the competing effects of repulsion from the He droplet surface and attraction of Rb⁺ toward it.¹⁴ Accordingly, the slower dynamics of the 6pΠ state compared with that of the 6pΣ state is due to the weaker repulsion from the droplet. We term “fall-back time”, τ_c , the critical delay discriminating between the ion falling back into the droplet and the ion escaping into the vacuum. It is obtained by fitting the 6p and 5p ion yield data with piecewisely defined asymmetric error function $I(t) = A_0 + A \cdot \{[t \leq \mu] \sigma_- \cdot \text{erf}[(t - \mu)/\sigma_-] + [t > \mu] \sigma_+ \cdot \text{erf}[(t - \mu)/\sigma_+]\}$, where σ_{\mp} denote widths on the right and left side of the inflection point μ . τ_c is obtained from computing the 50% rise time of that fit function. The evolution of the most probable

speeds \hat{v} is fitted by $\hat{v}(t) = \hat{v}_f \{1 - \exp[-\ln 2 \cdot (t - t_0)/\tau_v]\}$, from which we obtain the characteristic 50% rise times $\tau_v = t_0 + \tau_c$.

Note that for each applied pump–probe delay we measure the final velocity distribution of the ion after it has fully escaped from the droplet. Therefore, the experiment does not give direct access to the desorption dynamics of the neutral Rb^{*} atom. To get a complete picture of the dynamics, simulations based on the TDDFT approach are carried out using the functional of ref 35. Details of this approach have been described before.^{9,11,32} In short, we consider droplets consisting of $N = 1000$ atoms doped with one Rb atom. Because of its large mass compared with that of He we describe the dynamics of the Rb atom classically. The simulations of the full pump–probe sequence consist of two steps: the propagation of Rb^{*} in the excited state starting at $t = 0$ (step 1) and the propagation of the Rb⁺ ion at times $t > t_+$ (step 2). This is achieved by solving the coupled 3D TDDFT and Newton’s equations for the He droplet and the Rb impurity, respectively.

In step 1, the Rb^{*}–droplet interaction is obtained from the Rb^{*}–He $n\Sigma$ and $n\Pi$ pair potentials³⁶ with $n = 5$ and 6, and includes the spin–orbit interaction in the usual He–Rb^{*} distance-independent way; it also allows for the dynamic evolution of the internal electronic state of the Rb^{*} atom.¹¹ In step 2, the coupled dynamical equations are now simpler as they do not explicitly take into account the electronic structure of the closed-shell Rb⁺ ion. In all simulations, a spatial grid of 0.4 Å and a time step of 0.5 fs are used.

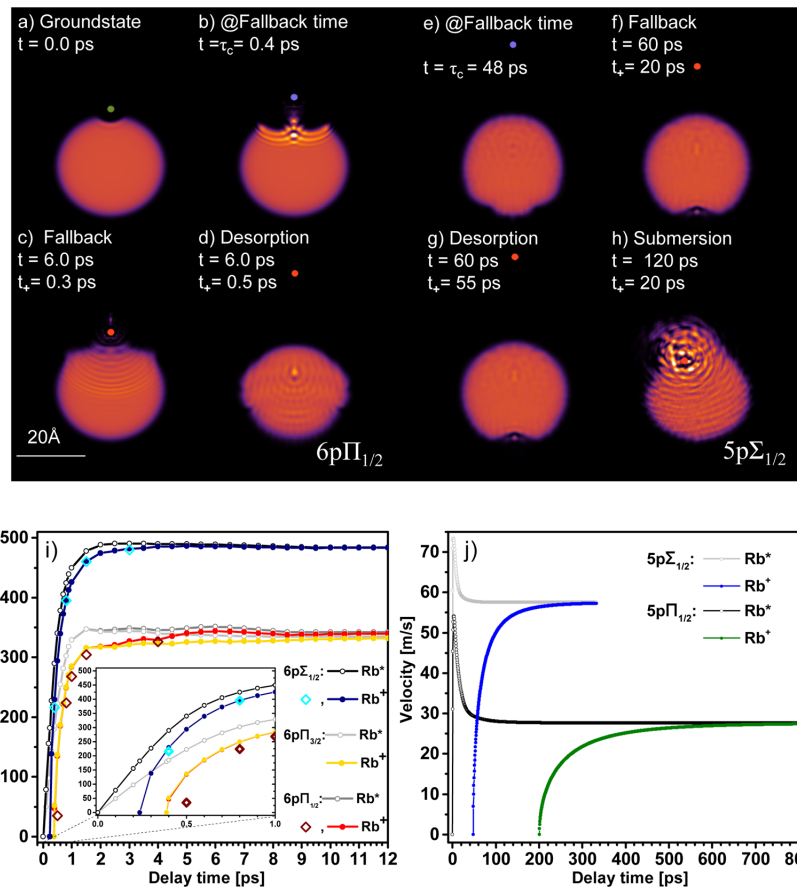


Figure 2. TDDFT-based 2D densities (a–d,e–h) and velocities (i,j) of Rb atoms attached to He_{1000} excited from equilibrium (a) to droplet perturbed 6p (left column) and 5p (right column) states. Configurations are shown for different propagation times t and ionization times t_+ : (b,e) neutral Rb at fall-back time $t = \tau_c$; (c,f) $t_+ < \tau_c$ fall-back of Rb^+ ion; (d,g) $t_+ > \tau_c$, desorption of Rb^+ ; (h) solvation of Rb^+ ; (i,j) evolution of Rb^* velocities with time t (gray open dots), and final velocities of Rb^+ (colored filled dots) as a function of t_+ .

For step 1, initial conditions are given by the structure of the neutral $\text{Rb}-\text{He}_{1000}$ complex in the ground state³² obtained using the $\text{Rb}-\text{He}$ potential of ref 37. For step 2 the initial conditions are given by the step 1 simulation at $t = t_+$. Carrying out the full simulations for step 2 is crucial for short and intermediate delays $t_+ \lesssim \tau_c$ as the droplet is still far from being relaxed when Rb^* is photoionized. At variance, we have checked that keeping the droplet density frozen as done in ref 14 is a good approximation for long delays $t_+ \gg \tau_c$. In Figure 2i the open diamonds show the difference between carrying out the full simulation and keeping the He density frozen at $t = \tau_c$ for $t_+ \gtrsim \tau_c$ (filled dots). For illustration, these simulations are provided as animations in the Supporting Information.

Figure 2a–d,e–h shows snapshots of the resulting 2D densities for different propagation times t and ionization times t_+ for the $6p\Pi_{1/2}$ (left column) and $5p\Sigma_{1/2}$ (right column) states. The ground-state dimple configuration is depicted in panel a. Figure 2b,e shows the configurations at the fall-back time τ_c . Panels c, d and g, h illustrate the desorption and fall-back processes. When ionization occurs before the fall-back time, $t_+ < \tau_c$ the ion turns around and submerges into the

droplet, where it becomes fully solvated (h). For $t_+ > \tau_c$, the ion keeps moving away from the droplet surface and fully desorbs (d, g). Panels i, j show the velocities of Rb^* (open symbols) and Rb^+ ions (filled symbols). The inset shows a close-up of the 6p dynamics at short propagation times.

For the 6p states, the Rb^* velocity features a steep rise that levels out after ~ 2 ps propagation time t (gray open dots). The final Rb^+ velocity is reduced compared with the Rb^* velocity at short delays $t_+ \lesssim 10$ ps (colored dots) due to the attraction of the Rb^+ ion toward the He droplet. For long delays these values converge as the Rb^+-He droplet attraction drops off at large distances. For the 5p case, the Rb^* velocity shows an overshoot at short delays relative to the asymptotic value. This is due to the transient Rb^*-He droplet interaction being weakly attractive at intermediate distance, which slows down the ejected Rb^* atom. It derives from the Rb^*-He potentials featuring an outer attractive region.

A compilation of the time constants for fall-back, τ_c , rise times of the ion speed, τ_v , as well as most probable Rb^+ final velocities, \hat{v}_f inferred from the experimental and theoretical data, is presented in Figure 3. The theory values of τ_v are

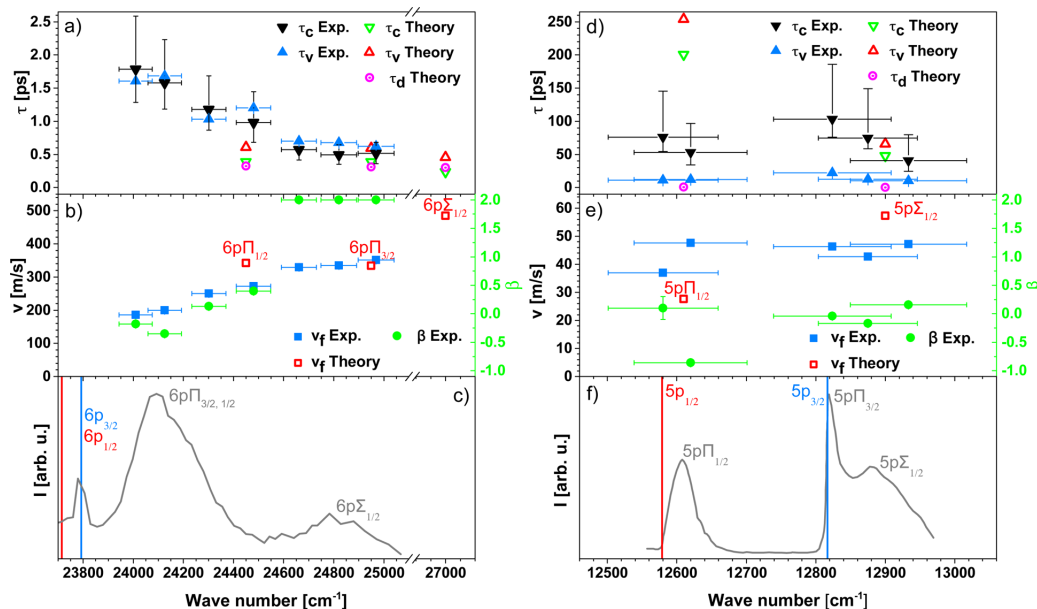


Figure 3. Experimental and theoretical fall-back time constants τ_c (a,d), velocity rise times τ_v (a,d), theoretical Rb* desorption times τ_d (a,d), Rb⁺ final most probable speeds v_f (b,e), and anisotropy parameters β (b,e) for different excitation wavenumbers corresponding to droplet perturbed Rb states 6p (left column) and 5p (right column). Panels c and f show fluorescence emission spectra as reference.^{25,38} Vertical lines indicate free atomic transitions.

determined by fitting the final ion velocities using the same model as for the experimental data. In addition, Figure 3a,d contains desorption times τ_d of the neutral Rb* atoms inferred from the simulation by fitting the same model as for ion velocities. Note that for the 5p $\Pi_{1/2}$ and 5p $\Sigma_{1/2}$ states we obtain values $\tau_d = 0.4$ and 0.2 ps, respectively, from the rising edges of the speed curves in Figure 2j. Figure 3b,e displays the anisotropy parameter β of the Rb⁺ angular distributions measured at long delay times. For reference we include the corresponding fluorescence excitation spectra taken from literature.^{25,38} Excitation wavenumbers for the theory values correspond to the peak positions of the simulated absorption spectra (not shown). Vertical error bars are connected to widths of the asymmetric fit function. Horizontal error bars reflect the spectral widths (FWHM) of the fs laser pulses.

The experimentally observed drastic difference between time scales for the 6p and 5p state dynamics is well-reproduced by the calculation. The general trend that fall-back times τ_c decrease and final velocities rise as a function of excitation wavenumber reflects the increasing repulsion acting between Rb* and the He droplet as the excitation energy is tuned up.^{9,13,24,26,32} Fall-back times τ_c and speed rise times τ_v exceed the desorption times τ_d of the neutral Rb* atom because the range of Rb⁺-He attractive interaction is larger than that of Rb*-He repulsion.¹⁴

Discrepancies are found for the asymptotic velocities of the 6p states that are smaller in the experiment than in the simulation by a factor of ~ 0.7 . Accordingly, experimental fall-back and speed rise times exceed the simulated values by a factor of 2 for the 6p $\Sigma_{1/2}$ and up to a factor of 4 for the 6p Π states. We attribute this mainly to the limited accuracy of the 6p Σ and 6p Π Rb*-He pair potentials³⁶ used in the simulation, causing a substantial blue shift of the simulated 6p \leftarrow 5s

absorption spectrum (not shown) with respect to the measured one.^{24,25}

For the 5p states the fall-back times being considerably larger than the speed rise times indicates that the desorption dynamics deviates to some extent from the impulsive model. In the limit of statistical desorption of Rb* atoms by an evaporation-like process, one would expect a continuously rising yield of free atoms and broad thermal distributions. Considering the slightly delayed, slow rise of the Rb⁺ yield (Figure 1f) and the peaked but broadened speed distributions that feature only small up-shifts at short delays (Figures 1d,e), we conclude that the dynamics of 5p excited states proceeds in a transition regime from impulsive dissociation to more complex, evaporation-like desorption. This conclusion is supported by the anisotropy parameter β (Figure 3e), whose sign correctly indicates the symmetry of the dissociating complex^{9,13,24} but whose absolute value is significantly reduced compared with that expected for impulsively dissociating complexes, in contrast with the 6p case (Figure 3b). Consequently, the quantitative agreement with the simulations, which do describe complex dynamical couplings within the superfluid model (Figure 2j) but do not contain statistical evaporation, is limited.

Aside from this, the experimentally observed higher final ion velocity and smaller fall-back time for the 5p $\Pi_{1/2}$ state compared with theory may be due to the measured signals being dominated by excitation of the blue edge of the 5p $\Pi_{1/2}$ feature. Considering the observed steep rise of fall-back time and drop of Rb⁺ velocity toward the red edge of the 5p $\Pi_{1/2}$ feature, our results agree with the previous finding that Rb* remains attached to the droplet surface upon narrow-band excitation at the red edge of the 5p $\Pi_{1/2}$ state.^{39,40}

Excitation of the $5p\Pi_{3/2}$ state leads to the formation of RbHe exciplexes because the Rb * -He pair interaction is strongly attractive in this state.^{15,16,38} While exciplex formation is reproduced by the simulation, the ejection of exciplexes off the He droplet surface is not. However, we find that nonradiative relaxation to the $5p\Pi_{1/2}$ state may supply enough kinetic energy to the Rb * atom to cause ejection. We therefore argue that when tuning the fs laser to the $5p\Pi_{3/2}$ peak, the experimentally observed Rb $^+$ signal is mainly due to spin relaxation to the $5p\Pi_{1/2}$ state.³⁸ Possibly the admixture of the nearby repulsive $5p\Sigma_{1/2}$ state also contributes. The relaxation dynamics will be further studied using time-resolved photoelectron spectroscopy. Let us mention that the RbHe $^+$ pump–probe transients (not shown) closely follow the ones of Rb $^+$ but significantly differ from those previously measured using a one-color NIR scheme.^{15,22} This raises some doubts as to the previous interpretation in terms of exciplex formation times and should be further investigated.

In conclusion, the observed dynamics of femtosecond pump–probe photoionization of Rb atoms attached to He nanodroplets is determined by the competition between the repulsive interaction of the droplet with the Rb atom in an excited state and the attractive interaction of the droplet with the Rb $^+$ cation, causing either desorption of Rb * off the droplet or submersion of the Rb $^+$ ion into the droplet interior, respectively. The resulting desorption dynamics proceeds impulsively within ~ 1 ps for the 6p excited states and in a transition regime between impulsive dissociation and statistical desorption within ~ 100 ps for the 5p states. This interplay between opposing trends (Rb * repulsion, Rb $^+$ attraction) is likely to be present in other types of clusters and condensed phase systems probed by time-resolved photoionization spectroscopy.

■ EXPERIMENTAL METHODS

The experimental setup has been previously described.^{14,32} In brief, He droplets with an average diameter of 10 nm are created by continuous supersonic expansion and doped by one Rb atom on average.^{14,32} The laser system generates amplified pulses of 100 fs duration at a repetition rate of 5 kHz with a tunable center wavelength in the near-infrared (NIR) region. Light in the visible range (VIS) is generated by frequency doubling. Pulses are split and separated in time in a Mach-Zehnder type interferometer. Droplet perturbed Rb 6p and 5p states are probed by one-color VIS and two-color NIR+VIS pump–probe schemes, respectively. NIR pulses are strongly attenuated to avoid excitations to higher lying states. Photoions are detected by a VMI spectrometer.^{24,28,32} For varying pump–probe delay steps, mass-selected ion VMIs are recorded and inverse-Abel transformed.³³ For each pump–probe scheme, a background contribution from ionization of effusive Rb is observed. In the measurement probing the Rb 6p states, additional background arises from single pulse ionization. To extract the pump–probe correlated dynamics, these contributions are subtracted from the signal.

■ ASSOCIATED CONTENT

Supporting Information

The following files are available free of charge. The Supporting Information is available free of charge on the ACS Publications website at DOI: [10.1021/acs.jpclett.6b02598](https://doi.org/10.1021/acs.jpclett.6b02598).

Desorption and fall-back dynamics of Rb atoms initially excited to the $5p\Pi_{1/2}$ state and ionized at $t_+ = 20$ ps. (AVI)

Desorption dynamics for $5p\Pi_{1/2}$ excitation and $t_+ = 55$ ps. (AVI)

Desorption and fall-back dynamics for $6p\Pi_{1/2}$ excitation $t_+ = 0.3$ ps. (AVI)

Desorption dynamics for $6p\Pi_{1/2}$ excitation and $t_+ = 0.5$ ps. (AVI)

■ AUTHOR INFORMATION

Corresponding Author

*E-mail: mudrich@physik.uni-freiburg.de.

ORCID

Marcel Mudrich: [0000-0003-4959-5220](https://orcid.org/0000-0003-4959-5220)

Notes

The authors declare no competing financial interest.

■ ACKNOWLEDGMENTS

Financial support for this work by the Deutsche Forschungsgemeinschaft (grant nos. MU 2347/6-1 and IRTG 2079), DGI, Spain (grant no. FIS2014-52285-C2-1-P), and HPC resources from CALMIP (Grant P1039) is gratefully acknowledged. M.B. thanks the Université Féderale Toulouse Midi-Pyrénées for financial support through the “Chaires d’Attractivité 2014” program IMDYNHE.

■ REFERENCES

- Toennies, J. P.; Vilesov, A. F. *Angew. Chem., Int. Ed.* **2004**, *43*, 2622.
- Stienkemeier, F.; Lehmann, K. *J. Phys. B: At., Mol. Opt. Phys.* **2006**, *39*, R127.
- Brauer, N. B.; Smolarek, S.; Loginov, E.; Mateo, D.; Hernando, A.; Pi, M.; Barranco, M.; Buma, W. J.; Drabbels, M. *Phys. Rev. Lett.* **2013**, *111*, 153002.
- Tiggesbäumker, J.; Stienkemeier, F. *Phys. Chem. Chem. Phys.* **2007**, *9*, 4748–4770.
- Müller, S.; Mudrich, M.; Stienkemeier, F. *J. Chem. Phys.* **2009**, *131*, 044319.
- Theisen, M.; Lackner, F.; Ernst, W. E. *Phys. Chem. Chem. Phys.* **2010**, *12*, 14861–14863.
- Zhang, X.; Drabbels, M. *J. Chem. Phys.* **2012**, *137*, 051102.
- Smolarek, S.; Brauer, N. B.; Buma, W. J.; Drabbels, M. *J. Am. Chem. Soc.* **2010**, *132*, 14086–14091.
- Hernando, A.; Barranco, M.; Pi, M.; Loginov, E.; Langlet, M.; Drabbels, M. *Phys. Chem. Chem. Phys.* **2012**, *14*, 3996–4010.
- Loginov, E.; Drabbels, M. *J. Chem. Phys.* **2012**, *136*, 154302.
- Mateo, D.; Hernando, A.; Barranco, M.; Loginov, E.; Drabbels, M.; Pi, M. *Phys. Chem. Chem. Phys.* **2013**, *15*, 18388–18400.
- Leal, A.; Mateo, D.; Hernando, A.; Pi, M.; Barranco, M.; Ponti, A.; Cargnoni, F.; Drabbels, M. *Phys. Rev. B: Condens. Matter Mater. Phys.* **2014**, *90*, 224518.
- Loginov, E.; Hernando, A.; Beswick, J. A.; Halberstadt, N.; Drabbels, M. *J. Phys. Chem. A* **2015**, *119*, 6033–6044.
- von Vangerow, J.; John, O.; Stienkemeier, F.; Mudrich, M. *J. Chem. Phys.* **2015**, *143*, 034302.
- Droppelmann, G.; Bünermann, O.; Schulz, C. P.; Stienkemeier, F. *Phys. Rev. Lett.* **2004**, *93*, 0233402.
- Reho, J.; Higgins, J.; Lehmann, K. K.; Scoles, G. *J. Chem. Phys.* **2000**, *113*, 9694–9701.
- Mudrich, M.; Doppelmann, G.; Claas, P.; Schulz, C.; Stienkemeier, F. *Phys. Rev. Lett.* **2008**, *100*, 023401.
- Mudrich, M.; Stienkemeier, F. *Int. Rev. Phys. Chem.* **2014**, *33*, 301–339.

- (19) Bruder, L.; Mudrich, M.; Stienkemeier, F. *Phys. Chem. Chem. Phys.* **2015**, *17*, 23877–23885.
- (20) Ziemkiewicz, M. P.; Neumark, D. M.; Gessner, O. *Int. Rev. Phys. Chem.* **2015**, *34*, 239.
- (21) Masson, A.; Poisson, L.; Gaveau, M.-A.; Soep, B.; Mestdagh, J.-M.; Mazet, V.; Spiegelman, F. *J. Chem. Phys.* **2010**, *133*, 054307.
- (22) Schulz, C. P.; Claas, P.; Stienkemeier, F. *Phys. Rev. Lett.* **2001**, *87*, 153401.
- (23) Giese, C.; Mullins, T.; Grüner, B.; Weidemüller, M.; Stienkemeier, F.; Mudrich, M. *J. Chem. Phys.* **2012**, *137*, 244307.
- (24) Fechner, L.; Grüner, B.; Sieg, A.; Callegari, C.; Ancilotto, F.; Stienkemeier, F.; Mudrich, M. *Phys. Chem. Chem. Phys.* **2012**, *14*, 3843.
- (25) Piffrader, A.; Allard, O.; Auböck, G.; Callegari, C.; Ernst, W.; Huber, R.; Ancilotto, F. *J. Chem. Phys.* **2010**, *133*, 164502.
- (26) Loginov, E.; Drabbels, M. *J. Phys. Chem. A* **2014**, *118*, 2738–2748.
- (27) Grüner, B.; Schlesinger, M.; Heister, P.; Strunz, W. T.; Stienkemeier, F.; Mudrich, M. *Phys. Chem. Chem. Phys.* **2011**, *13*, 6816–6826.
- (28) Eppink, A. T. J. B.; Parker, D. H. *Rev. Sci. Instrum.* **1997**, *68*, 3477.
- (29) Ancilotto, F.; DeToffol, G.; Toigo, F. *Phys. Rev. B: Condens. Matter Mater. Phys.* **1995**, *52*, 16125–16129.
- (30) Stienkemeier, F.; Higgins, J.; Ernst, W. E.; Scoles, G. *Phys. Rev. Lett.* **1995**, *74*, 3592–3595.
- (31) Bünermann, O.; Droppeleman, G.; Hernando, A.; Mayol, R.; Stienkemeier, F. *J. Phys. Chem. A* **2007**, *111*, 12684.
- (32) von Vangerow, J.; Sieg, A.; Stienkemeier, F.; Mudrich, M.; Leal, A.; Mateo, D.; Hernando, A.; Barranco, M.; Pi, M. *J. Phys. Chem. A* **2014**, *118*, 6604–6614.
- (33) Dick, B. *Phys. Chem. Chem. Phys.* **2014**, *16*, 570–580.
- (34) Mudholkar, G. S.; Hutson, A. D. *J. Stat. Plan. Inference* **2000**, *83*, 291–309.
- (35) Ancilotto, F.; Barranco, M.; Caupin, F.; Mayol, R.; Pi, M. *Phys. Rev. B: Condens. Matter Mater. Phys.* **2005**, *72*, 214522.
- (36) Pascale, J. *Phys. Rev. A: At., Mol., Opt. Phys.* **1983**, *28*, 632–644.
- (37) Patil, S. H. *J. Chem. Phys.* **1991**, *94*, 8089–8095.
- (38) Brühl, F. R.; Trasca, R. A.; Ernst, W. E. *J. Chem. Phys.* **2001**, *115*, 10220–10224.
- (39) Auböck, G.; Nagl, J.; Callegari, C.; Ernst, W. E. *Phys. Rev. Lett.* **2008**, *101*, 035301.
- (40) Theisen, M.; Lackner, F.; Ernst, W. E. *J. Phys. Chem. A* **2011**, *115*, 7005–7009.

4.2 Desorption dynamics of RbHe exciplexes

ARTICLE TYPE

Cite this: DOI: 10.1039/xxxxxxxxxx

Desorption dynamics of RbHe exciplexes off He nanodroplets induced by spin relaxation[†]

François Coppens,^a Johannes von Vangerow,^b Manuel Barranco,^{a,c} Nadine Halberstadt,^a Frank Stienkemeier,^b Martí Pi^c, and Marcel Mudrich,^d

Received Date

Accepted Date

DOI: 10.1039/xxxxxxxxxx

www.rsc.org/journalname

Doped He nanodroplets are ideal model systems to study the dynamics of elementary photophysical processes of heterogeneous nanosystems. Here we present a combined experimental and theoretical investigation of the formation of free RbHe exciplex molecules from laser-excited Rb-doped He nanodroplets. Upon excitation of a droplet-bound Rb atom to the $5p_{3/2}(\Pi_{3/2})$ -state, a stable RbHe exciplex forms within about 50 ps. Only due to $\Pi_{3/2} \rightarrow \Pi_{1/2}$ spin-relaxation does the RbHe exciplex detach from the He droplet surface within about 700 ps, given by the spin-relaxation time and the coupling of spin and translational degrees of freedom.

1 Introduction

Understanding the photochemistry of condensed phase systems and surfaces is essential in many research areas, such as atmospheric sciences¹ and photocatalysis². However, complex diabatic couplings of electronic and motional degrees of freedom of various subunits of the system often present a major challenge. Moreover, the heterogeneity of multi-component solid or liquid systems and experimental difficulties in precisely preparing the sample and reproducing measurements tend to make it hard to unravel specific elementary reactions. In this respect, He nanodroplets doped with single atoms or well-defined complexes are ideal model systems for studying photodynamical processes in the condensed phase, both experimentally and theoretically. Due to their ultralow temperature (0.37 K) and their quantum fluid nature, He nanodroplets have a homogeneous density distribution and dopant particles aggregate into cold clusters mostly inside the droplets^{3,4}. Only alkali metal atoms and small clusters are attached to He droplets in loosely bound dimple-like states at the droplet surface^{5–12}.

While He nanodroplets are extremely inert and weakly-perturbing matrices for spectroscopy of embedded atoms and molecules in their electronic ground state, a rich photochemical

dynamics is initiated upon electronic excitation or ionization^{13,14}, involving electronic relaxation^{15–18}, the ejection of the dopant out of the droplet^{19–26}, chemical reactions within the dopant complex^{27–29}, and even among the dopant and the surrounding He^{20,30–39}.

As a general trend, electronically excited dopant atoms and small molecules tend to be ejected out of He droplets either as bare particles or with a few He atoms attached to them^{15,40–42}. In particular, all atomic alkali species promptly desorb off the droplet surface, the only exceptions being Rb and Cs atoms in their lowest excited states^{43,44}. The dynamics of the desorption process has recently been studied at an increasing level of detail^{16,21,23,45}, including time-resolved experiments and simulations^{24,26}. The focus was on the competing processes of desorption of the dopant induced by laser excitation, and the dopant falling back into the He droplet upon photoionization. The latter occurred at short pump-probe delay times when the distance between the photoion and the droplet was short enough for ion-He attraction to be effective.

The purpose of this work is to extend our joint experimental and theoretical study of the photodynamics of Rb-doped He nanodroplets to RbHe exciplexes^{23,26}. The simultaneous effect of pair-wise Rb-He attraction and repulsion of Rb from the He droplet as a whole results in an intricate dynamics, and interpretations have remained somewhat ambiguous with respect to the exciplex formation mechanism and time scale, as well as the origin of free exciplexes detached from the He droplets^{16,26,30,33,34}. In particular the role of relaxation of internal degrees of freedom of the RbHe exciplex in the desorption process has not been explicitly addressed^{46,47}. Here, we discuss in detail the interplay of the RbHe formation dynamics, the RbHe desorption off the He droplet surface, and the fall-back of [RbHe]⁺ created by photo-

^a Laboratoire des Collisions, Agrégats, Réactivité, IRSAMC, UMR 5589, CNRS et Université Paul Sabatier-Toulouse 3, 118 route de Narbonne, F-31062 Toulouse Cedex 09, France

^b Physikalisches Institut, Universität Freiburg, Hermann-Herder-Str. 3, 79104 Freiburg, Germany

^c Institute of Nanoscience and Nanotechnology (IN2UB), Universitat de Barcelona, Diagonal 645, 08028 Barcelona, Spain

^d Department of Physics and Astronomy, Aarhus University, Ny Munkegade 120, Aarhus 8000 C, Denmark

* E-mail: mudrich@phys.au.dk

toionization in femtosecond pump-probe experiments^{24,26,31}. We find that electronic spin-relaxation is the main process driving the desorption of RbHe off the He droplet.

2 Methods

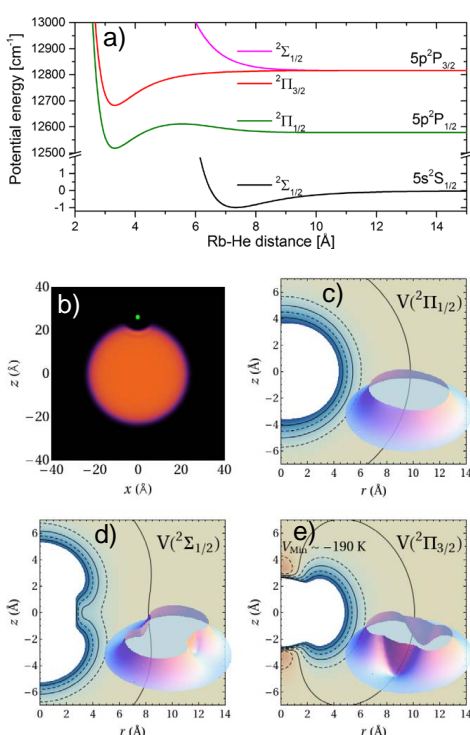


Fig. 1 (Color online) a) Rb-He pair potentials used in this work^{48,53}. The potentials correlating to the Rb excited 5p²P-state are split due to spin-orbit. b) Equilibrium dimple configuration of Rb in the groundstate (represented by a green dot). Panels c)-e) display the two-dimensional Rb-He potential surfaces corresponding to this configuration. Regions where the potentials are attractive (repulsive) are represented in brown (blue). The outermost equidensity line corresponds to zero potential. The 5p²Σ_{1/2} and 5p²Π_{1/2} potentials have a shallow attractive minimum of about 1 K depth at a distance of ~10 Å not represented in the figure.

2.1 Theoretical approach

During the last decade, the density functional theory (DFT) approach has emerged as an accurate and flexible tool to describe the statics and dynamics of doped helium droplets. The DFT activity carried out in this field has been summarized in two reviews^{7,14}. In the following we give the basic details how the method has been applied to the present problem, and refer the reader to Refs.^{14,22} for the details.

In this work, we describe the interaction of a Rb atom with a He droplet composed of $N = 1000$ He atoms. Due to its large mass,

Rb is treated as an external field in the statics, and as a classical particle in the dynamics. The impurity-droplet interaction is described in a pairwise approximation, and the groundstate of the droplet-impurity system is found by solving the Euler-Lagrange equation

$$\left\{ -\frac{\hbar^2}{2m} \nabla^2 + \frac{\delta \mathcal{E}_c}{\delta \rho} + V_X(|\mathbf{r} - \mathbf{r}_I|) \right\} \Psi_0(\mathbf{r}) = \mu \Psi_0(\mathbf{r}), \quad (1)$$

where $\Psi_0(\mathbf{r}) = \sqrt{\rho(\mathbf{r})}$ is the He effective wave function, with $\rho(\mathbf{r})$ being the atom density; μ is the He chemical potential, and V_X is the Rb-He pair potential⁴⁸. The correlation energy density functional \mathcal{E}_c has been taken from Ref.⁴⁹. The results presented in this work are obtained using the 4He-DFT BCN-TLS computing package⁵⁰. We work in cartesian coordinates using a space-step of 0.4 Å.

Once the droplet-equilibrium configuration shown in Fig. 1 b) is determined, the 5p \leftarrow 5s absorption spectrum is obtained using the DF sampling method⁵¹. To this end, the diatomic-in-molecule model is used for the droplet-Rb interaction in the excited 5p²P state⁵². The 5pΣ and 5pΠ Rb^{*}-He pair potentials, shown in Fig. 1 a), are taken from Refs.^{48,53}. The resulting simulated absorption dipole spectrum of the RbHe₁₀₀₀ complex, shown in Fig. 6 of Ref.¹⁴, is in good agreement with the experiment and previous calculations^{31,54}.

Figs. 1 c)-e) show the direction-dependent potentials (spin-orbit term included) which, within the diatomic-in-molecule approach, enter the dynamics simulations of Rb in the 5p²P-correlated states. In the course of the time evolution of the system, the He atoms have a natural tendency to adapt to these potential surfaces, either going away if the potential is mostly repulsive as in the Σ_{1/2}-state [Fig. 1 d)], or to evolve to a bound RbHe exciplex configurations in the Π_{3/2}-state [e)] featuring local minima at ($r = 0, z = \pm 3.5$ Å). In the Π_{1/2}-state near the D1-line transition [c)], one may also expect the formation of RbHe exciplexes given the potential minimum in the RbHe pair potential around 3.2 Å [Fig. 1 a)]. However, RbHe formation is hampered by a potential barrier which cannot be overcome at the low temperature of the He droplet^{31,55}.

2.2 Experimental setup

The setup used for the present experiments has been described previously^{23,24}. Briefly, a beam of He droplets with an average diameter of 10 nm is produced by continuously expanding pressurized He (50 bar) out of a cold nozzle (diameter 5 μm, temperature 17 K). The He droplets are doped with one Rb atom on average by pickup of Rb atoms inside a heated vapor cell (length 1 cm, temperature 85°C).

An amplified Ti:Sa laser system generates pulses of 100 fs duration at a repetition rate of 5 kHz. The center wavelength is tunable in the near infrared (NIR) region. The FWHM of the spectral laser profile is 140 cm⁻¹. Light in the visible range (VIS) is generated by frequency doubling. The pulses are split and separated in time in a Mach-Zehnder type interferometer. The droplet perturbed Rb 5p states are probed by a two-color NIR+VIS pump-probe resonant photoionization scheme. The NIR

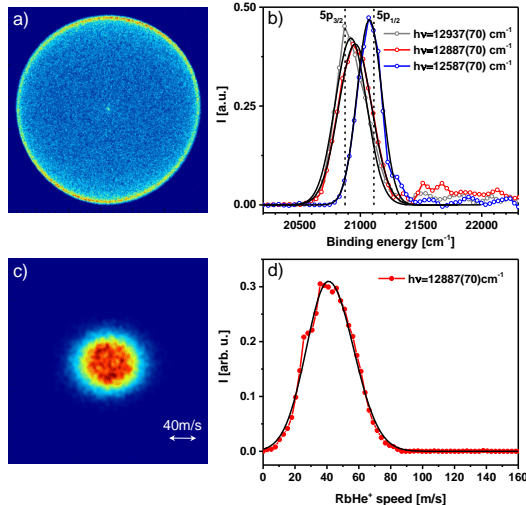


Fig. 2 Raw velocity-map images of photoelectrons a) and of RbHe⁺ photoions c) recorded at $\lambda = 776$ nm (12887 cm^{-1}) for a long pump-probe delay time of 2 ns. b) Electron binding energies inferred from the image in a) and from images recorded at $\lambda = 773$ nm (12937 cm^{-1}) and at $\lambda = 794$ nm (12587 cm^{-1}). d) RbHe⁺ photoion speed distribution inferred from c).

pulses are strongly attenuated to avoid the excitation of higher lying states by multi-photon processes. Polarizations of the two laser pulses are parallel to one another and parallel to the detector surface.

Photoions and photoelectrons are detected by a velocity-map imaging (VMI) spectrometer operated in centroid detection mode^{16,23,56,57}. Mass-selected ion VMIs are recorded for varying pump-probe delay times and are inverse Abel-transformed^{58,59}. Both Rb⁺ ion images and electron images contain background contributions stemming from resonant ionization of free Rb atoms effusing out of the doping cell. In order to efficiently subtract these contributions, background images are recorded at each pump-probe delay using a chopper running at a frequency of 15 Hz. Aquired background and signal+background images are inverse Abel transformed. The resulting spectra are normalized to the numer of counts and subtracted from each other exploiting the additivity of the inverse Abel transformation⁶⁰.

3 Time-resolved imaging spectroscopy

Typical experimental total electron and RbHe⁺ ion VMIs recorded at a center wavelength of the pump laser pulse $\lambda = 776$ nm and a pump-probe delay of 2 ns are shown in Fig. 2 a) and c), respectively. In these VMIs, the laser polarization is oriented along the y-axis. The corresponding electron energy distribution and ion speed distribution inferred from these images are presented in Fig. 2 b) and d), respectively. In addition, Fig. 2 b) contains photoelectron spectra measured at $\lambda = 773$ and 794 nm. Note that the photoelectron spectra in Fig. 2 b) are rescaled in terms of electron

binding energies $E_b = h\nu_2 - T_e$, where $h\nu_2 = 2hc/\lambda$ denotes the photon energy of the ionizing laser pulse and T_e is the measured electron kinetic energy. The dashed vertical lines represent E_b of the free atomic 5p_{1/2} and 5p_{3/2}-states.

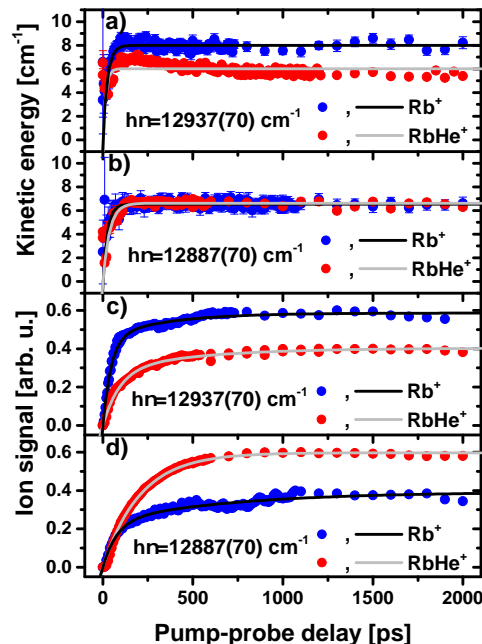


Fig. 3 Rb⁺ and RbHe⁺ ion kinetic energies [a) and b)] and signal yields [c) and d)] recorded at laser wavelengths $\lambda = 773$ nm [12937 cm^{-1} , a) and c)] and $\lambda = 776$ nm [12887 cm^{-1} , b) and d)].

3.1 Photoion imaging

The RbHe⁺ ion distribution [Fig. 2 c)] is a round spot with a flat intensity distribution and a slight elongation in x-direction (perpendicular to the laser polarization). The corresponding speed distribution is broad and nearly symmetric. The red line depicts a skewed Gaussian distribution fitted to the data⁶¹. This fit is applied repeatedly to each speed distribution measured at various pump-probe delays in order to trace the evolution of the most probable kinetic energy, see Fig. 3 a) and b). The yields of ions, shown in Fig. 3 c) and d), are obtained by summing over ion counts contained in each image. Blue and red symbols show the results for Rb⁺ and RbHe⁺ ions, respectively. Both kinetic energies and ion yields monotonously increase within 100-500 ps, with a slight overshoot at $\lambda = 773$ nm [Fig. 3 a)]. This dynamics results from the competing processes of desorption of the excited neutral Rb and RbHe species, and the falling back of the Rb⁺ and RbHe⁺ photoions into the He droplet due to attractive Rb⁺-He interactions, as discussed in Refs.^{24,26}. By comparing the experimental data with TD-DFT dynamics simulations, we concluded that the 5p-correlated states of Rb and RbHe desorb

off He droplets not purely impulsively, but in a more complex evaporation-like process²⁶. The overshoot of speeds in Fig. 3 a) is likely due to weak long-range attractive forces acting between the desorbing Rb and RbHe and the He droplet surface, which slightly slow down the relative motion in the later stage of desorption.

The data in Fig. 3 a) are measured at $\lambda = 773$ nm (12937 cm^{-1}), which corresponds to the excitation of the RbHe complex into the $5p\Sigma_{1/2}$ -state, with some contribution of the $5p\Pi_{3/2}$ -state due to overlapping absorption bands and due to the broad spectral width of the laser and ^{6,31,62}. The $5p\Sigma_{1/2}$ -state is the most repulsive one out of the three states studied here. Accordingly, the asymptotic most probable speed of Rb^+ reached at long delays is comparatively high, $\hat{v} = 85\text{ m/s}$, corresponding to a kinetic energy of 8 cm^{-1} , whereas for RbHe^+ we find $\hat{v} = 40\text{ m/s}$ (5.8 cm^{-1}). Since the diatomic $5p\Sigma_{1/2}$ RbHe potential is purely repulsive [Fig. 1 a)], this component of the excited population yields neat desorbed Rb atoms. Accordingly, the yield of detected Rb^+ ions exceeds that of RbHe^+ ions by about a factor 1.5.

At $\lambda = 776$ nm (12887 cm^{-1}), a higher contribution of the $5p\Pi_{3/2}$ -state is excited, which efficiently forms RbHe exciplexes³¹. Thus, the yield of RbHe^+ ions is higher than that of Rb^+ by a factor 1.5. The Rb^+ and RbHe^+ asymptotic most probable speed is 42 m/s (6.3 cm^{-1}), close to that of RbHe^+ at $\lambda = 773$ nm. At $\lambda = 794$ nm (12595 cm^{-1} , $5p\Pi_{1/2}$ -state of the Rb-He droplet complex, not shown), no RbHe^+ ions are detected. Therefore we have recorded only Rb^+ ion images at that wavelength²⁶. Here, the Rb^+ asymptotic most probable speed is lowest, 38 m/s (5.1 cm^{-1}), because dopant-He repulsion is weakest.

The transient kinetic energies measured at all laser wavelengths rise within a delay time of about 500 ps. The characteristic energy rise time (to half value), τ_d , and the asymptotic ion kinetic energy E' , are determined by fitting the data with an exponential function

$$E'(t) = E' \cdot (1 - \exp[-\ln 2 \cdot t / \tau_d]). \quad (2)$$

The resulting fit parameters are summarized in table 1.

The ion yields increase with pump-probe delay slightly more slowly than the ion kinetic energies, where the Rb^+ ion signal rises faster than the RbHe^+ ion signal at short delays. The initial fast rise of the Rb^+ ion yield flattens out at delays around 100 ps and continues to rise slightly up to about 2 ns. The RbHe^+ ion yields show a similar initial fast rise followed by a more pronounced slow increase that levels off somewhat earlier. For fitting the Rb^+ and RbHe^+ ion yield data we use a biexponential function,

$$I(t) = A \cdot (1 - \exp[-\ln 2 \cdot t / \tau]) + A^* \cdot (1 - \exp[-\ln 2 \cdot t / \tau^*]), \quad (3)$$

where (A, τ) and (A^*, τ^*) parametrize the fast and the slow signal rise, respectively.

While neither the Rb^+ and RbHe^+ asymptotic energies E' , nor the energy rise times τ_d depend much on λ , the rise times of ion yields of RbHe^+ , τ , clearly decrease monotonically with decreasing λ (increasing photon energy) by a factor 6, ranging from

186 ps at $\lambda = 780$ nm to 33 ps at $\lambda = 773$ nm.

The trend that the dynamics proceeds faster with decreasing λ (increasing photon energy) is due to the increasingly repulsive dopant-He interaction and agrees with our previous findings^{24,26}. However, the observation that the ion yields rise more slowly than the ion kinetic energies cannot be understood with the concept of impulsive desorption and fall-back. In that model, ion kinetic energies should be affected by ion-He attraction up to long delay times exceeding the fall-back time. Note that in previous experiments on the Rb 5p-state, where desorption proceeded impulsively, ion energies indeed increased more slowly than ion yields²⁶. Therefore we take our current finding ($\tau, \tau^* > \tau_d$) as a further indication for a non-impulsive, evaporation-like desorption dynamics.

Furthermore, from our analysis of the VMIs we obtain information about the anisotropy of the ion angular distribution, characterized by the parameter β ¹⁶. For long delay times we find $\beta = -0.36(1)$ when exciting mainly the $\Pi_{3/2}$ -state at $\lambda = 776$ nm. At $\lambda = 773$ nm (mainly $\Sigma_{1/2}$ -excitation), the anisotropy becomes slightly positive, $\beta = 0.13(1)$. The corresponding values for the Rb^+ ion distributions are $\beta = -0.16(1)$ and $\beta = 0.17(1)$, respectively. While the signs of the β -values are in agreement with the symmetries of coupled states (ideal perpendicular $\Sigma \rightarrow \Pi$ -transition in a diatomic implies $\beta = -1$, parallel $\Sigma \rightarrow \Sigma$ -transition implies $\beta = 2$), the absolute values are much less. On the one hand, this is due to the mixture of excited $\Sigma_{1/2}$ and $\Pi_{3/2}$ -states. On the other hand, the desorption process is significantly more complex than direct dissociation of a diatomic molecule. We recall that the β -values came much closer to the ideal values in the case of excitation of Rb to the high-lying 6p-correlated states, where desorption proceeded more impulsively^{16,23,26}. The larger absolute value of β measured at $\lambda = 776$ nm for $[\text{RbHe}]^+$ likely reflects the fact that RbHe exciplexes are formed only from the $\Pi_{3/2}$ -part of the excited state.

We mention that in earlier pump-probe experiments, significantly differing Rb^+ and $[\text{RbHe}]^+$ ion yield curves were measured³³. However, in those experiments, near-infrared light emitted directly from a mode-locked titanium:sapphire laser was used at a pulse repetition rate of 80 MHz. Therefore, a large fraction of the ion signals actually stemmed from Rb and RbHe that were desorbed off the droplets by preceding pulse pairs. Thus, the observed pump-probe transients may have reflected the internal dynamics of free RbHe instead of the dynamics of the Rb-He droplet interaction. Besides, near-resonant two-photon excitation of higher lying states correlating to the Rb 5d-level were probably involved in the observed dynamics. This raises some doubts as to the conclusions of those previous experiments in terms of exciplex formation times^{26,33}. Further studies are needed to clarify this issue.

From the overall resemblance of the RbHe^+ and Rb^+ kinetic energy curves and ion yields in the present study one is tempted to conclude that RbHe exciplex formation is fast and desorption of RbHe off the He droplet surface proceeds essentially in the same way as for neat Rb atoms. However, the more pronounced biexponential rise of $[\text{RbHe}]^+$ ion yields, as well as complementary delay-dependent photoelectron measurements in combina-

λ [nm]	State	Ion	E^I [1/cm]	τ_d [ps]	A	τ [ps]	A^*	τ^* [ps]	β
773	$\Sigma_{1/2}/\Pi_{3/2}$	Rb ⁺	8.0(1)	17(1)	0.45(2)	32(1)	0.14(2)	234(33)	*** 0.13(1)
		RbHe ⁺	6.0(1)	10(2)	0.17(2)	41(6)	0.22(2)	178(17)	
776	$\Pi_{3/2}/\Sigma_{1/2}$	Rb ⁺	6.5(3)	17(1)	0.24(2)	53(5)	0.16(2)	490(104)	*** -0.39(1)
		RbHe ⁺	6.6(3)	26(1)	0.60(1)	143(2)	~ 0	-	

Table 1 Time constants and energies inferred from the pump-probe measurements of mainly the $5p\Sigma_{1/2}$ and $5p\Pi_{3/2}$ -states, obtained from fits with equations (2 and 3), see Fig. 3.

tion with simulations presented in the following sections will show that the desorption dynamics of RbHe exciplexes is more complex than that of Rb atoms.

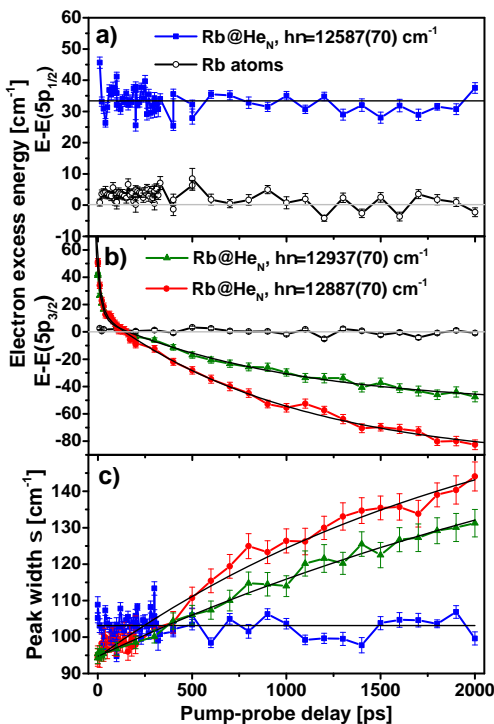


Fig. 4 Photoelectron energies as a function of pump-probe delay (filled circles) recorded at laser wavelengths $\lambda = 794$ nm ($5p\Pi_{1/2}$) (a), and $\lambda = 773$ nm ($5p\Sigma_{1/2}$) and $\lambda = 776$ nm ($5p\Pi_{3/2}$) (b). Open circles indicate the electron energies measured for atomic Rb background signal.

3.2 Photoelectron imaging

The photoelectron spectra recorded at the three characteristic laser wavelengths λ [Fig. 2 b)] exhibit pronounced peaks around the Rb $5p_{1/2}$ and $5p_{3/2}$ atomic binding energies, $E_{5p1/2}$ and $E_{5p3/2}$, respectively. Both the peak position and the peak width significantly vary with λ , as inferred from fits to the data with a Gaussian function, depicted as smooth lines. The resulting peak

positions relative to $E_{5p1/2}$ and $E_{5p3/2}$ are plotted in Fig. 4 a), b), respectively. Fig. 4 c) shows the peak widths σ . For reference, the open symbols represent the peak positions measured for the Rb atomic background. The scatter of data points around the literature value (grey horizontal line) indicates the level of precision of our measurements.

The excess energies for the $5p\Sigma_{1/2}$ and $5p\Pi_{3/2}$ -states, $E_b - E_{5p1/2,5p3/2}$ [Fig. 4 b)] exhibit a fast decay (E_+^e, τ_+^e) above and a slow decay (E_-^e, τ_-^e) below $E_{5p3/2}$ (horizontal line at $y = 0$). Therefore, these data are fitted with a biexponential decay function

$$E^e(t) = E_+^e \cdot \exp(-\ln 2 \cdot t / \tau_+^e) + E_-^e \cdot \exp(-\ln 2 \cdot t / \tau_-^e) + E_\infty^e. \quad (4)$$

Here, E_∞^e denotes the asymptotic energy value at long delay times. When exciting the $5p\Pi_{1/2}$ -state at $\lambda = 794$ nm, the transient droplet correlated peak position remains constant within the experimental scatter. Therefore, merely the mean value E_+^e is determined. The resulting energies and time constants are summarized in table 2. The increasing peak widths in the cases of $\lambda = 773$ and 776 nm are fitted by the simple exponential function given by Eq. 2.

The fact that the droplet-related photoelectron energy E_+^e for the $\Pi_{1/2}$ -state is constant but shifted with respect to the atomic value indicates that most of the Rb atoms remain attached to the droplet surface upon electronic excitation, in accordance with previous studies^{43,63}. Thus, the slowly rising Rb⁺-ion signal measured at that wavelength, indicative for excited Rb^{*} desorption, reflects only a small fraction of Rb^{*} atoms, most of which actually remain bound to the droplets. The measured up-shift of electron energy of $E_+^e = 33(2)$ cm⁻¹ is attributed to a lowering of the ionization threshold induced by the He environment. This value is in reasonable agreement with previous measurements, where the ionization threshold was found to be lowered by 50(10) cm⁻¹ at comparable conditions⁶³.

The similar dynamics of electron energies and ion yields for the $\Sigma_{1/2}$ and $\Pi_{3/2}$ -states – a biexponential evolution with a fast component (tens of ps) and a slow component (hundreds of ps) – we take as a confirmation that two distinct relaxation processes occur simultaneously. The fast process – prompt desorption of Rb^{*} off the He droplet – is associated mainly with the $\Sigma_{1/2}$ -component of the excited state, whereas the $\Pi_{3/2}$ -component undergoes slow relaxation. The latter will be discussed in the following sections. Deviations of the time constants τ vs. τ_+^e , and τ^* vs. τ_-^e are mainly due to the different nature of the observables. Both ion yields and

λ [nm]	State	E_+^e [1/cm]	τ_+^e [ps]	E_-^e [1/cm]	τ_-^e [ps]	E_∞^e [1/cm]
773	$\Sigma_{1/2}/\Pi_{3/2}$	32(2)	15(2)	63(4)	683(130)	-53(5)
776	$\Pi_{3/2}/\Sigma_{1/2}$	36(2)	13(2)	110(4)	709(70)	-96(5)
794	$\Pi_{1/2}$	33(2)	-	-	-	-

Table 2 Time constants and energies inferred from the transient photoelectron energies (Fig. 4).

speeds are affected by the dynamics occurring after the probe-ionization, whereas electron spectra probe the spatial distribution (and electronic state) at the moment of ionization. In particular, ion signals provide information only about that fraction of ions that are eventually detached from the He droplets, whereas electron signals are measured for all photoionization events, including those where the ion falls back into the droplet; in this respect the electron spectra are the better probes of the full Rb^{*} dynamics, with the restriction that we cannot distinguish between the final products (Rb^{*}, [RbHe]^{*}, [Rb^{*}He_N]). For this, electron-ion coincidence detection would have to be applied, as e. g. in Ref.⁶⁴.

We mention that at $\lambda = 776$ nm ($\Pi_{3/2}$ -state), an extended low intensity distribution is present in the spectrum [Fig. 4 b)] at higher electron binding energies $\geq 21,500$ cm⁻¹ (lower electron kinetic energies). We attribute this component to elastic scattering of photoelectrons with He atoms as they propagate through the He droplet. Low-energy features in photoelectron spectra due to electron-He scattering have been observed previously, in particular when using one-photon ionization^{64–67}. The fact that this feature is most pronounced for the $\Pi_{3/2}$ -excitation may be related to the more abundant formation of RbHe exciplexes which enhances the electron-He scattering probability.

4 TD-DFT dynamics simulation

Time-dependent density functional theory (TD-DFT) simulations are carried out as thoroughly described in Refs.^{14,22}. The step width in time and space is 0.5 fs and 0.4 Å, respectively. Starting with the Rb-droplet equilibrium configuration, the dynamics is initiated by a “vertical DFT transition” into the excited state. This is realized by suddenly switching from the potential energy surface of the Rb-He droplet groundstate to that of the Rb^{*}-He excited state. The subsequent evolution of the system can be followed in real-time, as illustrated by the series of snapshots of the He density distribution (red area) and the position of the Rb atom (green and magenta dots) in Fig. 5. Here, excitation of the 5p $\Pi_{3/2}$ -state at $t = 0$ is followed by relaxation to the 5p $\Pi_{1/2}$ -state at $t = 60$ ps.

4.1 Direct ejection of bare Rb atoms from the $^2\Sigma_{1/2}$ and $^2\Pi_{1/2}$ -states

From these data we now infer the relevant quantities to compare with the experimental results, such as the kinetic energy of the Rb atom relative to the droplet, the occurrence of He density attached to Rb which we identify with the formation of an exciplex, and the transient interaction energy of the neutral and ionized Rb atom with the surrounding He. The latter is related to the kinetic energy of a photoelectron created in a time-delayed photoionization

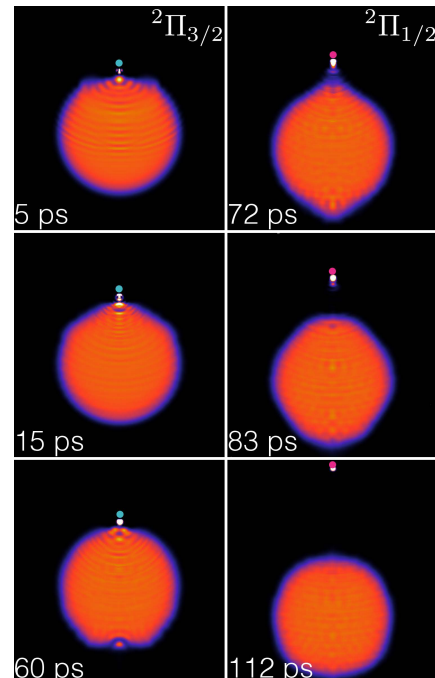


Fig. 5 Snapshots of the He density during the evolution of the Rb^{*}He₁₀₀₀ complex for $\eta = 15\%$, $\tau = 60$ ps. The green dot represents the Rb^{*} atom excited into the 5p $\Pi_{3/2}$ -state, and the magenta dot is the Rb^{*} atom after suddenly relaxing to the 5p $\Pi_{1/2}$ -state.

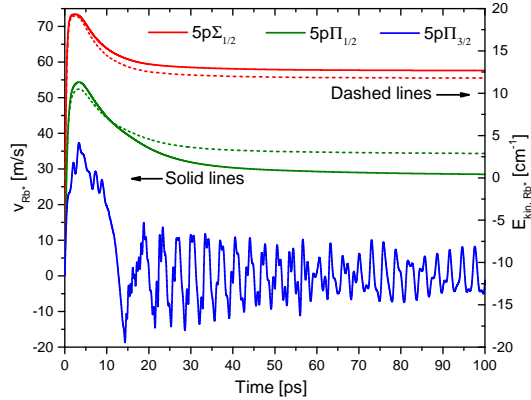


Fig. 6 (Color online) Velocity (dashed lines, right scale) and kinetic energy (solid lines, left scale) of the Rb atom excited to the 5p-state as a function of time. The kinetic energy of the $5p\Pi_{3/2}$ -state is not given as this state remains bound to the droplet.

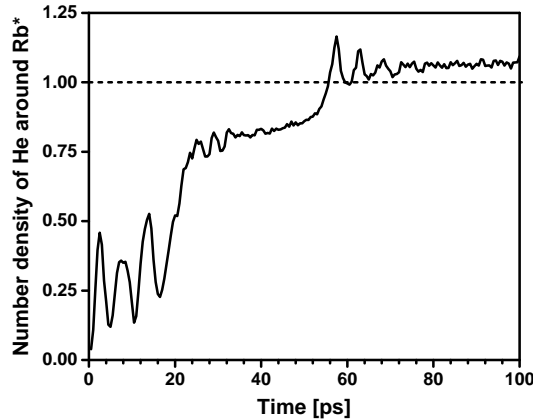


Fig. 7 (Color online) Simulated time evolution of the integrated He density within an inclusion volume of radius $r_{\text{incl}} = 5.7 \text{ \AA}$ around the Rb atom excited to the $5p\Pi_{3/2}$ -state.

process.

Fig. 6 collects our results for the dynamics of the Rb atom excited to the droplet-perturbed states correlating to the atomic 5p-state. For the $\Sigma_{1/2}$ and $\Pi_{1/2}$ -states, the velocities (dashed lines) and kinetic energy curves (solid lines) feature rapid increase to reach a maximum at time $t = 2\text{-}5 \text{ ps}$ after excitation, followed by a drop due to long-range attractive forces acting on the desorbing Rb^{*} atom. The asymptotic values are reached for $t > 50 \text{ ps}$. When exciting the $\Pi_{3/2}$ -state, the Rb^{*}-velocity features a damped oscillation around zero indicating that the Rb^{*} atom remains bound to the He droplet surface.

The following conclusions can be drawn from these results: (i) Rb excited to the $5p\Sigma_{1/2}$ -state detaches from the droplet reaching an asymptotic kinetic energy of 12 cm^{-1} ***. This value slightly deviates from the experimental one (8.0 cm^{-1}) due to contributions of $\Pi_{3/2}$ -excitation to the experimental signal. Despite of the shallow local minima in the corresponding Rb-He droplet potential surface [1 c], no binding of He density to the departing Rb^{*} atom occurs. This finding is in accordance with experiments^{16,31,33}, where mostly free Rb atoms were detected following excitation at wavelengths $\lambda < 774 \text{ nm}$.

(ii) Rb excited to the $5p\Pi_{1/2}$ -state also detaches from the He droplet, but the asymptotic kinetic energy is much lower, 2.8 cm^{-1} . This value again slightly deviates from the experimental one (5.1 cm^{-1}), but the trend that desorption of the less repulsive $\Pi_{1/2}$ -state yields a lower energy than for the $\Sigma_{1/2}$ -state is well reproduced. The potential well at short distance $\sim 3 \text{ \AA}$ would in principle support a stable RbHe exciplex. However, at the low temperature of the He droplet, exciplex formation is hindered by a potential barrier located at $\sim 5 \text{ \AA}$, between the well and the range where the $5p\Pi_{1/2}$ -state is populated by excitation from the $5s\Sigma_{1/2}$ -groundstate (7 \AA)^{30,31,55}.

We recall that in previous experiments using narrow-band ex-

citation of the low energy edge of the $\Pi_{1/2}$ -resonance it was observed that Rb and Cs dopants remained attached to the He droplet surface⁴³. However, our simulations correspond to the excitation at the peak of the resonance, where free Rb atoms are also observed in the experiment. Thus, our simulations are not in conflict with the experimental findings. Note that Quantum Monte Carlo (QMC) calculations carried out for this state⁶⁸ yielded a weakly bound Rb^{*} in a shallow dimple. Had we carried out a static DFT relaxation, we would also have found a bound structure, due to the shallow minimum on the Rb-He droplet potential surface. However, in the dynamical TD-DFT simulation this minimum is too shallow to retain the departing Rb^{*} atom.

(iii) In our simulation we find that Rb excited to the $5p\Pi_{3/2}$ -state remains bound to the He droplet surface where it forms a RbHe exciplex. Fig. 1 shows two deep barrierless potential wells at a Rb-He distance of about 3 \AA . In the course of the dynamics, the Rb^{*} atom is drawn to the well close to the droplet surface, develops a RbHe exciplex that remains bound to it, and oscillates around an equilibrium position of 3 \AA above the static equilibrium position at the dimple as shown in Fig. 6. This result is in full agreement with static QMC calculations by Leino et al.⁴⁶. However, contrary to the conjecture of that paper, in our simulations we do not find that damping of the vibrational motion of the RbHe exciplex structure leads to its desorption from the He droplet.

The dynamics of the exciplex formation process can be quantitatively represented by integrating over the He density within a spherical inclusion volume with radius r_{incl} around Rb^{*}. The result is shown in Fig. 7. Thus, for $r_{\text{incl}} = 5.7 \text{ \AA}$, which contains the entire localized He density at the Rb^{*} atom without including He density of the remaining droplet, we find a rise to 75 % of the final value at $t = 20 \text{ ps}$. For $t > 60 \text{ ps}$ the He number density stabilizes close to 1, indicating the full evolution of a RbHe exciplex containing 1 He atom. This result is in good agreement with

η (%)	v_∞ (m/s)	Kin. energy (cm ⁻¹)
5	bound	–
10	13.4	0.64
12.5	43.0	6.6
15	62.4	13.9
20	80.4	23.0

Table 3 Asymptotic velocity of the ejected Rb^{*}-He exciplex for various values of the fraction η of the 5p $\Pi_{3/2,1/2}$ -energy spacing of 165 cm⁻¹ which is converted into kinetic energy of Rb^{*} by relaxation from the 5p $\Pi_{3/2}$ into the 5p $\Pi_{1/2}$ -state. The calculations are carried out at a delay time $\tau = 60$ ps between photo-excitation and non-radiative de-excitation of the Rb^{*} atom.

the previous fs pump-probe measurements, where an increasing RbHe⁺ signal was observed that reached its maximum at a delay time of about 20 ps^{33,34}.

The finding that the RbHe exciplex remains attached to the He droplet is in apparent contradiction to experiments where the ejection of free Rb and RbHe was clearly observed^{16,31,33}. Therefore, an additional mechanism must be active that induces the desorption of the RbHe molecule off the He droplet surface.

4.2 RbHe exciplex formation around the 5p² $\Pi_{1/2}$ -state: non-radiative relaxation from the 5p² $\Pi_{3/2}$ -state

In the gas phase, a RbHe exciplex can be formed in the 5p $\Pi_{1/2}$ -state if enough kinetic energy is provided by collisions such that the Rb^{*} can overcome the potential barrier⁵⁵. Alternatively, collisions of a RbHe formed in the 5p $\Pi_{3/2}$ exciplex with another atom or complex might induce relaxation into a RbHe electronic state correlating to the Rb 5p $1/2$ -state. In this case the barrier is circumvented by the relaxation process, as the potential wells for the two states $\Pi_{3/2}$ and $\Pi_{1/2}$ are at similar Rb-He distances. In the condensed (droplet) phase at 0.4 K temperature, none of these mechanisms are active to explain the formation of RbHe 5p² $\Pi_{1/2}$ exciplexes and their potential ejection.

However, Fig. 1 a) indicates another possible mechanism: Non-radiative de-excitation from the 5p $\Pi_{3/2}$ to the 5p $\Pi_{1/2}$ -state accompanied by transfer of energy into the relative motion of the Rb^{*} atom away from the He droplet. Notice from the figure that the minimum of the 5p $\Pi_{3/2}$ -potential is at ~ 12683 cm⁻¹, and that of the 5p $\Pi_{1/2}$ -potential is at ~ 12518 cm⁻¹; the value of this potential at the barrier is 12611 cm⁻¹. Thus, non-radiative de-excitation of the Rb^{*} atom may add to its original kinetic energy a fraction of this 165 cm⁻¹ difference energy. Consequently, the RbHe exciplex will be ejected in the 5p $\Pi_{1/2}$ -state, and not in the 5p $\Pi_{3/2}$ -state that was originally photo-excited. Non-radiative electronic relaxation induced by the He droplet has been observed for a number of metal atoms^{15–18,38,41,69}. In particular, previous measurements of the dispersed fluorescence upon excitation of Rb into the 5p $\Pi_{3/2}$ -state of the Rb-He droplet complex have evidenced large populations of free Rb^{*} atoms in the 5p $\Pi_{1/2}$ -state³¹. Efficient spin-relaxation of 5p $\Pi_{3/2}$ -excited Rb atoms can be rationalized by the large cross section for mixing of fine structure states in collisions of alkali metal atoms with He⁷⁰. For low-temperature Rb-He collisions, the fine structure relaxation rate

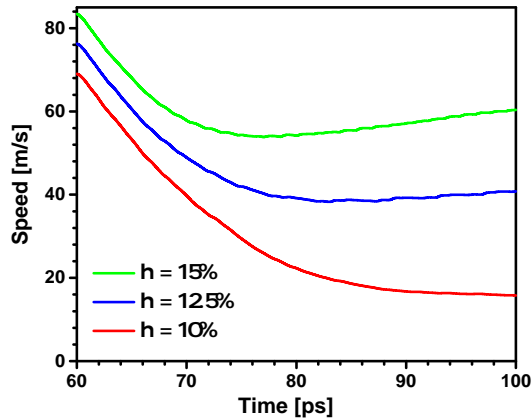


Fig. 8 (Color online) Velocity of the Rb^{*} atom with attached He density as a function of time after 5p $\Pi_{3/2} \rightarrow 5p\Gamma_{1/2}$ relaxation at $\tau = 60$ ps for various values of the energy conversion factor η .

was found to be enhanced by the transient formation of a RbHe exciplex by orders of magnitude compared to binary Rb-He collisions⁵⁵.

Here we explore this scenario within TDDFT. Starting from Rb^{*} in the 5p $\Pi_{3/2}$ -state, we induce a “vertical DFT transition” by suddenly switching potential energy surfaces from 5p $\Pi_{3/2}$ to 5p $\Pi_{1/2}$, imparting to the Rb^{*} a kinetic energy corresponding to a fraction η of the available non-radiative de-excitation energy. The time τ elapsing between the vertical excitation and de-excitation has to be chosen as well; this time influences the degree of RbHe 5p $\Pi_{3/2}$ exciplex formation which, as we have seen, may require some tens of ps. The actual value of these inputs cannot be determined by the model itself.

In the following, we present results obtained from simulations using as input parameters the delay before relaxation $\tau = 60$ ps, and several values of η . As shown in Fig. 6 (see also the bottom left panel of Fig. 5), this –arbitrary– time is sufficient to allow for a full development of the 5p $\Pi_{3/2}$ RbHe exciplex and to bring it to a rather stationary configuration.

Fig. 5 (right column) shows snapshots of the evolution following the 5s $\Sigma_{1/2} \rightarrow 5p\Gamma_{3/2} \rightarrow 5p\Gamma_{1/2}$ process for $\eta = 15\%$, $\tau = 60$ ps. Thus, upon sudden relaxation to the 5p $\Gamma_{1/2}$ -state, the Rb^{*}-He structure promptly detaches from the remaining He droplet. The velocity of the Rb^{*} atom as a function of time is depicted in Fig. 8 for this and other values of η . Clearly, as the fraction of relaxation energy converted to Rb^{*} kinetic energy is increased from 10% to 15%, the initial speed, and even more so the asymptotic value for long evolution times rises significantly. Table 3 collects the results obtained for various values of η . It can be seen that a fairly small $\eta \geq 10\%$ is enough to induce the ejection of the Rb^{*}-He complex. For a value $\eta = 12.5\%$, the asymptotic value of the Rb^{*}-He velocity matches best the experimental one measured for maximum $\Pi_{3/2}$ -excitation at $\lambda = 776$ nm.

Now that we have established the Rb^{*}-He formation and desorp-

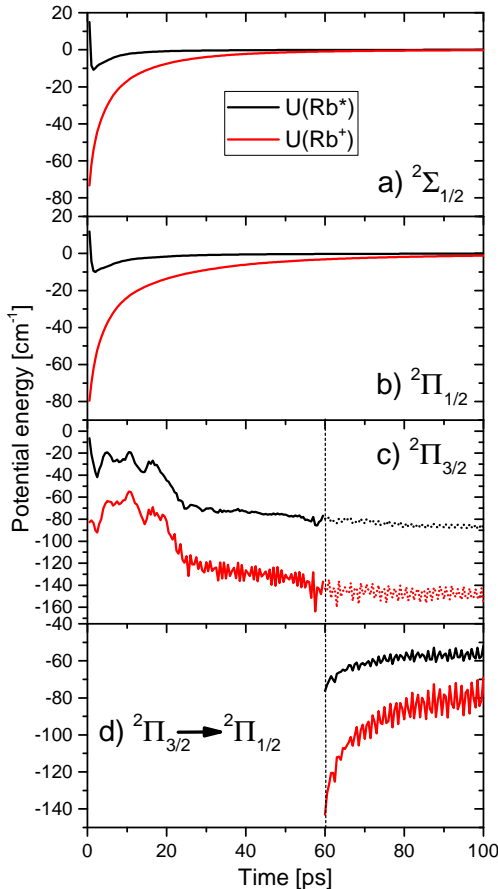


Fig. 9 (Color online) Simulated energies of the Rb-atom excited into various states interacting with the surrounding distribution of He atoms (black lines), and of the Rb⁺ ion for the same momentary geometry (red lines). In d), the excited state of Rb is suddenly switched from $\Pi_{3/2}$ to $\Pi_{1/2}$ to simulate the dynamics initiated by spin-relaxation.

tion mechanisms, we can take our comparative study one step further and compute from the simulation results the electron binding energies to compare with the experimental photoelectron spectra. For this, we evaluate the interaction energy of the Rb^{*} atom and of the Rb⁺ ion with the droplet by calculating, respectively,

$$U^*(t) = \int d\mathbf{r} \gamma_{He-Rb^*}(|\mathbf{r} - \mathbf{r}_{Rb^*}|) \rho(\mathbf{r}, t) \quad (5)$$

and

$$U^+(t) = \int d\mathbf{r} \gamma_{He-Rb^+}(|\mathbf{r} - \mathbf{r}_{Rb^+}|) \rho(\mathbf{r}, t). \quad (6)$$

Here the He-Rb⁺ pair potential is taken from Ref.³⁷.

The interaction energies $U^*(t)$ and $U^+(t)$ are shown in Fig. 9 for

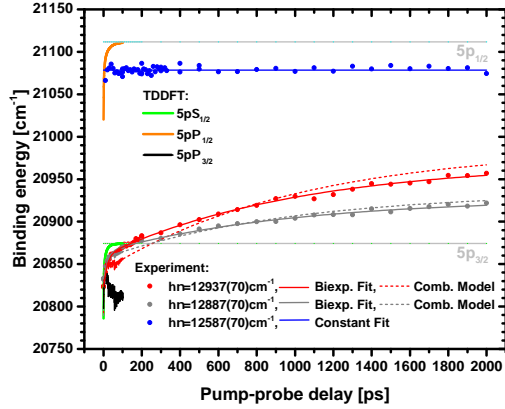


Fig. 10 Comparison of experimental and simulated electron binding energies. Thick solid lines: TD-DFT results. Dashed lines: Combined TD-DFT and analytical model. Thin solid lines: Biexponential fits of the experimental data.

Rb^{*} in the $\Sigma_{1/2}$ -state in a), in the $\Pi_{1/2}$ -state in b), and in the $\Pi_{3/2}$ -state in c). Fig. 9 d) shows the evolution following the sudden relaxation of Rb^{*} into the $\Sigma_{1/2}$ -state at $t = 60$ ps. The prompt desorption of Rb^{*} in the $\Sigma_{1/2}$ and $\Pi_{1/2}$ -states is seen as a sudden drop of $U^*(t)$ near $t = 0$ followed by a slow rise towards zero due to long-range van der Waals attraction as Rb^{*} departs from the He droplet. Due to the purely attractive interaction of the Rb⁺ ion with the He droplet, $U^+(t)$ monotonically rises to zero. The exciplex formation dynamics in the $\Pi_{3/2}$ -state is reflected by the irregular behavior of $U^*(t)$ and $U^+(t)$, eventually stabilizing at $t > 60$ ps at negative values, i.e. in a configuration where Rb^{*} is bound to the He droplet. Only when allowing for a sudden relaxation into the $\Pi_{1/2}$ -state at $t = 60$ ps, the Rb⁺-He exciplex receives a momentum “kick” and subsequently detaches from the He droplet, in spite of a rising $U^*(t)$. The asymptotic values of U^* and U^+ are then given by the binding energy of the free Rb^{*}-He exciplex configuration. The fast oscillations at $t > 65$ ps indicate that Rb⁺-He keeps vibrating as it is ejected.

5 Discussion: Experiment vs. theory

Knowledge of the interaction energies $U^*(t)$ and $U^+(t)$ allows us now to determine the electron binding energy $E_b = U^+(t) - U^*(t)$ and to compare it with the experimental photoelectron spectra. Here, $U^*(t)$ and $U^+(t)$ are referenced to their asymptotic values, i.e. the binding energies of free Rb^{*} and Rb⁺, respectively. The resulting binding energies E_b are depicted as thick colored lines in Fig. 10 in the range of delay times 0–100 ps. Compared to the experimental values we note both matches and deviations. The TD-DFT value of E_b for the $\Pi_{1/2}$ -state (red line) converges within 100 ps to the value of the free Rb⁺(5p_{1/2})-atom, as in the simulation Rb^{*} in that state detaches from the droplet. In contrast, the experimental values (blue symbols) are constant and below the atomic value because most of the atoms actually remain bound to the He droplet, see section 3.2.

The TD-DFT values for the $\Sigma_{1/2}$ -state (green line) quickly rise to $E_{5p3/2}$ within a few tens of ps, again due to prompt desorption, yielding free Rb* $5p_{3/2}$ atoms. The experimental values for excitation at 12,937 and 12,887 cm⁻¹ (red and grey symbols) show a very similar increase in that time range. This supports our conclusion that the fast dynamics observed both in the photoelectron peak position and in the yield of photoions results from prompt desorption of the $\Sigma_{1/2}$ -component of the excited state.

The TD-DFT curve for the $\Pi_{3/2}$ -state without relaxation (black line) drops in binding energy, at odds with the experiment. However, when $\Pi_{3/2} \rightarrow \Pi_{1/2}$ -relaxation is included, the simulated curve also rises, staying only slightly below the experimental values in the time range 20–100 ps.

Thus, we achieve good agreement of our extended TD-DFT simulations and experiment with regard to the fast (tens of ps) desorption of the $\Sigma_{1/2}$ -state, and qualitative agreement with regard to the desorption of the $\Pi_{3/2}$ -state when allowing for spin-relaxation. The lacking quantitative agreement is not surprising given the simplicity of our assumption – instantaneous spin-relaxation. Naturally, this relaxation process has its own time dependence.

If we identify the latter with our observed slow dynamics of photoelectron spectra and ion yields, we can make up a more realistic, combined model. Hereby we account for the populations $p_{\Sigma_{1/2}}$ in the $\Sigma_{1/2}$ -state and $p_{\Pi_{3/2}}$ in the $\Pi_{3/2}$ state, which are determined by the spectral profile of the laser $I_\ell(hv)$. The coefficients $p_{\Sigma_{1/2}, \Pi_{3/2}}$ are derived from the state-selective absorption profiles $I_\Sigma(hv)$ and $I_\Pi(hv)$ using LeRoy's LEVEL program⁷¹ based on the spin-orbit corrected pseudodiatomic potentials by Callegari and Ancilotto⁶². In a second step, the absorption profiles are weighted with $I_\ell(hv)$ and integrated over $h\nu$, yielding $p(\Pi_{3/2}) = 0.28$ for the center frequency $h\nu = 12,937$ cm⁻¹ and $p(\Pi_{3/2}) = 0.52$ for $h\nu = 12,887$ cm⁻¹. The transient energy of the $\Pi_{3/2}$ -state, $E_{\Pi_{3/2}}(t)$, consists of a contribution $[U_{\Pi_{3/2} \rightarrow \Pi_{1/2}}^+ - U_{\Pi_{3/2} \rightarrow \Pi_{1/2}}^*]$ which relaxes to $\Pi_{1/2}$, and a contribution $[U_{\Pi_{3/2}}^+ - U_{\Pi_{3/2}}^*]$ which remains in the $\Pi_{3/2}$ -state. When assuming an exponential time dependence of the relaxation with a time constant τ , we get

$$\begin{aligned} E(t) &= p_{\Sigma_{1/2}} \cdot [U_{\Sigma_{1/2}}^+ - U_{\Sigma_{1/2}}^*] + p_{\Pi_{3/2}} \cdot e^{-\ln 2/\tau} \cdot [U_{\Pi_{3/2}}^+ - U_{\Pi_{3/2}}^*] \\ &+ p_{\Pi_{3/2}} \cdot (1 - e^{-\ln 2/\tau}) \cdot [U_{\Pi_{3/2} \rightarrow \Pi_{1/2}}^+ - U_{\Pi_{3/2} \rightarrow \Pi_{1/2}}^*]. \end{aligned}$$

Here, $U^*(t)$ and $U^+(t)$ are extrapolated by constants for the $\Sigma_{1/2}$ and $\Pi_{3/2}$ -states and by an exponential function for the $\Pi_{3/2} \rightarrow \Pi_{1/2}$ case for long times $t > 200$ ps. For simplicity, we neglect the 60 ps time delay between excitation and relaxation which is short compared to the full relaxation dynamics. If we assign to τ the experimental value of the slow time constant of the fit of photoelectron energies, τ_e^* , we obtain the dashed lines in Fig. 10, which nicely match the experimental data. This confirms our concept that the slow variations of ion and electron signals spanning hundreds of ps are due to spin-relaxation which proceeds on that time scale and causes the desorption of RbHe exciplexes, which would otherwise remain bound to the He droplet surface.

6 Conclusion

In summary, we have presented a detailed study of the formation and desorption dynamics of RbHe exciplexes initiated by laser excitation of Rb atoms attached to He nanodroplets. Experimentally, the two-color femtosecond pump-probe photoionization scheme allows us to selectively probe the dynamics of the lowest three excited states of the Rb-He droplet complex. Both photoion and photoelectron signals feature pump-probe dynamics proceeding on two distinct time scales (30 and 700 ps). By comparing with time-dependent DFT simulations, complemented by a spin-relaxation mechanism, we conclude that the fast dynamics is due to prompt desorption of Rb atoms when exciting the $\Sigma_{1/2}$ -state. The slow desorption of RbHe exciplexes is induced by $\Pi_{3/2} \rightarrow \Sigma_{1/2}$ spin-relaxation. By analyzing the rearrangement of the He surrounding the Rb atom in the $\Pi_{3/2}$ -state, we infer a formation time of the RbHe exciplex of 20 ps. When exciting the lowest state of the Rb-He droplet, $\Pi_{1/2}$, we find that a small fraction of Rb atoms desorbs as free atoms, as predicted by the DFT simulation, whereas the larger fraction Rb atoms remains bound to the He droplets.

6.0.1 Acknowledgements We would like to thank Marcel Drabbels for useful exchanges. Financial support by the Deutsche Forschungsgemeinschaft (MU 2347/6-1 and IRTG 2079) is gratefully acknowledged. This work has been performed under Grants No. FIS2014-52285-C2-1-P and FIS2017-87801-P from DGI, Spain, and 2014SGR401 from Generalitat de Catalunya. MB thanks the Université Féderale Toulouse Midi-Pyrénées for financial support throughout the “Chaires d’Attractivité 2014” Programme IMDYNHE. The dynamics simulations presented in this work have been carried out thanks to the HPC resources of CALMIP supercomputing center (Grant P1039).

References

- C. George, M. Ammann, B. D'Anna, D. J. Donaldson and S. A. Nizkorodov, *Chem. Rev.*, 2015, **115**, 4218–4258.
- J. Schneider, D. Bahnemann, J. Ye, G. L. Puma and D. D. Dionysiou, *Photocatalysis: Fundamentals and Perspectives*, The Royal Society of Chemistry, Cambridge CB4 0WF, UK, 2016.
- J. P. Toennies and A. F. Vilesov, *Angew. Chem. Int. Ed.*, 2004, **43**, 2622.
- F. Stienkemeier and K. Lehmann, *J. Phys. B*, 2006, **39**, R127.
- F. Ancilotto, G. DeToffol and F. Toigo, *Phys. Rev. B*, 1995, **52**, 16125–16129.
- F. Stienkemeier, J. Higgins, C. Callegari, S. I. Kanorsky, W. E. Ernst and G. Scoles, *Z. Phys. D*, 1996, **38**, 253–263.
- M. Barranco, R. Guardiola, S. Hernández, R. Mayol, J. Navarro and M. Pi, *J. Low Temp. Phys.*, 2006, **142**, 1–81.
- C. Stark and V. V. Kresin, *Phys. Rev. B*, 2010, **81**, 085401.
- L. A. der Lan, P. Bartl, C. Leidlmair, H. Schöbel, R. Jochum, S. Denifl, T. D. Märk, A. M. Ellis and P. Scheier, *J. Chem. Phys.*, 2011, **135**, 044309.
- L. An der Lan, P. Bartl, C. Leidlmair, H. Schöbel, S. Denifl, T. D. Märk, A. M. Ellis and P. Scheier, *Phys. Rev. B*, 2012, **85**, 115414.

- 11 Höller, Johannes, Krotscheck, Eckhard and Zillich, Robert E., *Eur. Phys. J. D*, 2015, **69**, 198.
- 12 F. Calvo, *Phys. Rev. B*, 2017, **95**, 035429.
- 13 M. Mudrich and F. Stienkemeier, *Int. Rev. Phys. Chem.*, 2014, **33**, 301–339.
- 14 F. Ancilotto, M. Barranco, F. Coppens, J. Eloranta, N. Halberstadt, A. Hernando, D. Mateo and M. Pi, *Int. Rev. Phys. Chem.*, 2017, **36**, 621–707.
- 15 E. Loginov and M. Drabbels, *J. Phys. Chem. A*, 2007, **111**, 7504–7515.
- 16 L. Fechner, B. Grüner, A. Sieg, C. Callegari, F. Ancilotto, F. Stienkemeier and M. Mudrich, *Phys. Chem. Chem. Phys.*, 2012, **14**, 3843.
- 17 A. Kautsch, M. Koch and W. E. Ernst, *J. Phys. Chem. A*, 2013, **117**, 9621–9625.
- 18 F. Lindebner, A. Kautsch, M. Koch and W. E. Ernst, *Int. J. Mass Spectrom.*, 2014, **365–366**, 255–259.
- 19 M. Koch, G. Auböck, C. Callegari and W. E. Ernst, *Phys. Rev. Lett.*, 2009, **103**, 035302.
- 20 S. Smolarek, N. B. Brauer, W. J. Buma and M. Drabbels, *J. Am. Chem. Soc.*, 2010, **132**, 14086–14091.
- 21 A. Hernando, M. Barranco, M. Pi, E. Loginov, M. Langlet and M. Drabbels, *Phys. Chem. Chem. Phys.*, 2012, **14**, 3996–4010.
- 22 D. Mateo, A. Hernando, M. Barranco, E. Loginov, M. Drabbels and M. Pi, *Phys. Chem. Chem. Phys.*, 2013, **15**, 18388–18400.
- 23 J. von Vangerow, A. Sieg, F. Stienkemeier, M. Mudrich, A. Leal, D. Mateo, A. Hernando, M. Barranco and M. Pi, *J. Phys. Chem. A*, 2014, **118**, 6604–6614.
- 24 J. von Vangerow, O. John, F. Stienkemeier and M. Mudrich, *J. Chem. Phys.*, 2015, **143**, 034302.
- 25 A. Sieg, J. von Vangerow, F. Stienkemeier, O. Dulieu and M. Mudrich, *J. Phys. Chem. A*, 2016, **120**, 7641–7649.
- 26 J. von Vangerow, F. Coppens, A. Leal, M. Pi, M. Barranco, N. Halberstadt, F. Stienkemeier and M. Mudrich, *J. Phys. Chem. Lett.*, 2017, **8**, 307–312.
- 27 A. Przystawik, S. Göde, T. Döppner, J. Tiggesbäumker and K. H. Meiwes-Broer, *Phys. Rev. A*, 2008, **78**, 021202.
- 28 S. Müller, S. Krapf, T. Koslowski, M. Mudrich and F. Stienkemeier, *Phys. Rev. Lett.*, 2009, **102**, 183401.
- 29 A. Kautsch, M. Koch and W. E. Ernst, *Phys. Chem. Chem. Phys.*, 2015, **17**, 12310–12316.
- 30 J. Reho, J. Higgins, C. Callegari, K. K. Lehmann and G. Scoles, *J. Chem. Phys.*, 2000, **113**, 9694–9701.
- 31 F. R. Brühl, R. A. Trasca and W. E. Ernst, *J. Chem. Phys.*, 2001, **115**, 10220–10224.
- 32 C. P. Schulz, P. Claas and F. Stienkemeier, *Phys. Rev. Lett.*, 2001, **87**, 153401.
- 33 G. Dropelmann, O. Bünermann, C. P. Schulz and F. Stienkemeier, *Phys. Rev. Lett.*, 2004, **93**, 0233402.
- 34 M. Mudrich, G. Dropelmann, P. Claas, C. Schulz and F. Stienkemeier, *Phys. Rev. Lett.*, 2008, **100**, 023401.
- 35 S. Müller, M. Mudrich and F. Stienkemeier, *J. Chem. Phys.*, 2009, **131**, 044319.
- 36 M. Theisen, F. Lackner and W. E. Ernst, *Phys. Chem. Chem. Phys.*, 2010, **12**, 14861–14863.
- 37 A. Leal, D. Mateo, A. Hernando, M. Pi, M. Barranco, A. Ponti, F. Cargnani and M. Drabbels, *Phys. Rev. B*, 2014, **90**, 224518.
- 38 E. Loginov, A. Hernando, J. A. Beswick, N. Halberstadt and M. Drabbels, *J. Phys. Chem. A*, 2015, **119**, 6033–6044.
- 39 M. Kuhn, M. Renzler, J. Postler, S. Ralsen, S. Spieler, M. Simpson, H. Linnartz, A. G. G. M. Tielen, J. Cami, A. Mauacher, Y. Wang, M. Alcamí, F. Martín, M. K. Beyer, R. Wester, A. Lindinger and P. Scheier, *Nat. Comm.*, 2016, **7**, 13550.
- 40 N. B. Brauer, S. Smolarek, E. Loginov, D. Mateo, A. Hernando, M. Pi, M. Barranco, W. J. Buma and M. Drabbels, *Phys. Rev. Lett.*, 2013, **111**, 153002.
- 41 M. Koch, A. Kautsch, F. Lackner and W. E. Ernst, *J. Phys. Chem. A*, 2014, **118**, 8373–8379.
- 42 Y. Seki, T. Takayanagi and M. Shiga, *Phys. Chem. Chem. Phys.*, 2017, **19**, 13798–13806.
- 43 G. Auböck, J. Nagl, C. Callegari and W. E. Ernst, *Phys. Rev. Lett.*, 2008, **101**, 035301.
- 44 M. Theisen, F. Lackner and W. E. Ernst, *J. Phys. Chem. A*, 2011, **115**, 7005–7009.
- 45 T. Takayanagi and M. Shiga, *Phys. Chem. Chem. Phys.*, 2004, **6**, 3241.
- 46 M. Leino, A. Viel and R. E. Zillich, *J. Chem. Phys.*, 2011, **134**, 024316.
- 47 C. Giese, T. Mullins, B. Grüner, M. Weidmüller, F. Stienkemeier and M. Mudrich, *J. Chem. Phys.*, 2012, **137**, 244307.
- 48 S. H. Patil, *J. Chem. Phys.*, 1991, **94**, 8089–8095.
- 49 F. Ancilotto, M. Barranco, F. Caupin, R. Mayol and M. Pi, *Phys. Rev. B*, 2005, **72**, 214522.
- 50 M. Pi, F. Ancilotto, F. Coppens, N. Halberstadt, A. Hernando, A. Leal, D. Mateo, R. Mayol and M. Barranco, *4He-DFT BCN-TLS: A Computer Package for Simulating Structural Properties and Dynamics of Doped Liquid Helium-4 Systems*. <https://github.com/bcntls2016/>, 2017.
- 51 D. Mateo, A. Hernando, M. Barranco, R. Mayol and M. Pi, *Phys. Rev. B*, 2011, **83**, 174505.
- 52 A. Hernando, M. Barranco, R. Mayol, M. Pi and M. Krośnicki, *Phys. Rev. B*, 2008, **77**, 024513.
- 53 J. Pascale, *Phys. Rev. A*, 1983, **28**, 632–644.
- 54 O. Bünermann, G. Dropelmann, A. Hernando, R. Mayol and F. Stienkemeier, 2007, **111**, 12684.
- 55 K. Hirano, K. Enomoto, M. Kumakura, Y. Takahashi and T. Yabuzaki, *Phys. Rev. A*, 2003, **68**, 012722.
- 56 A. T. J. B. Eppink and D. H. Parker, *Rev. Sci. Instrum.*, 1997, **68**, 3477.
- 57 A. Wituschek, J. von Vangerow, J. Grzesiak, F. Stienkemeier and M. Mudrich, *Rev. Sci. Instrum.*, 2016, **87**, 083105.
- 58 G. A. Garcia, L. Nahon and I. Powis, *Rev. Sci. Instrum.*, 2004, **75**, 4989–4996.
- 59 B. Dick, *Phys. Chem. Chem. Phys.*, 2014, **16**, 570–580.
- 60 A. Braun and M. Drabbels, *jcp*, 2007, **127**, 114303.
- 61 G. S. Mudholkar and A. D. Hutson, *J. Stat. Plan. Inference*, 2000, **83**, 291–309.

- 62 C. Callegari and F. Ancilotto, *J. Phys. Chem. A*, 2011, **115**, 6789–6796.
- 63 M. Theisen, F. Lackner, G. Krois and W. E. Ernst, *J. Phys. Chem. Lett.*, 2011, **2**, 2778–2782.
- 64 D. Buchta, S. R. Krishnan, N. B. Brauer, M. Drabbels, P. O’Keeffe, M. Devetta, M. Di Fraia, C. Callegari, R. Richter, M. Coreno, K. C. Prince, F. Stienkemeier, R. Moshammer and M. Mudrich, *J. Phys. Chem. A*, 2013, **117**, 4394–4403.
- 65 E. Loginov, D. Rossi and M. Drabbels, *Phys. Rev. Lett.*, 2005, **95**, 163401.
- 66 D. S. Peterka, J. H. Kim, C. C. Wang and D. M. Neumark, *J. Phys. Chem. B*, 2006, **110**, 19945–19955.
- 67 C. C. Wang, O. Kornilov, O. Gessner, J. H. Kim, D. S. Peterka and D. M. Neumark, 2008, **112**, 9356.
- 68 M. Leino, A. Viel and R. E. Zillich, 2008, **129**, 184308.
- 69 E. Loginov and M. Drabbels, *J. Phys. Chem. A*, 2014, **118**, 2738–2748.
- 70 L. Krause, in *Adv. Chem. Phys.*, edited by J. W. McGowan (Wiley, New York), 1975.
- 71 R. LeRoy, *Chemical Physics Research Report*, University of Waterloo, CP-555, 1995, 1995.

4.3. *SUPERVISED WORK: DYNAMICS OF SUPERFLUID HELIUM NANODROPLETS DOPED WITH POTASSIUM*

4.3 Supervised work: Dynamics of superfluid helium nanodroplets doped with potassium

Part II

Head-on collisions and capture by quantised vortices

Chapter 5

Introduction

5.1 Head-on collisions

It is well known that helium drops readily capture foreign atoms and molecules[1], and this ability has had a considerable influence on the chemistry and physics of these systems[2]. Among the studies carried out in the past on atom-drop collisions, let us mention those aiming at experimentally determining the density profiles of large ^4He and ^3He droplets from the scattering of Ar and Kr atoms off helium droplets, which have been analysed within density functional theory (DFT)[3,4]; the microscopic simulation of the scattering of ^3He and ^4He atoms from inhomogeneous liquid helium systems[5,6]; and an earlier theoretical work on the scattering of ^4He atoms from ^4He droplets within a liquid drop plus optical model approach[7].

Very recently, time-dependent density functional theory (TDDFT) has been used to address the capture of Cs or Ne atoms by ^4He nanodroplets[8,9]. The Cs capture was treated fully three dimensionally with the Cs atom described as a classical particle, whereas for the Ne capture study the Ne atom was described quantum mechanically, but the description was strictly one dimension.

Motivated by recent experiments that use Xe atoms to visualize vortex arrays in very large helium droplets[10,11], we present here a first step toward the description of the capture of Xe atoms by helium droplets, namely head-on collisions of Xe atoms against a $^4\text{He}_{1000}$ droplet. A discussion on the dynamic capture of Xe atoms by droplets hosting vortex lines and vortex arrays will be provided by a forthcoming study combining DFT

simulation of vortex arrays as in Refs.[12,13] for helium nanocylinders and nanodroplets and collision with Xe atoms as in this work. Whenever possible, the results for Xe, a heliophilic atom, are contrasted with results for Cs, a heliophobic atom with similar mass.

5.2 Capture by quantised vortices

It is well established that helium droplets can readily capture in their interior almost any atom or molecule interacting with them, as first shown for the case of Ne atoms[1], with the notable exception of alkali[2] and some alkaline-earth[3] atoms. This property, together with the extremely low temperature (T) achieved in helium droplets – of the order of 0.4 K – makes them the perfect ultracold and inert environment for hosting and studying isolated atoms and molecules, which is at the basis of current applications of helium droplets for spectroscopic studies of atoms and molecules. Besides, the superfluid nature of helium facilitates binary encounters of atoms/molecules in the bulk of the droplet while absorbing the energy released upon recombination, making possible chemical reactions which would not otherwise occur in the gas phase. These unique properties of helium droplets have had a huge impact on their study[4-8].

The pickup of Ar, Kr and Xe atoms in the gas phase by ${}^4\text{He}_N$ droplets with $N > 10^3$ atoms produced by nozzle beam expansions was described about twenty years ago by Toennies and coworkers[9]. In these experiments, the droplets in the helium beam were deflected by impacting with a secondary beam made of rare gas atoms.

Recently, a technique has been introduced to determine the size of large He droplets ($N > 10^5$). It is based on the attenuation of a continuous droplet beam through collisions with Ar atoms at room temperature[10]. The pickup chamber of the droplet beam apparatus is filled with argon gas and the helium droplets experience multiple, isotropic collisions with the Ar atoms on their way towards the detection chamber. Large helium droplets could also be doped in this way. This method, using Xe atoms, has been instrumental for detecting and imaging quantised vortex arrays in helium droplets[11,12]. Xe atoms were used in these experiments because of their large sensitivity to the X-ray coherent diffractive imaging employed to detect them within the helium droplets. Experiments with large superfluid helium droplets are reviewed in a recent publication[14].

The impurity-droplet interaction in the presence of vortices is also relevant as the first stage of a more complex process leading to the formation of nanowires, see e.g. ref. 15-18. Long filaments made of micrometer-sized solid hydrogen particles trapped on quantised vortex cores were used to directly image the vortex reconnection between quantised vortices in superfluid helium[19].

The impact and capture of impurities interacting with pure helium droplets have been addressed recently within time-dependent density functional theory (TDDFT). Real-time simulations have been carried out for heliophobic[20] (Cs) and heliophilic[21] (Ne) atoms. In addition to the TDDFT equation for ^4He , heavy impurities are treated as classical particles using Newton's equation of motion, whereas a time-dependent Schrödinger equation has been used in the case of light impurities within the mean field model[21,22]. A comparison between the results for head-on collisions of Cs and Xe atoms – heliophobic and heliophilic atoms of similar mass – has been presented in ref. 23.

In this work, we present the results obtained within TDDFT for the collision and capture of Xe and Ar atoms by a $^4\text{He}_{1000}$ droplet at different kinetic energies and impact parameters. Special attention is paid to the time-dependent interaction of Xe and Ar atoms with helium nanodroplets hosting vortex lines, and to the effect of multi-doped vortex arrays in large helium droplets.

Due to the heavy computational cost of the TDDFT simulations presented here, we address only a few facets of the capture process that we consider of experimental relevance rather than carrying out a systematic study of the process. In particular:

- We study the capture of Xe atoms by a ^4He nanodroplet, both for head-on collisions and for different impact parameters, with velocities ranging from thermal values up to several hundred m/s. The results of peripheral collisions with different values of the impact parameter are used to estimate the cross section for the Xe capture.
- We study how a Xe atom dynamically interacts with a droplet hosting a vortex line, under different initial conditions resulting in different velocity regimes of the impurity as it collides with the vortex core:
 - i) a Xe atom initially at rest on the droplet surface and sinking under the effect of solvation forces

- ii) a head-on collision of a moving Xe or Ar atom against the ${}^4\text{He}$ nanodroplet.
- We study the stationary state of a large ${}^4\text{He}_{15000}$ droplet hosting a ring of six vortex lines, doped with Ar atoms completely filling all six vortex cores. This is the simplest system that mimics those experimentally described in ref. 11, where doped vortex arrays embedded in rotating ${}^4\text{He}$ microdroplets have been imaged.

Multimedia materials accompany this paper, showing the real-time dynamics of several impact/capture processes described here. These materials are presented in the ESI document. They constitute an important part of this work, since often it is only by viewing how a complex microscopic process unfolds in real-time that one can catch important physical details which would otherwise escape in a written account.

Chapter 6

Results

6.1 Head-on collisions



Head-on Collisions of Xe Atoms Against Superfluid ^4He Nanodroplets

François Coppens¹ · Antonio Leal² ·
Manuel Barranco² · Nadine Halberstadt¹ ·
Martí Pi²

Received: 8 July 2016 / Accepted: 26 October 2016
© Springer Science+Business Media New York 2016

Abstract We study the head-on collision of a heliophilic xenon atom with a superfluid ^4He droplet made of 1000 atoms. At variance with the findings for a heliophobic cesium atom of a similar atomic weight, it is found that the xenon atom has to hit the droplet with a large kinetic energy in order to get across it without being captured. When it is not captured, the xenon impurity does not emerge as a bare atom; instead, due to its heliophilic character it carries away some helium atoms.

Keywords Superfluid ^4He droplets · Density functional theory · Atomic collisions

1 Introduction

It is well known that helium drops readily capture foreign atoms and molecules [1], and this ability has had a considerable influence on the chemistry and physics of these systems [2]. Among the studies carried out in the past on atom–drop collisions, let us mention those aiming at experimentally determining the density profiles of large ^4He and ^3He droplets from the scattering of Ar and Kr atoms off helium droplets, which have been analyzed within density functional theory (DFT) [3, 4]; the microscopic simulation of the scattering of ^3He and ^4He atoms from inhomogeneous liquid helium systems [5, 6]; and an earlier theoretical work on the scattering of ^4He atoms from ^4He droplets within a liquid drop plus optical model approach [7].

✉ François Coppens
francois.coppens@irsamc.ups-tlse.fr

¹ Laboratoire des Collisions, Agrégats, Réactivité, IRSAMC, UMR 5589, CNRS,
Université Toulouse 3, 118 Route de Narbonne, 31062 Toulouse Cedex 09, France

² Departament FQA, Facultat de Física, and IN²UB, Universitat de Barcelona, Diagonal 645,
08028 Barcelona, Spain

Very recently, time-dependent density functional theory (TDDFT) has been used to address the capture of Cs or Ne atoms by ^4He nanodroplets [8,9]. The Cs capture was treated fully three dimensionally with the Cs atom described as a classical particle, whereas for the Ne capture study the Ne atom was described quantum mechanically, but the description was strictly one dimension.

Motivated by recent experiments that use Xe atoms to visualize vortex arrays in very large helium droplets [10,11], we present here a first step toward the description of the capture of Xe atoms by helium droplets, namely head-on collisions of Xe atoms against a $^4\text{He}_{1000}$ droplet. A discussion on the dynamic capture of Xe atoms by droplets hosting vortex lines and vortex arrays will be provided by a forthcoming study combining DFT simulation of vortex arrays as in Refs. [12,13] for helium nanocylinders and nanodroplets and collision with Xe atoms as in this work. Whenever possible, the results for Xe, a heliophilic atom, are contrasted with results for Cs, a heliophobic atom with similar mass.

2 Method and Results

We use the He density functional approach to describe the helium droplet, whereas the Xe atom is treated classically given its large mass. Within TDDFT, we represent the He droplet by a complex effective wave function $\Psi_{\text{He}}(\mathbf{r}, t)$ such that the atomic density $\rho(\mathbf{r}, t)$ fulfills $\rho(\mathbf{r}, t) = |\Psi_{\text{He}}(\mathbf{r}, t)|^2$; the Xe atom is represented by its classical position $\mathbf{r}_{\text{Xe}}(t)$ obeying Newton's equation of motion. We solve the coupled equations

$$\begin{aligned} i\hbar \frac{\partial}{\partial t} \Psi_{\text{He}} &= \left[-\frac{\hbar^2}{2m_{\text{He}}} \nabla^2 + \frac{\delta \mathcal{E}_{\text{He}}}{\delta \rho(\mathbf{r})} + V_X(|\mathbf{r} - \mathbf{r}_{\text{Xe}}|) \right] \Psi_{\text{He}} \\ m_{\text{Xe}} \ddot{\mathbf{r}}_{\text{Xe}} &= -\nabla_{\mathbf{r}_{\text{Xe}}} \left[\int d\mathbf{r} \rho(\mathbf{r}) V_X(|\mathbf{r} - \mathbf{r}_{\text{Xe}}|) \right] = - \int d\mathbf{r} [\nabla \rho(\mathbf{r})] V_X(|\mathbf{r} - \mathbf{r}_{\text{Xe}}|) \end{aligned} \quad (1)$$

where \mathcal{E}_{He} is the potential energy per unit volume for the functional of Ref. [14] and V_X the Xe–He pair potential taken from Ref. [15]. We refer the reader to Ref. [8] for details on how to solve Eq. (1).

We consider a droplet made of $N = 1000$ helium atoms. Its ground state structure is obtained using DFT and gives a sharp density radius of about 22.2 Å. Then, the dynamics is initiated by placing the Xe atom 32 Å away from the center of mass (COM) of the droplet with an impact parameter equal to zero (head-on collision). The simulations are carried out for initial Xe velocities v_0 ranging from 200 to 600 m/s in the system of reference of the droplet, corresponding to kinetic energies between 315.8 and 2842 K. These energies can be compared to the solvation energy of a Xe atom at the center of a $^4\text{He}_{1000}$ droplet, $S_{\text{Xe}} = E(\text{Xe}@^4\text{He}_{1000}) - E(^4\text{He}_{1000}) = -316.3$ K. For the sake of comparison, the solvation energy of Cs is -5.2 K and its equilibrium position is in a dimple at the outer droplet surface, about 26.6 Å from its center. Thermal Xe atoms ($v_0 \sim 240$ m/s) are used in the experiments [10,11], and the average drop velocity is about 170 m/s [16].

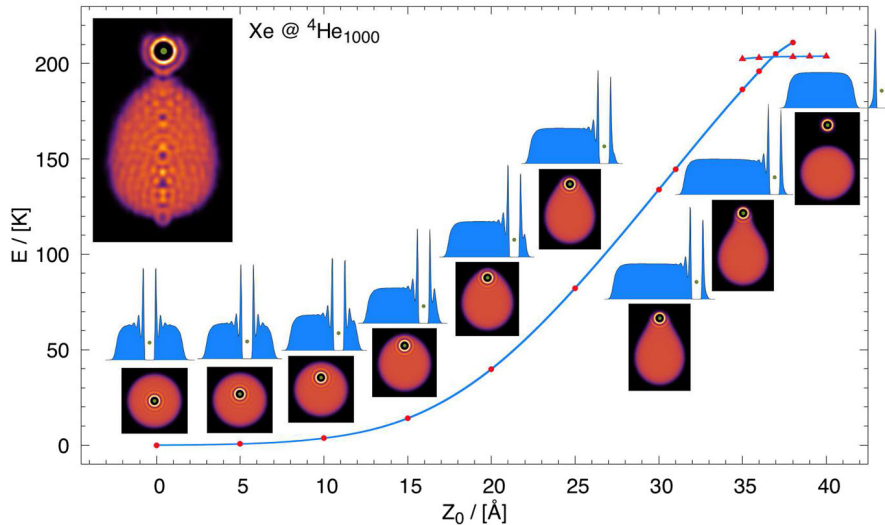


Fig. 1 Energy of the $\text{Xe}@\text{He}_{1000}$ complex as a function of the distance between the Xe atom and the COM of the droplet. Several two-dimensional helium densities and density profiles are shown for distances between 0 and 40 Å in 5 Å steps. Connected (dots) and disconnected (triangles) helium configurations are shown (see text). Top left inset: snapshot of the helium density at the first turning point during the dynamic evolution of a Xe atom (green dot) at $v_0 = 600 \text{ m/s}$ attained 78 ps after it has started (Color figure online)

Figure 1 shows the energy of the $\text{Xe}@\text{He}_{1000}$ complex referred to that of the equilibrium configuration (Xe at the center of the droplet, -5716.4 K) as a function of the distance between the Xe atom and the COM of the droplet. It is obtained by a constrained calculation similar to that presented in Ref. [17] for Ba^+ . With increasing distance, the stretched droplet–Xe configuration eventually breaks into a minicluster around the Xe atom containing about 22 helium atoms disconnected from the rest of the droplet. The appearance of this minicluster is at variance with the situation for a heliophobic impurity such as Cs [8]. The stretched (connected) configuration energies are represented by dots, the disconnected ones by triangles. The two corresponding curves cross at 37 \AA . At shorter distances, the connected configuration is stable and the disconnected one metastable, and at larger distances the roles are inverted. In an actual dynamics, the number of He atoms in the minicluster depends on the velocity of the Xe projectile.

Figure 2 displays two-dimensional plots of the helium density for Xe head-on colliding against the He_{1000} droplet at $v_0 = 200 \text{ m/s}$ and Fig. 3 the energy of the impinging atom as a function of time, with the corresponding plots for Cs collisions for the sake of comparison. It can be seen that for both species most of the initial kinetic energy is spent in piercing the droplet surface, after which the impurity moves inside the droplet at a velocity well below the critical Landau velocity v_L .

Figure 2 also shows that the collision launches a series of density waves in the droplet that are reflected at the droplet free surface producing complex interference patterns in its bulk. As an illustrative example, Fig. 4 shows the density profile along the incident direction (z axis) corresponding to the Xe collision at $v_0 = 200 \text{ m/s}$, 6 ps

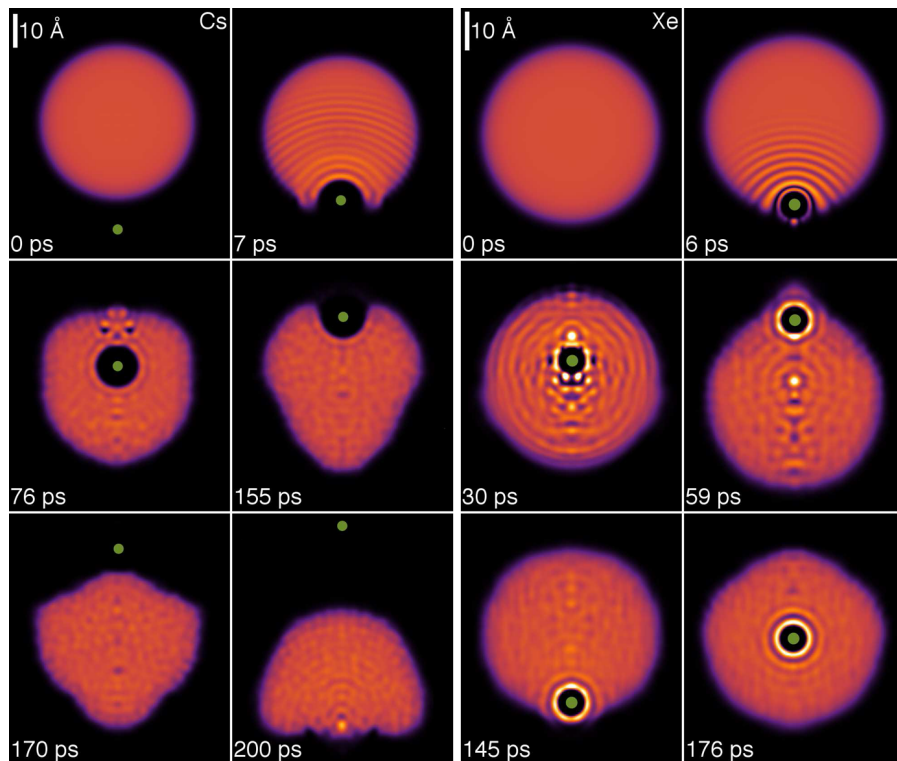


Fig. 2 Right panel: dynamic evolution of a Xe atom (big dot) approaching the ${}^4\text{He}_{1000}$ droplet from below at $v_0 = 200 \text{ m/s}$. The corresponding time is indicated in each frame. Left panel: same as left figure for a Cs atom (Color figure online)

after the process starts. The wave number associated with this wave can be estimated from the wavelength λ of the oscillations, $q = 2\pi/\lambda \sim 2.7 \text{ \AA}^{-1}$.

In the case of Xe, Figs. 2 and 3 reveal the appearance of turning points at which the velocity of the impurity is zero. Note that these points are not fixed during the dynamics since the droplet deforms due to the swift motion of Xe inside it; the droplet is not a rigid object and reacts to the motion of the impurity, with energy being transferred not only from the impurity to the droplet but also the other way around [18].

The top left inset in Fig. 1 shows a snapshot obtained at the first turning point for $v_0 = 600 \text{ m/s}$, with 57 He atoms around the Xe dopant. We have found that the Xe atom has to hit the droplet at a velocity above 600 m/s in order to go across the helium droplet; otherwise, it remains attached to the droplet. The kinetic energy lost by the Xe atom is partially deposited in the droplet and partially carried away by prompt-emitted helium atoms, i.e., atoms expelled early on in the collision and with a significant kinetic energy. The number of He atoms emitted during the first 78 ps is about 47. For comparison, about 19 atoms are emitted after 185 ps for $v_0 = 200 \text{ m/s}$. Eventually, the energy deposited into the droplet should be lost by atom evaporation; however, the time scale for this to happen is beyond the reach of any realistic simulation.

The piercing of the droplet by the Cs atom produces a density wave that travels on its surface and collapses at the surface region opposite to the hitting point. This

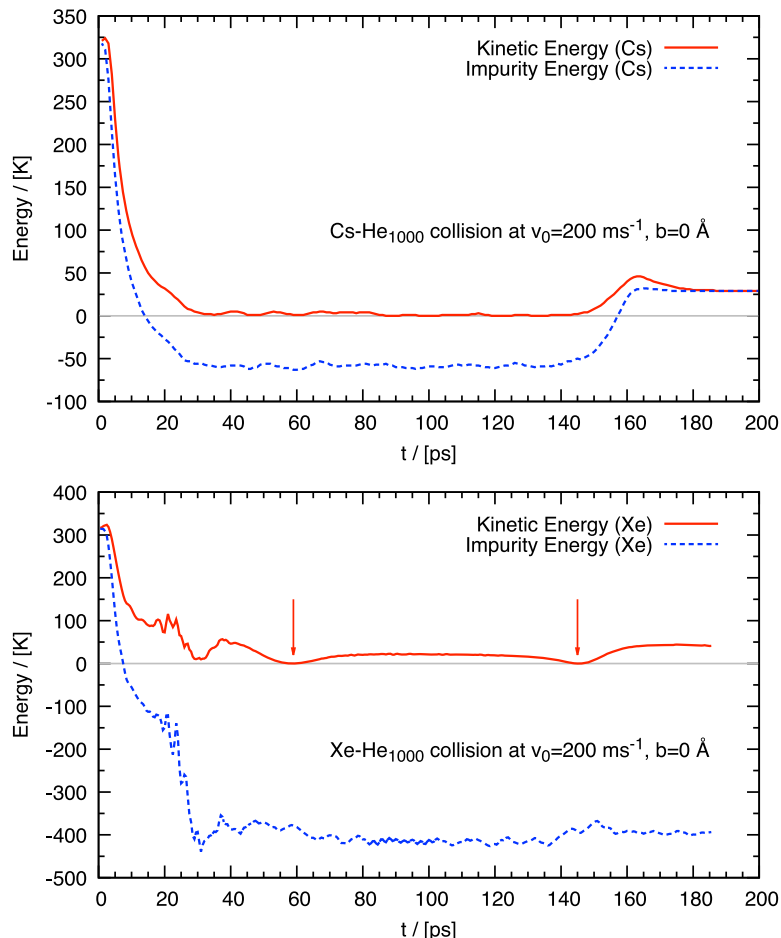


Fig. 3 Top figure: kinetic and total (kinetic plus potential) energy as a function of time of a Cs atom head-on colliding against a ${}^4\text{He}_{1000}$ droplet at $v_0 = 200 \text{ m/s}$. Bottom figure: same as top figure for a Xe atom. The vertical arrows indicate the first two turning points at 59 and 145 ps, whose corresponding helium densities are shown in the right panel of Fig. 2 (Color figure online)

collapse nucleates a vortex ring (the two dark spots in the 76-ps plot of the left panel of Fig. 2) [8].

It is worth pointing out that the falloff of the Xe velocity in the $t = 20 - 30$ -ps interval observed in Fig. 3 is due to the increase in its inertia due to the appearance of a dynamic “snowball”—a crust of helium atoms surrounding the Xe bubble indicated by the bright spots in Fig. 2—that is eventually washed out at larger times. At variance with our findings for Ba^+ [18], vortex rings have not been nucleated in the case of Xe; in particular, we have checked that the two dark spots in the 30-ps plot of the right panel of Fig. 2 for Xe do not correspond to a vortex ring.

The collapse of the Cs bubble at the surface of the droplet some 150 ps after the process gives back to the impurity part of the kinetic energy it has lost in the piercing

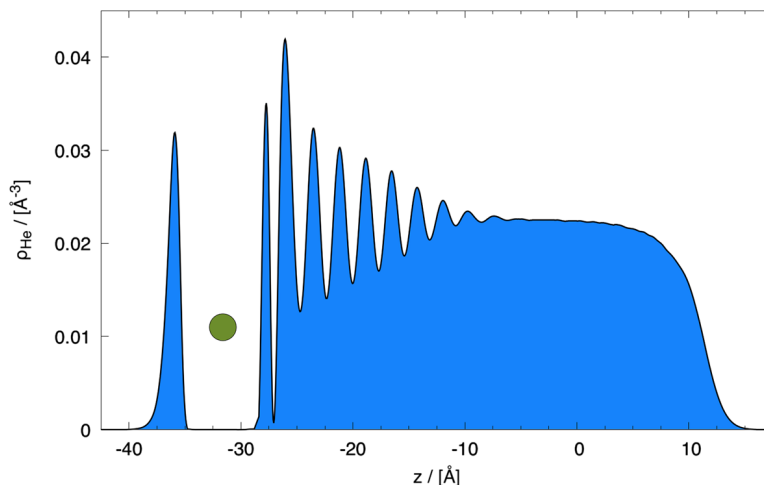


Fig. 4 Density profile of the He₁₀₀₀ droplet along the incident direction corresponding to the Xe collision at $v_0 = 200 \text{ m/s}$ after 6 ps (Color figure online)

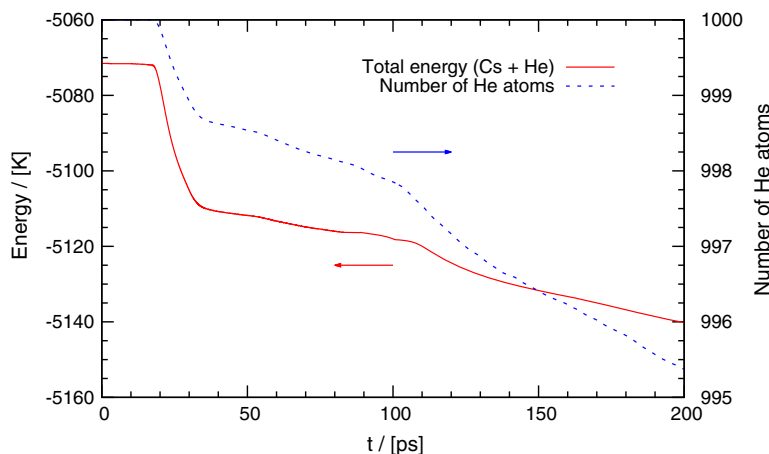


Fig. 5 Total energy (left scale) and number of atoms in the droplet (right scale) as a function of time for the Cs@⁴He₁₀₀₀ system at $v_0 = 200 \text{ m/s}$ (Color figure online)

of the droplet. The Cs atom is expelled at 64.5 m/s (corresponding to 33.6 K kinetic energy). The number of prompt-emitted helium atoms is 5, which is smaller than for Xe at the same collision energy (19 atoms). As shown in Fig. 5, they are preferentially emitted as a forward burst (first sharp drop around 20 ps in the number of atoms) and as a backward burst (second sharp drop slightly after 100 ps).

In conclusion, head-on collisions of xenon, a heliophilic atom, involve a kinetic energy exchange of the same order of magnitude as cesium, a heliophobic atom with similar mass. In both cases, this energy is largely dissipated by producing energetic waves in the droplet or it is carried away by promptly emitted helium atoms. The difference is that it takes a much higher velocity for xenon to go through the droplet

and escape than for cesium, as could be expected. Also, density builds up around the xenon during the dynamics, whereas a bubble is created around cesium.

Acknowledgements This work has been performed under Grants No. FIS2014-52285-C2-1-P from DGI, Spain, and 2014SGR401 from Generalitat de Catalunya and using HPC resources from CALMIP (Grant P1039). AL has been supported by the ME (Spain) FPI program, Grant No. BES-2012-057439. MB thanks the Université Féderale Toulouse Midi-Pyrénées for financial support through the “Chaires d’Attractivité 2014” Programme IMDYNHE.

References

1. A. Scheidemann, J.P. Toennies, J.A. Northby, *Phys. Rev. Lett.* **64**, 1899 (1990)
2. J.P. Toennies, A.F. Vilesov, *Angew. Chem. Phys.* **43**, 2622 (2004)
3. J. Harms, J.P. Toennies, F. Dalfovo, *Phys. Rev. B* **58**, 3341 (1998)
4. J. Harms, J.P. Toennies, M. Barranco, M. Pi, *Phys. Rev. B* **63**, 184513 (2001)
5. E. Krotscheck, R.E. Zillich, *Eur. Phys. J. D* **43**, 113 (2007)
6. E. Krotscheck, R.E. Zillich, *Phys. Rev. B* **77**, 094507 (2008)
7. D. Eichenauer, A. Scheidemann, J.P. Toennies, *Z. Phys. D* **8**, 295 (1988)
8. A. Leal, D. Mateo, A. Hernando, M. Pi, M. Barranco, *Phys. Chem. Chem. Phys.* **16**, 23206 (2014)
9. A. Vilà, M. González, R. Mayol, *Phys. Chem. Chem. Phys.* **18**, 2006 (2016)
10. L.F. Gomez et al., *Science* **345**, 906 (2014)
11. C.F. Jones et al., *Phys. Rev. B* **93**, 180510(R) (2016)
12. F. Ancilotto, M. Pi, M. Barranco, *Phys. Rev. B* **90**, 174512 (2014)
13. F. Ancilotto, M. Pi, M. Barranco, *Phys. Rev. B* **91**, 100503(R) (2015)
14. F. Ancilotto, M. Barranco, F. Caupin, R. Mayol, M. Pi, *Phys. Rev. B* **72**, 214522 (2005)
15. K.T. Tang, J.P. Toennies, *Z. Phys. D* **1**, 91 (1986)
16. L.F. Gomez, E. Loginov, R. Sliter, A.F. Vilesov, *J. Chem. Phys.* **135**, 154201 (2011)
17. A. Leal, X. Zhang, M. Barranco, F. Cargnoni, A. Hernando, D. Mateo, M. Mella, M. Drabbels, M. Pi, *J. Chem. Phys.* **144**, 094302 (2016)
18. D. Mateo, A. Leal, A. Hernando, M. Barranco, M. Pi, F. Cargnoni, M. Mella, X. Zhang, M. Drabbels, *J. Chem. Phys.* **140**, 131101 (2014)

6.2 Capture by quantised vortices



Cite this: *Phys. Chem. Chem. Phys.*,
2017, **19**, 24805

Capture of Xe and Ar atoms by quantized vortices in ^4He nanodroplets†

François Coppens,^{ID *ab} Francesco Ancilotto,^{cd} Manuel Barranco,^{abef} Nadine Halberstadt^{ab} and Martí Pi^{ef}

We present a computational study, based on time-dependent Density Functional theory, of the real-time interaction and trapping of Ar and Xe atoms in superfluid ^4He nanodroplets either pure or hosting quantized vortex lines. We investigate the phase-space trajectories of the impurities for different initial conditions and describe in detail the complex dynamics of the droplets during the capture of the impurities. We show that the interaction of the incoming atom with the vortex core induces large bending and twisting excitations of the vortex core lines, including the generation of helical Kelvin waves propagating along the vortex core. We have also calculated the stationary configurations of a ^4He droplet hosting a 6-vortex array whose cores are filled with Ar atoms. As observed in recent experiments, we find that doping adds substantial rigidity to the system, such that the doped vortex array remains stable, even at low values of the angular velocities where the undoped vortices would otherwise be pushed towards the droplet surface and be expelled.

Received 17th May 2017,
Accepted 11th July 2017

DOI: 10.1039/c7cp03307a

rsc.li/pccp

1 Introduction

It is well established that helium droplets can readily capture in their interior almost any atom or molecule interacting with them, as first shown for the case of Ne atoms,¹ with the notable exception of alkali² and some alkaline-earth³ atoms. This property, together with the extremely low temperature (T) achieved in helium droplets – of the order of 0.4 K – makes them the perfect ultracold and inert environment for hosting and studying isolated atoms and molecules, which is at the basis of current applications of helium droplets for spectroscopic studies of atoms and molecules. Besides, the superfluid nature of helium facilitates binary encounters of atoms/molecules in the bulk of the droplet while absorbing the energy released upon recombination, making possible chemical reactions which would not otherwise occur in the gas phase. These unique properties of helium droplets have had a huge impact on their study.^{4–8}

The pickup of Ar, Kr and Xe atoms in the gas phase by $^4\text{He}_N$ droplets with $N > 10^3$ atoms produced by nozzle beam expansions was described about twenty years ago by Toennies and coworkers.⁹ In these experiments, the droplets in the helium beam were deflected by impacting with a secondary beam made of rare gas atoms.

Recently, a technique has been introduced to determine the size of large He droplets ($N > 10^5$). It is based on the attenuation of a continuous droplet beam through collisions with Ar atoms at room temperature.¹⁰ The pickup chamber of the droplet beam apparatus is filled with argon gas and the helium droplets experience multiple, isotropic collisions with the Ar atoms on their way towards the detection chamber. Large helium droplets could also be doped in this way. This method, using Xe atoms, has been instrumental for detecting and imaging quantized vortex arrays in helium droplets.^{11,12} Xe atoms were used in these experiments because of their large sensitivity to the X-ray coherent diffractive imaging employed to detect them within the helium droplets. Experiments with large superfluid helium droplets are reviewed in a recent publication.¹⁴

The impurity–droplet interaction in the presence of vortices is also relevant as the first stage of a more complex process leading to the formation of nanowires, see *e.g.* ref. 15–18. Long filaments made of micrometer-sized solid hydrogen particles trapped on quantized vortex cores were used to directly image the vortex reconnection between quantized vortices in superfluid helium.¹⁹

The impact and capture of impurities interacting with pure helium droplets have been addressed recently within time-dependent density functional theory (TDDFT). Real-time simulations

^aUniversité de Toulouse, UPS, Laboratoire Collisions Agrégats Réactivité, IRSAMC, F-31062 Toulouse, France. E-mail: francois.coppens@irsamc.ups-tlse.fr

^bCNRS, UMR 5589, F-31062 Toulouse, France

^cDipartimento di Fisica e Astronomia ‘Galileo Galilei’ and CNISM, Università di Padova, via Marzolo 8, 35122 Padova, Italy

^dCNR-IOM Democritos, via Bonomea 265, 34136 Trieste, Italy

^eFacultat de Física, Departament FQA, Universitat de Barcelona, Diagonal 645, 08028 Barcelona, Spain

^fInstitute of Nanoscience and Nanotechnology (IN2UB), Universitat de Barcelona, Barcelona, Spain

† Electronic supplementary information (ESI) available. See DOI: 10.1039/c7cp03307a

have been carried out for heliophobic²⁰ (Cs) and heliophilic²¹ (Ne) atoms. In addition to the TDDFT equation for ^4He , heavy impurities are treated as classical particles using Newton's equation of motion, whereas a time-dependent Schrödinger equation has been used in the case of light impurities within the mean field model.^{21,22} A comparison between the results for head-on collisions of Cs and Xe atoms – heliophobic and heliophilic atoms of similar mass – has been presented in ref. 23.

In this work, we present the results obtained within TDDFT for the collision and capture of Xe and Ar atoms by a $^4\text{He}_{1000}$ droplet at different kinetic energies and impact parameters. Special attention is paid to the time-dependent interaction of Xe and Ar atoms with helium nanodroplets hosting vortex lines, and to the effect of multiply-doped vortex arrays in large helium droplets.

Due to the heavy computational cost of the TDDFT simulations presented here, we address only a few facets of the capture process that we consider of experimental relevance rather than carrying out a systematic study of the process. In particular:

- We study the capture of Xe atoms by a ^4He nanodroplet, both for head-on collisions and for different impact parameters, with velocities ranging from thermal values up to several hundred m s^{-1} . The results of peripheral collisions with different values of the impact parameter are used to estimate the cross section for the Xe capture.

- We study how a Xe atom dynamically interacts with a droplet hosting a vortex line, under different initial conditions resulting in different velocity regimes of the impurity as it collides with the vortex core: (i) a Xe atom initially at rest on the droplet surface and sinking under the effect of solvation forces; and (ii) a head-on collision of a moving Xe or Ar atom against the ^4He nanodroplet.

- We study the stationary state of a large $^4\text{He}_{15000}$ droplet hosting a ring of six vortex lines, doped with Ar atoms completely filling all six vortex cores. This is the simplest system that mimics those experimentally described in ref. 11, where doped vortex arrays embedded in rotating ^4He microdroplets have been imaged.

Multimedia materials accompany this paper, showing the real-time dynamics of several impact/capture processes described here. These materials are presented in the ESI† document. They constitute an important part of this work, since often it is only by viewing how a complex microscopic process unfolds in real time that one can catch important physical details which would otherwise escape in a written account.

2 Theoretical approach

The DFT model of liquid helium, which describes the nuclear degrees of freedom quantum mechanically, has emerged as the only viable method to address the experimentally studied large helium droplets. Its use constitutes a compromise between the accuracy of “*ab initio*” methods (like quantum Monte Carlo methods²⁴) and numerical feasibility.²⁵ Its essential features are recalled here for the sake of completeness.

Within DFT, the total energy E of a $^4\text{He}_N$ droplet at zero temperature is written as a functional of the ^4He atom density $\rho(\mathbf{r})$

$$E[\rho] = T[\rho] + \int d\mathbf{r} \mathcal{E}_c[\rho] \quad (1)$$

where $T[\rho]$ is the kinetic energy of a fictitious system of non-interacting particles (with mass m_4) constituting a BEC in the present case.

As in recent applications of the TDDFT approach,^{23,26–30} we use the correlation energy density functional \mathcal{E}_c proposed in ref. 31. This functional has a finite range and includes non-local effects. Both aspects are needed to describe the response of the liquid at the Ångström-scale. Note that a zero-range density functional has been recently applied to the study of inelastic scattering of xenon atoms by quantized vortices in superfluid liquid ^4He .³² Particle-vortex collisions in thermal superfluid ^4He have also been addressed.³³

It is customary to define an order parameter Ψ (often called the effective wave function) as $\Psi(\mathbf{r}) = \sqrt{\rho(\mathbf{r})}$. The kinetic energy of the fictitious system of non-interacting particles is thus

$$T[\rho] = \frac{\hbar^2}{2m_4} \int d\mathbf{r} |\nabla \Psi|^2 \quad (2)$$

Extension to time-dependent systems leads to the following time-dependent equation

$$i\hbar \frac{\partial}{\partial t} \Psi(\mathbf{r}, t) = \left\{ -\frac{\hbar^2}{2m_4} \nabla^2 + \frac{\delta \mathcal{E}_c}{\delta \rho} \right\} \Psi(\mathbf{r}, t) \equiv \mathcal{H}[\rho] \Psi(\mathbf{r}, t) \quad (3)$$

whose self-consistent solution provides the system density $\rho(\mathbf{r}, t) = |\Psi(\mathbf{r}, t)|^2$ and hence its total energy E . If the effective wave function is written as $\Psi(\mathbf{r}, t) = \Phi(\mathbf{r}, t) \exp[i\mathcal{S}(\mathbf{r}, t)]$, the particle current density is

$$\begin{aligned} \mathbf{j}(\mathbf{r}, t) &= -\frac{i\hbar}{2m_4} [\Psi^*(\mathbf{r}, t) \nabla \Psi(\mathbf{r}, t) - \Psi(\mathbf{r}, t) \nabla \Psi^*(\mathbf{r}, t)] \\ &= \frac{\hbar}{m_4} \rho(\mathbf{r}, t) \nabla \mathcal{S}(\mathbf{r}, t) \end{aligned} \quad (4)$$

with $\rho(\mathbf{r}, t) = |\Psi(\mathbf{r}, t)|^2 = \Phi^2(\mathbf{r}, t)$. This allows identifying the velocity field

$$\mathbf{v}(\mathbf{r}, t) = \frac{\hbar}{m_4} \nabla \mathcal{S}(\mathbf{r}, t)$$

that fulfills

$$\nabla \times \mathbf{v}(\mathbf{r}, t) = \frac{\hbar}{m_4} \nabla \times \nabla \mathcal{S}(\mathbf{r}, t) = 0$$

but in general

$$\nabla \cdot \mathbf{v}(\mathbf{r}, t) = \frac{\hbar}{m_4} \nabla \cdot \nabla \mathcal{S}(\mathbf{r}, t) = \frac{\hbar}{m_4} \Delta \mathcal{S}(\mathbf{r}, t) \neq 0$$

Thus, in the zero temperature DFT approach, liquid helium flows irrotationally. Liquid helium is compressible, a property that – at variance with simpler approaches – is taken into account in the DFT method.

In the case of stationary states, $\Psi(\mathbf{r}, t) = \Psi_0(\mathbf{r})e^{i\mu_4 t/\hbar}$ and eqn (3) becomes

$$\left\{ -\frac{\hbar^2}{2m_4} \nabla^2 + \frac{\delta\mathcal{E}_c}{\delta\rho} \right\} \Psi_0(\mathbf{r}) = \mu_4 \Psi_0(\mathbf{r}) \quad (5)$$

where μ_4 is the ${}^4\text{He}$ chemical potential.

The effect of heavy impurities like Ar and Xe atoms embedded inside He droplets is incorporated as an external field. The impurity-droplet interaction is described within the pairwise sum approximation

$$E[\rho] \rightarrow E[\rho] + \int d\mathbf{r} \rho(\mathbf{r}) V_X(|\mathbf{r} - \mathbf{r}_i|), \quad (6)$$

with V_X being the He-rare gas interaction potential from ref. 34 and \mathbf{r}_i the location of the impurity. The helium density is obtained by solving the Euler-Lagrange (EL) equation

$$\left\{ -\frac{\hbar^2}{2m_4} \nabla^2 + \frac{\delta\mathcal{E}_c}{\delta\rho} + V_X(|\mathbf{r} - \mathbf{r}_i|) \right\} \Psi_0(\mathbf{r}) = \mu_4 \Psi_0(\mathbf{r}) \quad (7)$$

This static DFT equation is solved by the imaginary time method in Cartesian coordinates. The calculation is full 3D with no *a priori* imposed symmetry. A key tool for the implementation of the method is the use of fast-Fourier techniques (FFT)³⁵ to calculate the convolutions needed to obtain some of the contributions to the total energy of the impurity-droplet complex and the mean field potentials appearing in the EL equations. Densities, wave functions and differential operators are discretized on a Cartesian grid. The spatial grid intervals most often used in the applications are in the 0.3–0.4 Å range. The differential operators (first and second derivatives) are represented by 13-point formulas.

Once the static configuration has been obtained for a given impurity, the dynamics starts by imparting a velocity v_0 to the impurity, initially placed at a chosen location \mathbf{r}_{i_0} . $\Psi(\mathbf{r}, t)$ is thus evolved following the TDDFT prescription and $\mathbf{r}_i(t)$ according to Newton's equation of motion:

$$i\hbar \frac{\partial}{\partial t} \Psi(\mathbf{r}, t) = \left[-\frac{\hbar^2}{2m_4} \nabla^2 + \frac{\delta\mathcal{E}_c}{\delta\rho} + V_X(|\mathbf{r} - \mathbf{r}_i|) \right] \Psi(\mathbf{r}, t) \quad (8)$$

$$m_i \ddot{\mathbf{r}}_i = - \int d\mathbf{r} V_X(|\mathbf{r} - \mathbf{r}_i|) \nabla \rho(\mathbf{r}, t).$$

Eqn (8) are solved using Hamming's predictor-modifier-corrector method³⁶ using the same box and grid as for the static problem. In most cases, we have employed a time step of ~ 0.5 fs. Hamming's method is not self-starting and requires the evaluation of the solution for a few initial time steps. They were obtained using a fourth-order Runge-Kutta-Gill algorithm.³⁶

During the time evolution, some helium can be ejected off the droplet, eventually reaching the boundaries of the cell used in the simulations. If no action is taken, this material will re-enter the simulation cell from the other side (periodic boundary conditions are implied in our calculations due to the use of FFT), therefore spoiling the calculation. We have handled this problem by including an absorption potential into the time-dependent equation for helium.³⁷ Note that this

particle – and thus energy – leaking is physical: it represents helium atoms leaving the droplet and carrying away energy, although in a continuous way inherent to the DFT approach.

3 Results

The results presented in this work have been obtained using the 4He-DFT BCN-TLS computing package.³⁸

3.1 Xe capture by vortex-free droplets

We have simulated head-on collisions of a Xe atom with a ${}^4\text{He}_{1000}$ droplet at relative velocities v_0 ranging from 200 to 600 m s⁻¹. Fig. 1 displays the two-dimensional plots of the helium density for the highest value, $v_0 = 600$ m s⁻¹. This velocity is well above the range of velocities typically encountered in experiments.^{10–12} In spite of the appearance of disconnected helium density shown in the $t = 87$ ps frame, we have found that the Xe atom eventually turns around and is captured again inside the droplet even at that relatively high impact velocity. Note that the Xe impurity, even when it temporarily emerges from the bulk of the droplet, appears to be coated with a few ${}^4\text{He}$ atoms, see the configuration at 87 ps.

Fig. 1 also shows the development of bow waves in the density profile, moving ahead of the impurity at supersonic velocity, and an incipient conic density wave front with its vertex at the Xe bubble. Similar conic shapes, characteristic of

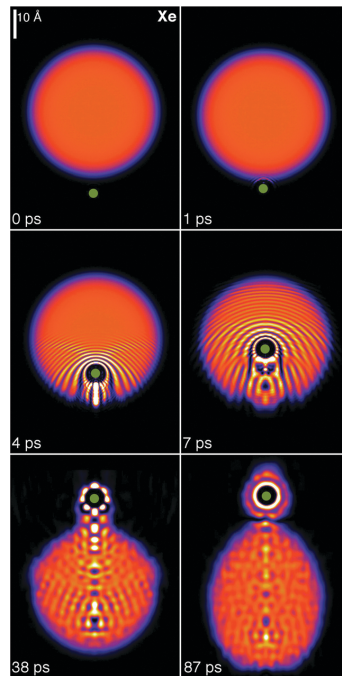


Fig. 1 Dynamic evolution of a Xe atom (green dot) approaching the ${}^4\text{He}_{1000}$ droplet from below at $v_0 = 600$ m s⁻¹. The corresponding time is indicated in each frame. Bright spots correspond to high density regions.³⁹

supersonic flows, are found when an impurity moves in bulk liquid helium. In the present case, the limited size of the droplet and the loss of kinetic energy during the first stages of the collision smooth out this front, making it just barely visible in the figure.

At low initial velocities of the impurity, we find that Xe moves back and forth inside the droplet. The turning points are not fixed, because the droplet deforms due to the displacement of the Xe atom and to the waves that are continuously emitted by the moving impurity (mainly in the direction of its motion), hit the droplet surface, and are reflected back inside it.²³ This is shown in Fig. 2 at $v_0 = 200$ and 300 m s^{-1} . Thermal Xe atoms ($v_0 \sim 240 \text{ m s}^{-1}$) are used in the vortex imaging experiments,^{11,12} and the average droplet velocity as it travels through the pick-up chamber is about 170 m s^{-1} ,¹⁰ corresponding to relative collision velocities which are within the range investigated here. The kinetic energy gained by the Xe atom after the turning point at 140–150 ps is precisely due to the fact that the droplet is not a rigid object and reacts to the motion of the impurity. As a consequence, energy is transferred not only from the impurity to the droplet but also the other way around. We want to emphasize that the droplet experiences large deformations rather than large displacements; the velocity of the center of mass (COM) of the droplet is rather small (below 6 m s^{-1} for $v_0 = 200$ and 300 m s^{-1} as well) due to the large mass difference between the impurity and the droplet.

We have found that most of the energy is transferred from the Xe atom to the droplet in the first stages of the collision. This is why, for collisions in this kinetic energy range leading to Xe capture, the motion of the impurity inside the droplet is independent of the initial kinetic energy to a large extent. This is shown in Fig. 3, which displays the trajectory of Xe (Ar) in phase space for $v_0 = 200$ (360 m s^{-1}). The figure also shows similar trajectories in the case where a vortex is present in the droplet; these cases will be discussed later in this paper.

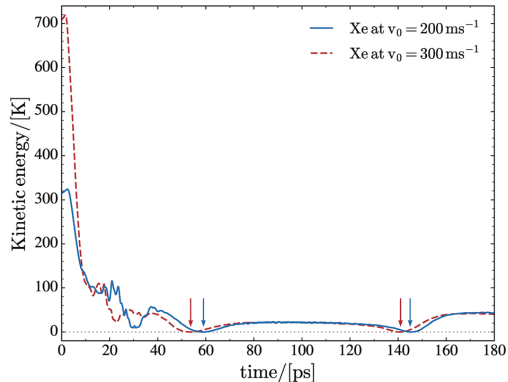


Fig. 2 Kinetic energy of the Xe atom in the center of mass (COM) frame of the ${}^4\text{He}_{1000}$ droplet as a function of time for a head-on collision at $v_0 = 200$ and 300 m s^{-1} . The kinetic energy increase during the first few picoseconds is due to the acceleration produced by the attractive part of the Xe-He potential. The vertical arrows indicate the first two turning points inside the droplet.

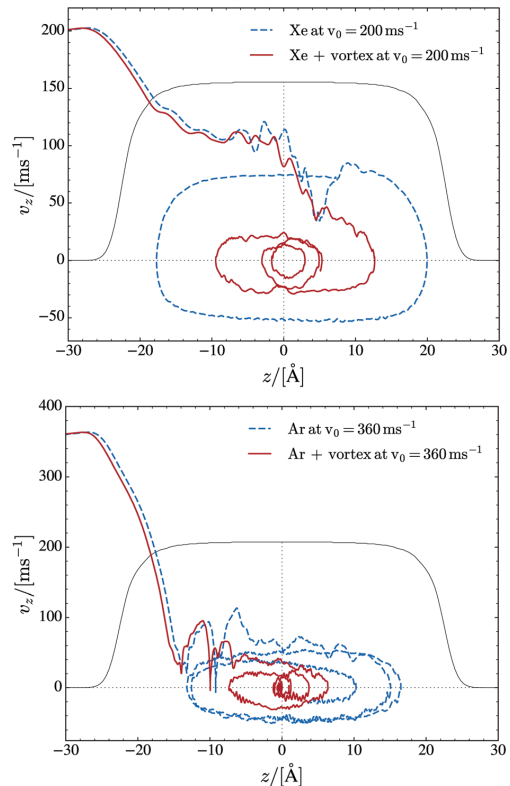


Fig. 3 (Top) Phase-space trajectory of Xe for a head-on collision at $v_0 = 200 \text{ m s}^{-1}$ against a ${}^4\text{He}_{1000}$ droplet with and without a vortex line. The Xe atom is referred to the COM frame of the droplet. (Bottom) Same as the top panel for Ar at $v_0 = 360 \text{ m s}^{-1}$. The droplet density at $t = 0$ is also represented on an arbitrary scale (black profile).

The kinetic energy lost by the impurity atom is partly deposited in the droplet, where it produces large deformations and sound waves, and partly carried away by prompt-emitted helium atoms. These are atoms with a significant kinetic energy which are expelled from the droplet early on in the collision process. Fig. 4 shows the number of atoms remaining in the simulation cell as a function of time for collisions with Xe at $v_0 = 200$, 300 and 400 m s^{-1} . Eventually, the energy deposited into the droplet should be lost by atom evaporation. The energy carried away by the ejected He atoms during the first 200 ps is collected in Table 1 for the head-on collisions described in this paper. For comparison, the calculated binding energy of a helium atom in the ${}^4\text{He}_{1000}$ droplet is 6.0 K. Note that helium atom ejection continues after 200 ps, with the droplet still being far from “thermalized” (equilibrated).

In the case of heavy dopants, it is possible to obtain a simple expression for their capture cross section. Defining

$$\kappa = \sqrt{\frac{2\mu E}{\hbar^2}}, \quad (9)$$

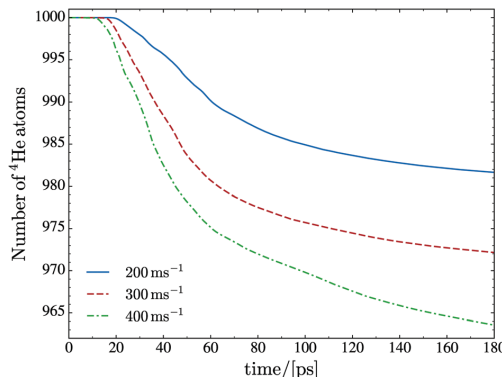


Fig. 4 Number of He atoms remaining in the droplet as a function of time for the Xe against ${}^4\text{He}_{1000}$ collision at $v_0 = 200, 300$ and 400 m s^{-1} .

Table 1 Number of He atoms promptly ejected (N_e) and average energy per ejected atom (E_e) during the first 200 ps

Species	$v_0 (\text{m s}^{-1})$	N_e	$E_e (\text{K})$
Xe	200	18	19
	300	28	23
	400	37	30
Ar	360	16	22

where μ is the reduced mass of the system and E is the available energy in the center-of-mass frame, and provided that the reduced de Broglie wave length of the impurity $\lambda/(2\pi) = 1/\kappa$ is much smaller than the dimensions of the droplet (which is the case for all v_0 in this study), the system behaves classically and²⁰

$$\sigma(E) = \frac{\pi}{\kappa^2} \sum_{\ell=0}^{\ell_{\text{cr}}} (2\ell + 1) = \frac{\pi}{\kappa^2} (\ell_{\text{cr}} + 1)^2 \quad (10)$$

where ℓ_{cr} is the largest relative angular momentum leading to the impurity capture. For a given energy, ℓ_{cr} is determined by carrying out simulations with different impact parameters b using $\ell = \mu v_0 b / \hbar$. We have done it for Xe at $v_0 = 200 \text{ m s}^{-1}$. Fig. 5 shows the simulation corresponding to the largest impact parameter among the ones we have calculated which led to Xe capture, $b = 20.3 \text{ \AA}$, and Fig. 6 shows the simulation corresponding to the smallest one which led to Xe deflection, $b = 22.2 \text{ \AA}$. The radius of the droplet, which is defined as $R = r_0 N^{1/3}$ with $r_0 = 2.22 \text{ \AA}$, is 22.2 \AA for $N = 1000$. Hence, at this energy – well within the thermal conditions of the experiment – the cross section for Xe capture is very similar to the geometric droplet cross section.

The circulation lines of the superflow are displayed in two selected panels in Fig. 5 and 6. They show the flow pointing towards the approaching Xe atom at the beginning of the collision and the appearance of vortex loops in the droplet at the latest stages of the simulation. Vortex loops appear from local distortions of the droplet surface.²⁸ The circulation lines displayed in the figures of this work have been drawn inside the

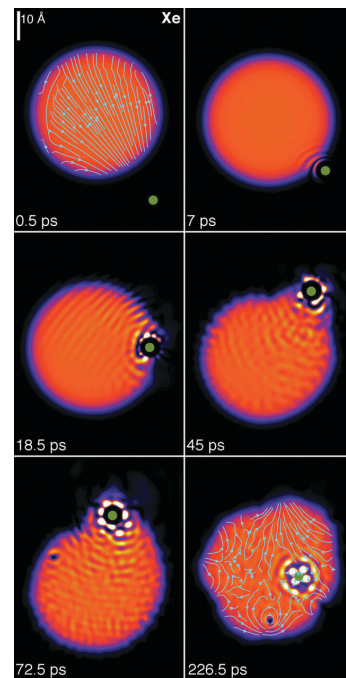


Fig. 5 Dynamic evolution of a Xe atom (green dot) approaching the ${}^4\text{He}_{1000}$ droplet from below at $v_0 = 200 \text{ m s}^{-1}$ with impact parameter $b = 20.3 \text{ \AA}$. The corresponding time is indicated in each frame.³⁹

region where the density is above $0.5\rho_0$ (with $\rho_0 = 0.0218 \text{ \AA}^{-3}$), which defines the dividing surface of the droplet.

In peripheral collisions, not only energy but also angular momentum is deposited into the droplet, which allows visualizing the irrotational flow of the superfluid helium. In particular, for Xe at $v_0 = 200 \text{ m s}^{-1}$ and $b = 22.2 \text{ \AA}$ the initial angular momentum is $917\hbar$. This collision was followed for some 220 ps and produced the ejection of 15 He atoms, 5 of them attached to the Xe atom, see Fig. 6. After the collision, the Xe + ${}^4\text{He}_5$ complex carries away 522 angular momentum units, while some 95 units are deposited in the droplet as vortex loops and capillary waves,⁴⁰ see the bottom right panel of Fig. 5 and 6. The remaining angular momentum is taken away by the ejected helium atoms.

3.2 Helium droplets hosting vortex lines

To determine the structure of a droplet hosting a singly-quantized linear vortex, we have started the imaginary time iteration from a helium density in which the vortex is “imprinted”. For this purpose, a vortex line along the z axis can be described by the effective wave function

$$\Psi_0(\mathbf{r}) = \rho_0^{1/2}(\mathbf{r}) e^{i\mathcal{S}(\mathbf{r})} = \rho_0^{1/2}(\mathbf{r}) \frac{(x + iy)}{\sqrt{x^2 + y^2}} \quad (11)$$

where $\rho_0(\mathbf{r})$ is the density of either the pure or the impurity-doped droplet without a vortex. Vortex lines along other directions passing through a chosen point can be imprinted as well.⁴¹

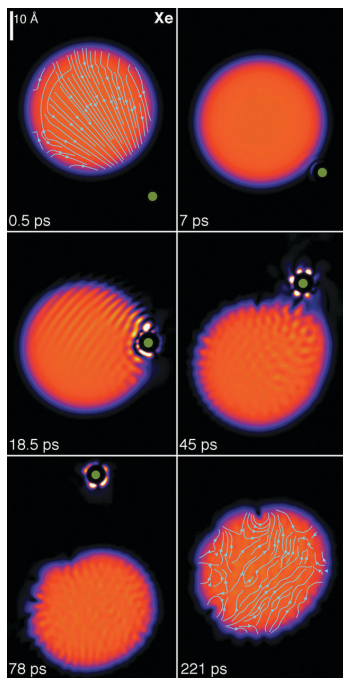


Fig. 6 Dynamic evolution of a Xe atom (green dot) approaching the ${}^4\text{He}_{1000}$ droplet from below at $v_0 = 200 \text{ m s}^{-1}$ with impact parameter $b = 22.2 \text{ \AA}$. The corresponding time is indicated in each frame.³⁹

In the case represented by eqn (11), if the impurity is within the vortex core along a symmetry axis of the impurity–droplet complex, the effective wave function $\Psi_0(\mathbf{r})$ – before and after relaxation – is an eigenvector of the angular momentum operator $\hat{L}_z = -i\hbar\partial/\partial\theta$. The angular momentum of the droplet is then

$$\langle \hat{L}_z \rangle = \langle \Psi_0(\mathbf{r}) | \hat{L}_z | \Psi_0(\mathbf{r}) \rangle = N\hbar \quad (12)$$

Different energy balances involving pure and doped droplets hosting vortices are defined:^{41–43}

- Solvation energy of the impurity:

$$S_X = E(X@{}^4\text{He}_N) - E({}^4\text{He}_N)$$

- Vortex energy:

$$E_V = E(V@{}^4\text{He}_N) - E({}^4\text{He}_N)$$

- Binding energy of the impurity to the vortex:

$$B_X = S_X - \{E[(X + V)@{}^4\text{He}_N] - E(V@{}^4\text{He}_N)\}$$

Using the functional of ref. 31 and the He–rare gas pair potentials of ref. 34, solvation energies of -316.3 K and -215.7 K have been found for Xe and Ar atoms, respectively. Thus, for the same incident kinetic energy, about 100 K of

additional energy have to be dissipated in the case of Xe in order to obtain the same kinematic conditions as for Ar.

The binding energy of the impurity to the vortex is the result of a delicate balance between terms which are individually much larger than their difference. It can thus be affected by relatively large inaccuracies. Within DFT, it has been found that the Xe atom is barely bound to the vortex line, with $B_{\text{Xe}} \sim 3–5 \text{ K}$.^{43,44}

A critical angular velocity ω_c exists above which nucleation of vortices with quantized velocity circulation in units of h/m_A occurs. The critical angular velocity for nucleating a vortex line along a diameter in a droplet made of N helium atoms is

$$\omega_c = \frac{1}{\hbar} \frac{E_V}{N} \quad (13)$$

This expression is obtained by computing the energy that minimizes $\langle H - \omega L_z \rangle$ (*i.e.* corresponding to the equilibrium configuration in the co-rotating frame) with and without a vortex line. Using the values appropriate for a ${}^4\text{He}_{1000}$ droplet we obtain $\omega_c = 0.127 \text{ K}/\hbar = 0.0167 \text{ ps}^{-1}$.

When the angular velocity is increased above ω_c , larger amounts of angular momentum may be stored into the superfluid by increasing the number of nucleated vortices. The higher the angular velocity, the more packed the vortex array around the rotation axis. These vortices arrange themselves into ordered structures whose existence in bulk superfluid ${}^4\text{He}$ was established long ago.^{45,46}

To generate vortex arrays, we have worked in the fixed-droplet frame of reference (co-rotating frame at angular velocity ω), *i.e.* we look for solutions of the following EL equation:

$$\{\mathcal{H}[\rho] - \omega \hat{L}_z\} \Psi(\mathbf{r}) = \mu_4 \Psi(\mathbf{r}), \quad (14)$$

In this case, $\Psi(\mathbf{r})$ no longer is an eigenvector of the angular momentum. To determine $\Psi(\mathbf{r})$ describing a configuration where n_v vortex lines are present we have followed again the imprinting strategy, starting the imaginary-time evolution of eqn (14) with the helium effective wave function

$$\Psi_0(\mathbf{r}) = \rho_0^{1/2}(\mathbf{r}) \prod_{j=1}^{n_v} \left[\frac{(x - x_j) + i(y - y_j)}{\sqrt{(x - x_j)^2 + (y - y_j)^2}} \right] \quad (15)$$

where $\rho_0(\mathbf{r})$ is the density of the vortex-free droplet and (x_j, y_j) is the initial position of the j -vortex linear core with respect to the z -axis of the droplet (note that in ref. 42 and 44 $\Psi_0(\mathbf{r})$ was incorrectly written). We underline the fact that during the functional minimization of the total energy, the vortex positions and shapes will change to provide at convergence the lowest energy vortex configuration for the given value of the angular velocity ω .

Fig. 7 shows the two-vortex stationary configuration of a ${}^4\text{He}_{1000}$ droplet in the co-rotating frame at angular frequency $\omega = 0.175 \text{ K}/\hbar = 0.0229 \text{ ps}^{-1}$. The angular momentum of this configuration is $\langle \hat{L}_z \rangle = 1836\hbar$. Note the bending of the vortex line so that they meet the droplet surface perpendicularly at both ends, and also the flattening of the droplet in the z direction due to centrifugal forces.

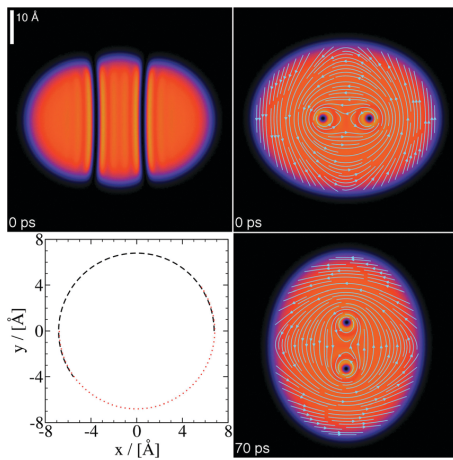


Fig. 7 ${}^4\text{He}_{1000}$ droplet at $\omega = 0.0229 \text{ ps}^{-1}$. Top panels, stationary two-vortex configuration in the x - z plane (left) and x - y plane (right) in the co-rotating frame. Bottom left panel, trajectory of the vortex cores in the x - y plane of the laboratory frame. The dashed line is the trajectory of one of the vortex cores, and the dotted line that of the other. Both trajectories overlap for a rigid rotation of the cores. Bottom right panel, helium density in the x - y plane at $t = 70 \text{ ps}$ obtained in the laboratory frame starting from the above configuration.³⁹

At variance with the single vortex line along the symmetry axis of the droplet, the two-vortex configuration is not stationary in the laboratory frame, where the density and velocity field change with time. To show this, $\Psi(\mathbf{r})$ has been evolved in the laboratory for about 150 ps taking as an initial condition the stationary configuration in the co-rotating frame. As expected, the vortex cores appear to rotate in the laboratory frame. Within the numerical accuracy, they do so rigidly. This can be seen in Fig. 7. Besides, they rotate precisely at $\omega = 0.0229 \text{ ps}^{-1}$. This is a stringent test of the accuracy of the dynamics and the consistency of the method. It can be seen in the ESI† material how the two vortex lines turn around each other.

Fig. 7 shows how a superfluid droplet hosting a vortex array “rotates”. The fact that the vortex cores rotate rigidly is not in contradiction with the irrotational character of the superfluid flow, since they are empty. The cores carry along with them the superfluid whose velocity field is irrotational, whereas for a rigid solid or a classical liquid in steady flow one has $\mathbf{v} = \omega \times \mathbf{r}$, hence $\nabla \times \mathbf{v} = 2\omega$. The circulation lines in Fig. 7 do not correspond to a rigid rotation, but to an irrotational flow in the presence of two vortices. The helium density adapts to the vortex cores as they rotate and this gives the appearance of a solid rotation in the laboratory frame, but it is not.

It is worth discussing the different configurations that may appear when $\omega < \omega_c$. The lowest energy corresponds to the current-free (CF) $\langle L_z \rangle = 0$ configuration. Metastable one-vortex (1V) configurations with $\langle L_z \rangle = N\hbar$ also exist in this angular frequency range.^{42,44} Other irrotational (IR) configurations with $\langle L_z \rangle < N\hbar$ do exist, arising from velocity potentials such as, e.g., $\mathcal{S}(\mathbf{r}) = zxy$. For an ellipsoidal droplet with a sharp surface,

the parameter α is related to the angular velocity around the z -axis and the deformation of the ellipsoid, see the Appendix and ref. 47–49.

These IR configurations may be generated by using the phase $\mathcal{S}(\mathbf{r}) = zxy$ in eqn (11) and minimizing $\langle H - \omega \hat{L}_z \rangle$. At a given value of $\omega < \omega_c$, the energies in the co-rotating frame are ordered as $E_{\text{CF}} < E_{\text{IR}} < E_{\text{1V}}$. Fig. 8 shows the stationary configuration in the co-rotating frame corresponding to $\omega = 0.10 \text{ K}/\hbar = 0.0131 \text{ ps}^{-1}$. Although this angular frequency is close to ω_c , this configuration is hardly distorted and hosts a negligible amount of angular momentum: less than $5 \times 10^{-2}\hbar$, compared to the value of $10^3\hbar$ at ω_c . The circulation lines can be analytically calculated if the density profile is approximated by that of an ellipsoid with constant density, see the Appendix.

Figures similar to Fig. 8 are shown in ref. 47 and 48 for a rotating elliptic vessel filled with a fluid whose flow is irrotational. While in the case of a rigid solid or viscous liquid in steady flow the entire system rotates as a whole, an irrotationally flowing fluid in a rotating vessel is just pushed by the walls of the container; the same happens for a Bose–Einstein condensed gas in a rotating trap.⁴⁹ For an isolated self-bound ${}^4\text{He}$ droplet, the apparent “rotation” of the system in the laboratory arises from deformations of the fluid elements constituting the droplet, but not from their local rotation which is forbidden by the irrotational condition. The vorticity Ω [defined in hydrodynamics as⁵⁰ $\Omega = \nabla \times \mathbf{v}(\mathbf{r})$], initially distributed in the helium droplet when it is in the normal phase, concentrates in the vortex lines when the droplet becomes superfluid and its velocity field becomes irrotational.

The above discussion shows how difficult it is to set a superfluid droplet in rotation. Experimentally,^{11–13} the situation is different, since the helium droplet is initially in a normal phase state at a temperature above the normal-to-superfluid transition temperature T_λ (about 2.17 K in bulk liquid at 1 bar). As a consequence, it may store large amounts of angular momentum and experience large deformations. Copious evaporation drives

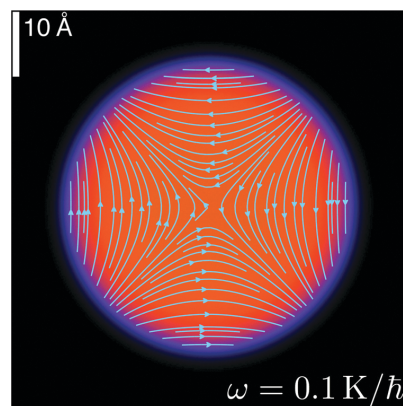


Fig. 8 Stationary configuration of the ${}^4\text{He}_{1000}$ droplet at $\omega = 0.10 \text{ K}/\hbar = 0.0131 \text{ ps}^{-1}$ in the co-rotating frame (x - y plane).

the droplet into a superfluid state at a temperature below T_c and the angular momentum remaining in the droplet is then stored in vortex arrays that are being nucleated.

3.3 Dynamics of Xe and Ar capture by vortex lines

To study the interaction of an atomic impurity with vortices, we have imprinted a vortex line in the ${}^4\text{He}_{1000}$ droplet and prepared the Xe atom under different kinematic conditions.

The inelastic scattering of xenon atoms by quantized vortices in superfluid bulk helium has been addressed in ref. 32. It was found that a head-on collision leads to the capture of Xe by the vortex line at $v_0 = 15.4 \text{ m s}^{-1}$, but not at $v_0 = 23.7 \text{ m s}^{-1}$. We have carried out an equivalent simulation by initially placing the Xe atom inside the droplet 10 Å away from the vortex line and sending it head-on towards the vortex at a velocity of 10 m s⁻¹. This velocity is of the order of the thermal velocity of a Xe atom in a droplet under experimental conditions, once the droplet has thermalized after capturing the Xe atom ($T \sim 0.4 \text{ K}$).⁴ Since the equilibrium position of the Xe atom is at the center of the droplet, it moves to this region and remains there during the rest of the simulation. In this region of the droplet, the Xe atom is also attracted by the vortex, but it is deflected by the superfluid flow around the vortex line and ends up orbiting around it. Hence, it is captured by the vortex without getting into its core.

A detailed analysis of the Xe capture as a function of the impact parameter has also been carried out in ref. 32, with the conclusion that when the impact parameter of the Xe atom approaching the vortex line is larger than about 5 Å, Xe is deflected but not captured.³² In the case of droplets, the final result is very different. Upon capture, the Xe atom wanders erratically inside the droplet, as we have seen in the case of vortex-free droplets. The surface of the droplet deforms dynamically and acts as a “pinball machine”, which eventually brings the Xe atom close enough to the vortex line if it missed it in the first attempt or was not previously ejected off the droplet.

The smoothest capture process one might think of corresponds to the Xe atom being initially placed at rest on the droplet surface, as no kinetic energy is given to the impurity. The Xe atom is accelerated towards the center of the droplet due to the attractive He-Xe interaction. We show that, under these kinematic conditions, some He atoms are first drawn towards the impurity because they are lighter, also see Fig. 9 and 10 in ref. 39. Eventually, the impurity with its “solvation structure” sinks, acquires some velocity, and is also deflected by the velocity field of the vortex line.

We have tried two different initial locations of the Xe atom on the droplet surface. One is a point on the equator of the droplet, in a plane perpendicular to the vortex line; the other location is one of the open vortex core ends. Our aim was to see if a sensible difference in the transit time of Xe across the droplet could be detected. The simulations do not show important differences between the time taken by the impurity to reach the center of the droplet. It is about 20% larger when Xe starts from the equator than from the core end.³⁹ It is worth noting that in the latter case the sliding of the impurity along

the core proceeds rather smoothly, and that the impurity oscillates back and forth much as in the vortex-free case.

The simulation of Xe ($v_0 = 200 \text{ m s}^{-1}$) and Ar ($v_0 = 360 \text{ m s}^{-1}$) atoms head-on colliding with a ${}^4\text{He}_{1000}$ droplet perpendicularly to the vortex line has been analyzed and compared with the results corresponding to a vortex-free droplet. The trajectory of the Xe and Ar atoms in phase space is shown Fig. 3. In both cases, the trajectory of the impurity is limited to the region of the droplet around the vortex line. The impurity orbits around the vortex line because the superfluid flow does so. Since in the DFT approach no dissipation is included, the signature of the capture of an impurity by a vortex is its close orbiting around the vortex line, as shown in the figure and especially in ref. 39. The ESI† material shows that while Ar is captured during its first transit across the droplet, the Xe atom is only captured in its second transit. We attribute this difference to the larger solvation energy of Xe (see Section 3.2), which requires more time to be dissipated. It can be seen³⁹ that when Xe detaches from the vortex in the first transit, the vortex line is reconnected near the atomic solvation structure because no open ends can remain in the bulk of the droplet.

Fig. 9 and 10 show that when the impurity hits the droplet surface, a series of surface and volume density waves are launched. These waves travel much faster than the impurity itself, which has lost a large amount of kinetic energy when it pierced the surface.

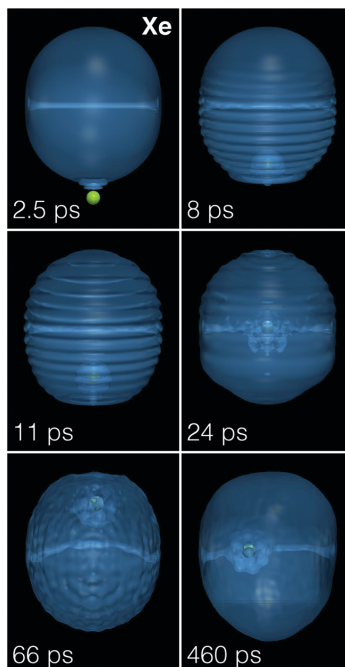


Fig. 9 Dynamic evolution of a Xe atom (green dot) approaching a ${}^4\text{He}_{1000}$ droplet hosting a vortex line from below at $v_0 = 200 \text{ m s}^{-1}$. The corresponding time is indicated in each frame.³⁹

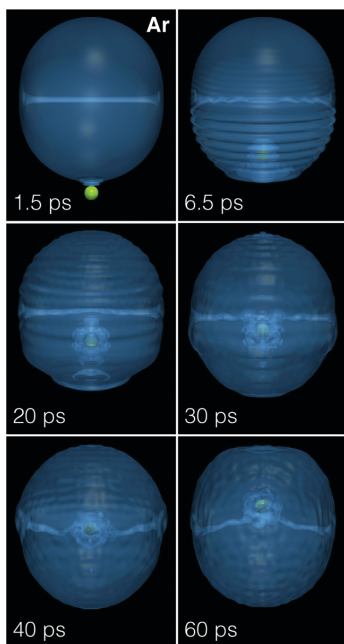


Fig. 10 Dynamic evolution of an Ar atom (green dot) approaching a ${}^4\text{He}_{1000}$ droplet hosting a vortex line from below at $v_0 = 360 \text{ m s}^{-1}$. The corresponding time is indicated in each frame.³⁹

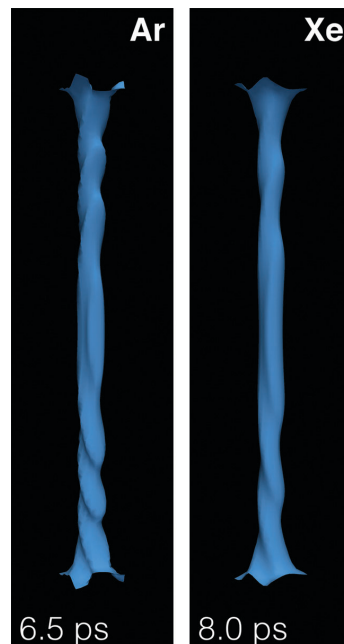


Fig. 11 Core structure of the vortex line in a ${}^4\text{He}_{1000}$ droplet after colliding with Xe at $v_0 = 200 \text{ m s}^{-1}$ (right panel, $t = 8 \text{ ps}$) and Ar at 360 m s^{-1} (left panel, $t = 6.5 \text{ ps}$). The full structure of the droplet is shown in Fig. 9 and 10.

The displacement of the atom in the droplet produces sound waves in the liquid and distortions along the vortex line (Kelvin modes). It is worth seeing that before bending by collision with the impurity, the vortex line is twisted (helical Kelvin mode). This is due to the interference between the spherical wave front flow produced by the hitting of the droplet surface, which travels from bottom to top, and the flow around the vortex core. The spherical wave front hits first the central portion of the vortex line, whose ends are anchored on the droplet surface. This yields the appearance of the helical distortion along the vortex line shown in Fig. 11. The twisting can no longer be followed after the impurity solvation structure reaches the vortex line, bending and dragging it along in the course of its orbiting around it. But it is clearly visible before as shown in Fig. 11, which displays the density of the droplet around the vortex line at the indicated collision time.

We have thus shown that Xe and Ar atoms are readily captured by vortex lines in helium droplets under conditions prevailing in the experiments.^{11,12} Simulating the capture of a huge number of impurities or clusters by vortex arrays in very large droplets is beyond reach at present. However, the results presented in this subsection are the proof of concept that the limitation is technical and not conceptual.

3.4 Vortex arrays in ${}^4\text{He}$ droplets doped with Ar atoms

The existence of ordered vortex lattices inside ${}^4\text{He}$ droplets has been established by the appearance of Bragg patterns from Xe

clusters trapped inside the vortex cores in droplets made of $N = 10^8\text{--}10^{11}$ atoms (corresponding to radii from 100 to 1000 nm).^{11,12} We have recently studied the stability of vortex arrays made of up to $n_v = 9$ vortices inside a ${}^4\text{He}$ nanodroplet using the DFT approach.⁴² It was found that the energetically favored structure for $n_v > 6$ is a ring of vortices encircling a vortex at the center of the droplet. For $n_v = 6$, the configuration with a six-vortex ring is found to have almost the same energy as the five-fold ring plus a vortex at the center. The former structure has been experimentally observed,^{11–13} although classical vortex theory predicts for it a much higher free energy cost than for the latter.⁵¹ Similar equilibrium structures have been obtained within DFT for helium nanocylinders hosting vortex arrays.⁴⁴

In the experiments of ref. 12, the diffraction images show that rotating ${}^4\text{He}$ nanodroplets of about 200 nm in diameter contain a small number of symmetrically arranged quantum vortices whose cores are filled with regularly spaced Xe atoms. Unexpected large distances of the vortices from the droplet center ($\sim 0.7\text{--}0.8$ droplet radii) are observed and explained as a result of the balance between the contribution of the Xe atoms to the total angular momentum of the droplets and the solvation potential of the embedded Xe atoms, which opposes the migration of vortices towards the droplet surface and their annihilation there, as it would happen instead in the case of undoped vortices at low values of the droplet rotational frequency.

In practice, as more and more Xe atoms become attached to a vortex, they adopt the angular velocity of its revolution about the droplet center. If the Xe capture is isotropic, the total angular momentum of the droplet is conserved, and thus the angular momentum accompanying the Xe rotational motion must be transferred from the vortices to the impurities. This reduction in the angular momentum of the vortices causes them to move outwards, resulting in the larger equilibrium distances of the vortices observed in the experiments. The actual equilibrium radial positions result from a balance between this tendency to move towards the droplet surface and the solvation potential, which tends instead to draw impurities towards the droplet center.

We have looked for stationary configurations of a 6-vortex ring in a rotating He_{15000} droplet by solving the EL equations in the co-rotating frame with a fixed angular velocity. Each vortex core is filled with Ar atoms, and the system is allowed to fully relax. In the end, the column of atoms inside each vortex core reaches an equilibrium structure where the Ar atoms are separated by a distance which is roughly that of the Ar dimer. One such configuration is shown in Fig. 12. Note that the vortex cores are almost straight lines, whereas in an undoped droplet rotating with the same velocity the vortex lines would be bent, as shown *e.g.* in Fig. 7. The Ar atoms are not shown in the figure. The localized structures appearing in the vortex cores are regions of highly inhomogeneous, high ^4He density resulting from the Ar-He attractive potential.

The presence of impurities thus confers rigidity to the vortex lines, preventing them from bending. Yet, the small segment of the vortex line free from impurities bends so as to hit the droplet surface perpendicularly, see the bottom panel of Fig. 12. Note that in the absence of vortices, Ar atoms initially placed in a linear chain structure would relax towards the lower energy, compact configuration of an Ar cluster in the bulk of the droplet. However, once trapped by a vortex core, their collapse into such a cluster structure does not occur, *i.e.* an energy barrier appears and prevents the formation of Ar clusters. Our simplified description of the more complex experimental conditions (where each vortex line hosts chains of regularly spaced atomic clusters, instead of chains of single atoms) is due to computational limitations.

Our choice of Ar instead of Xe as a dopant is motivated by the weaker He-Ar and Ar-Ar interactions, which facilitate the imaginary-time relaxation. The interaction of the helium environment with several close-by impurities increases the strength of dopant-droplet interaction, producing helium localization around the impurities (snowball structures), see Fig. 9. Stabilizing these structures is extremely time consuming, especially when the He-impurity interaction is strong. Experiments were also carried out with Ar atoms as dopants, but have not been analyzed yet.⁵² However, no significant difference is expected between argon and xenon, neither from the experimental nor from the theoretical viewpoint.

There are obvious differences in scales between our simulations and the actual experiments, due to computational cost. In experiments, heavier impurities are used (Xe), the droplets are much larger and doping is known to occur by filling the

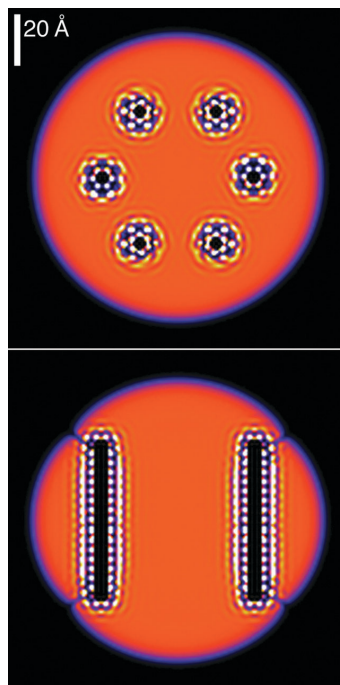


Fig. 12 Helium droplet configuration hosting six vortices, each doped with a line of regularly spaced Ar atoms (not represented). The top figure shows the density in the x-y symmetry plane (top view), while the bottom figure shows a side view corresponding to the y-z plane. As in some of the previous figures, the bright spots are high density blobs appearing around the impurity atoms.

vortex cores with a chain of equally spaced Xe clusters, each made of hundreds of atoms, instead of atom chains as done in our simulations. In spite of these differences, we find results which qualitatively explain the unusual behavior of vortex lines experimentally observed in doped rotating helium droplets.

We have looked for the equilibrium structure of the Ar@6-vortex $^4\text{He}_{15000}$ droplet for different imposed values of the angular velocity of rotation. The results show that doping inside each vortex core adds substantial stability to the system, such that doped vortices are still stable in a droplet rotating at rather low values of the angular velocities, whereas undoped vortices at such values would be pushed towards the surface of the droplet and eventually expelled. The solvation potential effect becomes apparent below some critical value of the angular velocity, where the vortices cease to move towards the surface and the system reaches an equilibrium maximum distance of the vortices from the droplet center. This is shown in Fig. 13, where we plot the radial distance of the vortices from the center as a function of the angular momentum of the system. Note how doped vortices are stable at values of the angular momentum well below the stability limit of an undoped droplet. A similar behavior has been observed in the experiment (see for instance Fig. 2 in the ESI† of ref. 12).

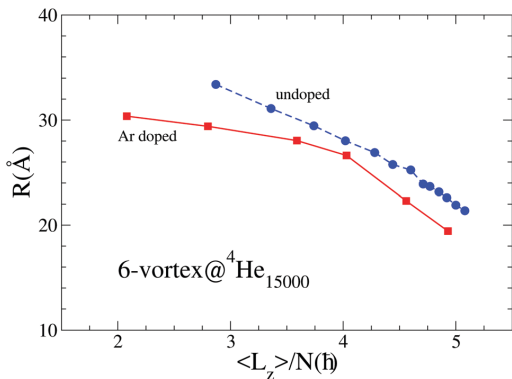


Fig. 13 Calculated equilibrium distance of the 6-vortex ring from the droplet center as a function of the angular momentum per He atom in units of \hbar . The dots represent the results for undoped vortices, while the squares are the results for Ar-doped vortices. The lines are drawn as a guide to the eye.

4 Summary and outlook

We have shown that Xe and Ar atoms at thermal velocities are readily captured by helium droplets, with a capture cross section similar to the geometric cross section of the droplet. Crucially for the subsequent capture of impurities by vortex lines, we have also shown that most of the kinetic energy of the impinging impurity is lost in the capture process during the first tens of picoseconds. This happens either by the ejection of prompt-emitted He atoms or by the production of sound waves and large deformations in the droplet.

If the droplet hosts a vortex, slowly moving impurities are readily captured by the vortex line. Rather than being trapped inside the vortex core, the impurity is bound to move at a close distance around it. Besides the crucial energy loss when the impurity hits the droplet, the capture by the vortex is favored by a further energy transfer from the impurity to the droplet: large amplitude displacements of the vortex line – as shown in the ESI† accompanying this work – take place, constituting another source of the kinetic energy loss in the final stages of the capture. A related issue is the appearance of Kelvin modes in the vortex line, that is not only bent, but also twisted in the course of the collision.

If the kinematic conditions of the collision (kinetic energy and impact parameter) lead to the capture of the impurity by the droplet, the pinball effect caused by the droplet surface can induce the meeting of the Xe/Ar atom and the vortex line – and the possible capture of the atom by the vortex –, since both have a tendency to remain in the inner region of the droplet. We have shown this in the case of Xe at $v_0 = 200 \text{ m s}^{-1}$: Xe is captured during its second transit across the droplet, whereas this could not have happened in bulk liquid helium.³²

The capabilities of the He-DFT approach might help elucidate processes of experimental interest, such as the capture of

one or several impurities by large droplets hosting a vortex array and how several atomic impurities, impinging upon a rotating droplet hosting vortices, react to form small clusters, eventually being trapped within the vortex cores as it appears in the experiments.

Appendix

In this Appendix, we discuss the relationship between the angular velocity and angular momentum of a deformed droplet below the critical angular frequency for vortex nucleation.

Let us consider an ellipsoidal vessel filled with liquid ^4He uniformly rotating around the z axis, $\omega = \omega \hat{\mathbf{k}}$. The ellipsoid has the equation

$$F(x, y, z) = \frac{x^2}{R_1^2} + \frac{y^2}{R_2^2} + \frac{z^2}{R_3^2} - 1 = 0$$

If \mathbf{v} is the irrotational velocity of a point in the laboratory, \mathbf{v}' the velocity of the same point in the vessel (co-rotating frame), and $\mathbf{V} = \omega \times \mathbf{r}$, one has

$$\mathbf{v}' = \mathbf{v} - \mathbf{V} = \frac{\hbar}{m_4} \nabla \mathcal{S} - \omega \times \mathbf{r}$$

where \mathcal{S} is the velocity potential defined here so that

$$\mathbf{v} = \frac{\hbar}{m_4} \nabla \mathcal{S}(x, y, z)$$

Its existence is granted by irrotationality; we also have $\mathbf{V} = \omega \times \mathbf{r} = \omega(-y, x, 0)$. A vector perpendicular to the ellipsoid surface is $\mathbf{n} = \nabla F(x, y, z)$. From the stationarity condition $(\mathbf{v}' \cdot \mathbf{n})|_{\text{surf}} = 0$, one obtains

$$\begin{aligned} \mathbf{v}' \cdot \mathbf{n} = 0 &= \left(\frac{\hbar}{m_4} \frac{\partial \mathcal{S}}{\partial x} + \omega y \right) \frac{x}{R_1^2} \\ &\quad + \left(\frac{\hbar}{m_4} \frac{\partial \mathcal{S}}{\partial y} - \omega x \right) \frac{y}{R_2^2} + \left. \left(\frac{\hbar}{m_4} \frac{\partial \mathcal{S}}{\partial z} \right) \frac{z}{R_3^2} \right|_{\text{surf}} \end{aligned}$$

It can be checked that $\mathcal{S} = xyz$ is a solution to this equation provided that

$$\frac{\hbar}{m_4} \left(\frac{1}{R_1^2} + \frac{1}{R_2^2} \right) \alpha = \left(\frac{1}{R_2^2} - \frac{1}{R_1^2} \right) \omega$$

Hence,

$$\alpha = \frac{m_4}{\hbar} \left(\frac{R_2^2 - R_1^2}{R_1^2 + R_2^2} \right) \omega$$

and

$$\mathcal{S} = \frac{m_4}{\hbar} \left(\frac{R_2^2 - R_1^2}{R_1^2 + R_2^2} \right) \omega xy$$

The velocity in the laboratory is $\mathbf{v} = (\hbar/m_4) \nabla \mathcal{S} = (\hbar/m_4) \alpha (y, x, 0)$, and in the vessel (co-rotating frame) is $\mathbf{v}' = \beta (R_1^2 y, -R_2^2 x, 0)$, where $\beta \equiv 2\omega/(R_1^2 + R_2^2)$. Once they have been determined, their circulation lines are straightforwardly obtained. In the laboratory frame, they are

$$x^2 - y^2 = c,$$

which is the appearance of the circulation lines displayed in Fig. 8. In the vessel frame, they are

$$\frac{x^2}{(\xi R_1)^2} + \frac{y^2}{(\xi R_2)^2} = 1.$$

These lines are “parallel” to the ellipsoidal surface.

We define the deformation parameter ε

$$\varepsilon = \frac{\langle x^2 \rangle - \langle y^2 \rangle}{\langle x^2 \rangle + \langle y^2 \rangle}$$

where e.g.,

$$\langle x^2 \rangle = \frac{1}{N} \int d\mathbf{r} x^2 \Psi(\mathbf{r})$$

For the sharp surface ellipsoid above,

$$\alpha = \frac{m_4}{\hbar} \varepsilon \omega \quad (16)$$

This relationship is not general but can be used as a guide for our more general approach. Let us now discuss the angular momentum and moment of inertia of the irrotational fluid droplet. Recalling that

$$L_z = -i\hbar \left(x \frac{\partial}{\partial y} - y \frac{\partial}{\partial x} \right)$$

if we write

$$\Psi(\mathbf{r}) = \Phi(\mathbf{r}) e^{i\omega xy}$$

with $\Phi(\mathbf{r})$ a real function,

$$\langle L_z \rangle = \hbar \alpha \int d\mathbf{r} (x^2 - y^2) \Phi^2(\mathbf{r})$$

If eqn (16) holds,

$$\begin{aligned} \langle L_z \rangle &= \varepsilon m_4 N [\langle x^2 \rangle - \langle y^2 \rangle] \omega \\ &= m_4 N \left(\frac{[\langle x^2 \rangle - \langle y^2 \rangle]^2}{\langle x^2 \rangle + \langle y^2 \rangle} \right) \omega \equiv \mathcal{I}_{\text{irr}} \omega \end{aligned} \quad (17)$$

where

$$\mathcal{I}_{\text{irr}} = m_4 N \left(\frac{[\langle x^2 \rangle - \langle y^2 \rangle]^2}{\langle x^2 \rangle + \langle y^2 \rangle} \right)$$

is the irrotational moment of inertia. For a rigid solid,

$$\mathcal{I}_{\text{rig}} = m_4 \int d\mathbf{r} (x^2 + y^2) \Phi^2(\mathbf{r}) = m_4 N [\langle x^2 \rangle + \langle y^2 \rangle]$$

Hence,

$$\frac{\mathcal{I}_{\text{irr}}}{\mathcal{I}_{\text{rig}}} = \left[\frac{\langle x^2 \rangle - \langle y^2 \rangle}{\langle x^2 \rangle + \langle y^2 \rangle} \right]^2 \rightarrow 0 \quad \text{if } \varepsilon \rightarrow 0$$

Finally, we discuss the kinetic energy of the droplet

$$E_{\text{kin}} = \frac{\hbar^2}{2m_4} \int d\mathbf{r} |\nabla \Psi(\mathbf{r})|^2$$

From the above $\Psi(\mathbf{r})$,

$$\begin{aligned} E_{\text{kin}} &= \frac{\hbar^2}{2m_4} \int d\mathbf{r} |\nabla \Phi(\mathbf{r})|^2 \\ &+ \frac{\hbar^2}{2m_4} \alpha^2 \int d\mathbf{r} (x^2 + y^2) \Phi^2(\mathbf{r}) = E_{\text{intr}} + E_{\text{coll}} \end{aligned}$$

where the first term is the “intrinsic” kinetic energy and the second term arises from the irrotational velocity field

$$\begin{aligned} E_{\text{coll}} &= \frac{\hbar^2}{2m_4} \alpha^2 \int d\mathbf{r} (x^2 + y^2) \Phi^2(\mathbf{r}) \\ &= \frac{1}{2} \left\{ m_4 \varepsilon^2 \int d\mathbf{r} (x^2 + y^2) \Phi^2(\mathbf{r}) \right\} \omega^2 = \frac{1}{2} \mathcal{I}_{\text{irr}} \omega^2 \end{aligned}$$

These expressions may be used to obtain some estimates from the actual DFT calculations. For a ${}^4\text{He}_{1000}$ droplet and $\omega = 0.10 \text{ K}/\hbar$, we have obtained $\langle x^2 \rangle = 100.82 \text{ \AA}^2$ and $\langle y^2 \rangle = 101.82 \text{ \AA}^2$; hence, $\varepsilon \sim -1/200$. Since $\hbar^2/m_4 = 12.12 \text{ K \AA}^2$, from eqn (16) one has $\alpha \sim -4.2 \times 10^{-5} \text{ \AA}^{-2}$. From eqn (17), we obtain $\langle L_z \rangle \sim 4 \times 10^{-2} \hbar$.

In a Bose-Einstein condensate, the deformation ε is a control parameter that can be set to a very large value (close to unity). For a self-bound ${}^4\text{He}$ droplet, deformation comes from “rotation” itself and it turns out to be minute even for angular frequencies close to the critical frequency for one-vortex nucleation; the conclusion is that the droplet “does not rotate”; in other words, it is unable to store an appreciable amount of angular momentum before vortex nucleation.

Acknowledgements

We would like to thank Antonio Muñoz, Jordi Ortín, Humphrey Maris and Andrey Vilesov for useful discussions and exchanges. We would also like to thank Nicolas Renon and Emmanuel Courcelle of CALMIP who greatly improved the performance of our code. This work has been performed under Grant No. FIS2014-52285-C2-1-P from DGI, Spain, and 2014SGR401 from Generalitat de Catalunya. MB thanks the Université Fédérale Toulouse Midi-Pyrénées for financial support through the “Chaires d’Attractivité 2014” Programme IMDYNHE. The dynamic simulations presented in this work have been carried out thanks to the HPC resources of the CALMIP supercomputing center (Grant P1039).

References

1. A. Scheidemann, J. P. Toennies and J. A. Northby, *Phys. Rev. Lett.*, 1990, **64**, 1899.
2. F. Stienkemeier, J. Higgins, C. Callegari, S. I. Kanorsky, W. E. Ernst and G. Scoles, *Z. Phys. D*, 1996, **38**, 253; F. Ancilotto, P. B. Lerner and M. W. Cole, *J. Low Temp. Phys.*, 1995, **101**, 1123.
3. A. Hernando, R. Mayol, M. Pi, M. Barranco, F. Ancilotto, O. Bünermann and F. Stienkemeier, *J. Phys. Chem. A*, 2007, **111**, 7303.

- 4 J. P. Toennies and A. F. Vilesov, *Angew. Chem. Phys.*, 2004, **43**, 2622.
- 5 F. Stienkemeier and K. K. Lehmann, *J. Phys. B: At., Mol. Opt. Phys.*, 2006, **39**, R127.
- 6 J. Tiggessäumker and F. Stienkemeier, *Phys. Chem. Chem. Phys.*, 2007, **9**, 4748.
- 7 C. Callegari and W. E. Ernst, *Handbook of High Resolution Spectroscopy*, Wiley, New York, 2011, vol. 3, p. 1551.
- 8 M. Mudrich and F. Stienkemeier, *Int. Rev. Phys. Chem.*, 2014, **33**, 301.
- 9 M. Lewerenz, B. Schilling and J. P. Toennies, *J. Chem. Phys.*, 1995, **102**, 8191.
- 10 L. F. Gomez, E. Loginov, R. Sliter and A. Vilesov, *J. Chem. Phys.*, 2011, **135**, 154201.
- 11 L. F. Gomez, K. R. Ferguson, J. P. Cryan, C. Bacellar, R. Mayro P. Tanyag, C. Jones, S. Schorb, D. Anielski, A. Belkacem, C. Bernando, R. Boll, J. Bozek, S. Carron, G. Chen, T. Delmas, L. Englert, S. W. Epp, B. Erk, L. Foucar, R. Hartmann, A. Hexemer, M. Huth, J. Kwok, S. R. Leone, J. H. S. Ma, F. R. N. C. Maia, E. Malmerberg, S. Marchesini, D. M. Neumark, B. Poon, J. Prell, D. Rolles, B. Rudek, A. Rudenko, M. Seifrid, K. R. Siefermann, F. P. Sturm, M. Swiggers, J. Ullrich, F. Weise, P. Zwart, C. Bostedt, O. Gessner and A. F. Vilesov, *Science*, 2014, **345**, 906.
- 12 C. F. Jones, Ch. Bernando, R. Tanyag, K. R. Ferguson, C. Bacellar, L. Gomez, D. Anielski, A. Belkacem, R. Boll, J. Bozek, S. Carron, J. Cryan, L. Englert, S. W. Epp, B. Erk, R. Hartmann, L. Foucar, D. M. Neumark, D. Rolles, B. Rudek, A. Rudenko, K. R. Siefermann, F. P. Sturm, J. Ullrich, F. Weise, Ch. Bostedt, O. Gessner and A. F. Vilesov, *Phys. Rev. B*, 2016, **93**, 180510(R).
- 13 C. Bernando, R. Mayro, P. Tanyag, C. Jones, C. Bacellar, M. Bucher, K. R. Ferguson, D. Rupp, M. P. Ziemkiewicz, L. F. Gomez, A. S. Chatterley, T. Gorkhover, M. Müller, J. Bozek, S. Carron, J. Kwok, S. L. Butler, T. Möller, Ch. Bostedt, O. Gessner and A. F. Vilesov, *Phys. Rev. B*, 2017, **95**, 064510.
- 14 R. M. P. Tanyag, C. F. Jones, C. Bernando, S. M. O. O'Connell, D. Verma and A. F. Vilesov, Experiments with large superfluid helium nanodroplets, in *Cold Chemistry: Molecular Scattering and Reactivity Near Absolute Zero*, ed. A. Osterwalder and O. Dulieu, Royal Society of Chemistry, Cambridge, UK, to be published, ch. 8, 2017.
- 15 V. Lebedev, P. Moroshkin, B. Grobety, E. B. Gordon and A. Weis, *J. Low Temp. Phys.*, 2011, **165**, 166.
- 16 L. F. Gomez, E. Loginov and A. F. Vilesov, *Phys. Rev. Lett.*, 2012, **108**, 155302.
- 17 E. Latimer, D. Spence, C. Feng, A. Boatwright, A. M. Ellis and S. Yang, *Nano Lett.*, 2014, **14**, 2902.
- 18 Ph. Thaler, A. Volk, F. Lackner, J. Steurer, D. Knez, W. Grogger, F. Hofer and W. E. Ernst, *Phys. Rev. B: Condens. Matter Mater. Phys.*, 2014, **90**, 155442.
- 19 G. P. Bewley, S. Matthew, S. Paoletti, R. Katepalli, R. Sreenivasan and D. P. Lathrop, *Proc. Natl. Acad. Sci. U. S. A.*, 2008, **105**, 13707.
- 20 A. Leal, D. Mateo, A. Hernando, M. Pi and M. Barranco, *Phys. Chem. Chem. Phys.*, 2014, **16**, 23206.
- 21 A. Vilà, M. González and R. Mayol, *Phys. Chem. Chem. Phys.*, 2016, **18**, 2006.
- 22 A. Hernando, M. Barranco, M. Pi, E. Loginov, M. Langlet and M. Drabbels, *Phys. Chem. Chem. Phys.*, 2012, **14**, 3996.
- 23 F. Coppens, A. Leal, M. Barranco, N. Halberstadt and M. Pi, *J. Low Temp. Phys.*, 2017, **187**, 439.
- 24 *Microscopic approaches to quantum liquids in confined geometries, Series on Advances in Quantum Many-Body Theory*, ed. E. Krotscheck and J. Navarro, World Scientific, Singapore, vol. 4, 2002.
- 25 M. Barranco, R. Guardiola, S. Hernández, R. Mayol, J. Navarro and M. Pi, *J. Low Temp. Phys.*, 2006, **142**, 1.
- 26 J. von Vangerow, A. Stieg, F. Stienkemeier, M. Mudrich, A. Leal, D. Mateo, A. Hernando, M. Barranco and M. Pi, *J. Phys. Chem. A*, 2014, **118**, 6604.
- 27 D. Mateo, A. Leal, A. Hernando, M. Barranco, M. Pi, F. Cargnani, M. Mella, X. Zhang and M. Drabbels, *J. Chem. Phys.*, 2014, **140**, 131101.
- 28 A. Leal, D. Mateo, A. Hernando, M. Pi, M. Barranco, A. Ponti, F. Cargnani and M. Drabbels, *Phys. Rev. B: Condens. Matter Mater. Phys.*, 2014, **90**, 224518.
- 29 A. Leal, X. Zhang, M. Barranco, F. Cargnani, A. Hernando, D. Mateo, M. Mella, M. Drabbels and M. Pi, *J. Chem. Phys.*, 2016, **144**, 094302.
- 30 J. von Vangerow, F. Coppens, A. Leal, M. Pi, M. Barranco, N. Halberstadt, F. Stienkemeier and M. Mudrich, *J. Phys. Chem. Lett.*, 2017, **8**, 307.
- 31 F. Ancilotto, M. Barranco, F. Caupin, R. Mayol and M. Pi, *Phys. Rev. B: Condens. Matter Mater. Phys.*, 2005, **72**, 214522.
- 32 I. A. Pshenichnyuk and N. G. Berloff, *Phys. Rev. B*, 2016, **94**, 184505.
- 33 D. Kivotides, C. F. Barenghi and Y. A. Sergeev, *Phys. Rev. B: Condens. Matter Mater. Phys.*, 2008, **77**, 014527.
- 34 K. T. Tang and J. P. Toennies, *Z. Phys. D*, 1986, **1**, 91.
- 35 M. Frigo and S. G. Johnson, *Proc. IEEE*, 2005, **93**, 216.
- 36 A. Ralston and H. S. Wilf, *Mathematical methods for digital computers*, John Wiley and Sons, New York, 1960.
- 37 D. Mateo, D. Jin, M. Barranco and M. Pi, *J. Chem. Phys.*, 2011, **134**, 044507.
- 38 4He-DFT BCN-TLS: A Computer Package for Simulating Structural Properties and Dynamics of Doped Liquid Helium-4 Systems. M. Pi, F. Ancilotto, F. Coppens, N. Halberstadt, A. Hernando, A. Leal, D. Mateo, R. Mayol and M. Barranco, <https://github.com/bcntls2016/>.
- 39 See the ESI† for the continuous movie corresponding to the simulation.
- 40 D. L. Whitaker, M. A. Weilert, C. L. Vicente, H. J. Maris and G. M. Seidel, *J. Low Temp. Phys.*, 1998, **110**, 173.
- 41 M. Pi, R. Mayol, A. Hernando, M. Barranco and F. Ancilotto, *J. Chem. Phys.*, 2007, **126**, 244502.
- 42 F. Ancilotto, M. Pi and M. Barranco, *Phys. Rev. B: Condens. Matter Mater. Phys.*, 2015, **91**, 100503(R).
- 43 F. Dalfovo, R. Mayol, M. Pi and M. Barranco, *Phys. Rev. Lett.*, 2000, **85**, 1028.

- 44 F. Ancilotto, M. Pi and M. Barranco, *Phys. Rev. B: Condens. Matter Mater. Phys.*, 2014, **90**, 174512.
- 45 W. F. Vinen, *Proc. - R. Soc. Edinburgh, Sect. A: Math. Phys. Sci.*, 1961, **260**, 218.
- 46 G. A. Williams and R. E. Packard, *Phys. Rev. Lett.*, 1974, **33**, 280.
- 47 G. M. Seidel and H. J. Maris, *Physica B*, 1994, **194-196**, 577.
- 48 A. Bohr and B. R. Mottelson, *Nuclear Structure*, W. A. Benjamin, vol. II, App. 6A, 1975.
- 49 A. Recati, F. Zambelli and S. Stringari, *Phys. Rev. Lett.*, 2001, **86**, 377.
- 50 E. Guyon, J.-P. Hulin, L. Petit and C. D. Mitescu, *Physical Hydrodynamics*, Oxford University Press, Oxford, UK, 2nd edn, 2015.
- 51 L. J. Campbell and R. M. Ziff, *Phys. Rev. B: Condens. Matter Mater. Phys.*, 1979, **20**, 1886.
- 52 A. F. Vilesov, Private communication, 2017.

Chapter 7

Conclusions & Outlook

Bibliography

- [1] P. Kapitza, Nature **141**, 74 (1938), URL <http://dx.doi.org/10.1038/141074a0>.
- [2] B. Rollin and F. Simon, Physica **6**, 219 (1939), ISSN 0031-8914, URL <http://www.sciencedirect.com/science/article/pii/S0031891439800131>.
- [3] W. Keesom and M. A. Keesom, Physica **3**, 359 (1936), ISSN 0031-8914, URL <http://www.sciencedirect.com/science/article/pii/S0031891436803127>.
- [4] L. Tisza, Comptes rendus hebdomadaires des séances de l'Académie des sciences **207**, 1035 (1938), URL <http://gallica.bnf.fr/ark:/12148/bpt6k31590/f1035.item>.
- [5] L. Tisza, Comptes rendus hebdomadaires des séances de l'Académie des sciences **207**, 1186 (1938), URL <http://gallica.bnf.fr/ark:/12148/bpt6k31590/f1186.item>.
- [6] L. Tisza, J. Phys. Radium **1**, 164 (1940), URL <https://doi.org/10.1051/jphysrad:0194000105016400>.
- [7] L. Tisza, J. Phys. Radium **1**, 350 (1940), URL <https://doi.org/10.1051/jphysrad:0194000108035000>.
- [8] P. Lebrun, Cryogenics **34**, 1 (1994), ISSN 0011-2275, fifteenth International Cryogenic Engineering Conference, URL <http://www.sciencedirect.com/science/article/pii/S0011227505800037>.
- [9] W. Keesom and M. A. Keesom, KNAW, Proceedings **35**, 736 (1932), URL <http://www.dwc.knaw.nl/DL/publications/PU00016277.pdf>.
- [10] R. J. Donnelly, Physics Today **62**, 34 (2009), <https://doi.org/10.1063/1.3248499>, URL <https://doi.org/10.1063/1.3248499>.

- [11] H. Kamerlingh Onnes, KNAW, Proceedings **10**, 744 (1908), URL <http://www.dwc.knaw.nl/toegangen/digital-library-knaw/?pagetype=publDetail&pId=PU00013699>.
- [12] H. Kamerlingh Onnes, KNAW, Proceedings **11**, 168 (1909), URL <http://www.dwc.knaw.nl/toegangen/digital-library-knaw/?pagetype=publDetail&pId=PU00013525>.
- [13] P. J. McLennan, H. Smith, and J. Wilhelm, The London, Edinburgh, and Dublin Philosophical Magazine and Journal of Science **14**, 161 (1932), <https://doi.org/10.1080/14786443209462044>, URL <https://doi.org/10.1080/14786443209462044>.
- [14] E. F. Burton, Nature **135**, 265 (1935), URL <http://dx.doi.org/10.1038/135265a0>.
- [15] M. v. Laue, F. London, and H. London, Zeitschrift für Physik **96**, 359 (1935), ISSN 0044-3328, URL <https://doi.org/10.1007/BF01343868>.
- [16] F. Simon, Nature **133**, 529 (1934), URL <http://dx.doi.org/10.1038/133529a0>.
- [17] F. London, Proceedings of the Royal Society of London A: Mathematical, Physical and Engineering Sciences **153**, 576 (1936), ISSN 0080-4630, <http://rspa.royalsocietypublishing.org/content/153/880/576.full.pdf>, URL <http://rspa.royalsocietypublishing.org/content/153/880/576>.
- [18] J. F. Allen, R. Peierls, and M. Zaki Uddin, Nature **140**, 62 (1937), URL <http://dx.doi.org/10.1038/140062a0>.
- [19] J. F. Allen and A. D. Misener, Nature **141**, 75 (1938), URL <http://dx.doi.org/10.1038/141075a0>.
- [20] F. London, Nature **141**, 643 (1938), URL <http://dx.doi.org/10.1038/141643a0>.
- [21] L. Tisza, Nature **141**, 913 (1938), URL <http://dx.doi.org/10.1038/141913a0>.
- [22] L. Landau, Phys. Rev. **60**, 356 (1941), URL <https://link.aps.org/doi/10.1103/PhysRev.60.356>.

- [23] L. Landau, Phys. Rev. **75**, 884 (1949), URL <https://link.aps.org/doi/10.1103/PhysRev.75.884>.
- [24] N. N. Bogolyubov, J. Phys. (USSR) **11**, 23 (1947), [Izv. Akad. Nauk Ser. Fiz. 11, 77 (1947)], URL <https://ufn.ru/ru/articles/1967/11/o/>.
- [25] E. A. Cornell and C. E. Wieman, Rev. Mod. Phys. **74**, 875 (2002), URL <https://link.aps.org/doi/10.1103/RevModPhys.74.875>.
- [26] W. Ketterle, Rev. Mod. Phys. **74**, 1131 (2002), URL <https://link.aps.org/doi/10.1103/RevModPhys.74.1131>.
- [27] D. Mateo, M. Barranco, and J. Navarro, Phys. Rev. B **82**, 134529 (2010).
- [28] R. J. Donnelly, J. A. Donnelly, and R. N. Hills, J. Low Temp. Phys. **44**, 471 (1981).
- [29] E. Krotscheck and J. Navarro, eds., *Microscopic approaches to quantum liquids in confined geometries*, vol. 4 of *Series on Advances in Quantum Many-Body Theory* (World Scientific, Singapore, 2002).
- [30] M. P. de Lara-Castells, G. Delgado-Barrio, P. Villarreal, and A. O. Mitrushchenkov, J. Chem. Phys. **125**, 221101 (2006).
- [31] M. P. de Lara-Castells, N. F. Aguirre, P. Villarreal, G. Delgado-Barrio, and A. O. Mitrushchenkov, J. Chem. Phys. **132**, 194313 (2010).
- [32] N. F. Aguirre, P. Villarreal, G. Delgado-Barrio, A. O. Mitrushchenkov, and M. P. de Lara-Castells, Phys. Chem. Chem. Phys. **15**, 10126 (2013).
- [33] S. Stringari and J. Treiner, Phys. Rev. B **36**, 8369 (1987).
- [34] S. Stringari and J. Treiner, J. Chem. Phys. **87**, 5021 (1987).
- [35] F. Dalfovo, A. Lastri, L. Pricaupenko, S. Stringari, and J. Treiner, Phys. Rev. B **52**, 1193 (1995).
- [36] P. Hohenberg and W. Kohn, Phys. Rev. **136**, B864 (1964).
- [37] Z. J. Jakubek, Q. Hui, and M. Takami, Phys. Rev. Lett. **79**, 629 (1997).
- [38] A. Nakayama and K. Yamashita, J. Chem. Phys. **114**, 780 (2001).
- [39] M. Barranco, F. Coppens, N. Halberstadt, A. Hernando, A. Leal, D. Mateo, R. Mayol, and M. Pi ((2017)), <https://github.com/bcctl2016/DFT-Guide/blob/master/dft-guide.pdf>.